E-8247
12/6/93

NASA Technical Memorandum 106411

A Study of the Compressible Flow Through a Diffusing S-Duct

Steven R. Wellborn and Theodore H. Okiishi
Iowa State University
Ames, Iowa

and

Bruce A. Reichert
Lewis Research Center
Cleveland, Ohio

December 1993

NASA

A STUDY OF THE COMPRESSIBLE FLOW THROUGH A DIFFUSING S-DUCT

Steven R. Wellborn and Theodore H. Okiishi
Iowa State University
Ames, Iowa 50011
and
Bruce A. Reichert
National Aeronautics and Space Administration
Lewis Research Center
Cleveland, Ohio 44135

ABSTRACT

Benchmark aerodynamic data are presented for compressible flow through a representative S-duct configuration. A numerical prediction of the S-duct flow field, obtained from a subsonic parabolized Navier-Stokes algorithm, is also shown. The experimental and numerical results are compared.

Measurements of the three-dimensional velocity field, total pressures and static pressures were obtained at five cross-sectional planes. Aerodynamic data were gathered with calibrated pneumatic probes. Surface static pressure and surface flow visualization data were also acquired. All reported tests were conducted with an inlet centerline Mach number of 0.6. The Reynolds number, based on the inlet centerline velocity and duct inlet diameter, was 2.6×10^6. Thin inlet turbulent boundary layers existed.

The collected data should be beneficial to aircraft inlet designers and the measurements are suitable for the validation of computational codes. The results show that a region of streamwise flow separation occurred within the duct. Details about the separated flow region, including mechanisms which drive this complicated flow phenomenon, are discussed. Results also indicate that the duct curvature induces strong pressure driven secondary flows. The cross flows evolve into counter-rotating vortices. These vortices convect low momentum fluid of the boundary layer toward the center of the duct, degrading both the uniformity and magnitude of the total pressure profile.

Page intentionally left blank

TABLE OF CONTENTS

ABSTRACT i

LIST OF FIGURES v

LIST OF TABLES vii

NOMENCLATURE viii

ACKNOWLEDGMENTS x

CHAPTER I. INTRODUCTION 1

CHAPTER II. A REVIEW OF PRIOR INVESTIGATIONS 3

CHAPTER III. EXPERIMENTAL FACILITIES AND PROCEDURES 6

Probe Calibration Facility 6

Experimental Test Facility 7

S-Duct Geometry 10

Instrumentation and Measurement Techniques 12

CHAPTER IV. COMPUTATIONAL ANALYSIS 21

Formulation of Equations 21

Numerical Procedure 23

Grid Distributions 25

Boundary Conditions 28

CHAPTER V. INLET FLOW CONDITIONS 29

CHAPTER VI. RESULTS AND DISCUSSION 31

Surface Streakline Patterns 32

Surface Static Pressures 35

Cross-Stream Aerodynamic Data in Plane A 37

Cross-Stream Aerodynamic Data in Plane B 40

Cross-Stream Aerodynamic Data in Plane C 46

Cross-stream Aerodynamic Data in Plane D 52

Cross-stream Aerodynamic Data in Plane E 58

CHAPTER VII. FURTHER INSIGHTS INTO SEPARATED FLOW 64
CHAPTER VIII. CONCLUSIONS 70
CHAPTER IX. RECOMMENDATIONS FOR FURTHER RESEARCH 72
CHAPTER X. POSTSCRIPT 73
BIBLIOGRAPHY 74
APPENDIX A. THREE-HOLE PROBE CALIBRATION AND DATA REDUCTION TECHNIQUES 78
The Three-Hole Probe 78
Yaw-Nulling Calibration 79
Data Reduction 81
APPENDIX B. FIVE-HOLE PROBE CALIBRATION AND DATA REDUCTION TECHNIQUES 82
The Five-Hole Probe 82
Yaw-Nulling Calibration 83
Yaw-Nulling Data Reduction 87
Non-Yaw-Nulling Calibration 88
Non-Yaw-Nulling Data Reduction 95

LIST OF FIGURES

Figure III.1 Schematic of the probe calibration facility 6
Figure III.2 Pitch and yaw mechanisms assembled on the calibration rig 8
Figure III.3 Schematic of the Internal Fluid Mechanics Facility 9
Figure III.4 Half shell representation of the diffusing S-duct 11
Figure III.5 Half shell representation of the diffusing S-duct indicating the measurement plane locations 15
Figure III.6 Measurement plane schematic for Plane A 16
Figure III.7 Measurement plane schematic for Plane B, C and D 17
Figure III.8 Measurement plane schematic for Plane E 18
Figure III.9 Static tap mounting procedure schematic 19
Figure IV.1 Computational mesh distribution for the potential solution 26
Figure IV.2 Computational mesh distribution for the viscous solution 27
Figure V.1 Experimental law-of-the-wall velocity profile measured at Plane A 30
Figure VI.2 Surface oil flow patterns at the duct exit showing flow symmetry 33
Figure VI.3 Surface oil flow patterns on one symmetric half of the duct surface 33
Figure VI.4 Close up of the surface oil flow patterns developed in the separation region 34
Figure VI.5 Surface oil flow patterns on the centerline splitter plate 34
Figure VI.6 Axial distributions of surface static pressure for three circumferential positions 35
Figure VI.7 Circumferential distributions of surface static pressures in Planes A, B, C and D 37
Figure VI.8 Total pressure distributions in Plane A 38
Figure VI.9 Normal velocity distributions in Plane A 39
Figure VI.10 Static pressure distributions in Plane B 41
Figure VI.11 Total pressure distributions in Plane B 42
Figure VI.12 Normal velocity distributions in Plane B 43
Figure VI.13 Transverse velocity vectors in Plane B 44
Figure VI.14 Streamwise vorticity distributions in Plane B 45
Figure VI.15 Static pressure distributions in Plane C 47
Figure VI.16 Total pressure distributions in Plane C 48

Figure VI.17 Normal velocity distributions in Plane C 49
Figure VI.18 Transverse velocity vectors in Plane C 50
Figure VI.19 Streamwise vorticity distributions in Plane C 51
Figure VI.20 Static pressure distributions in Plane D 53
Figure VI.21 Total pressure distributions in Plane D 54
Figure VI.22 Normal velocity distributions in Plane D 55
Figure VI.23 Transverse velocity vectors in Plane D 56
Figure VI.24 Streamwise vorticity distributions in Plane D 57
Figure VI.25 Total pressure distributions in Plane E 59
Figure VI.26 Normal velocity distributions in Plane E 60
Figure VI.27 Transverse velocity vectors in Plane E 61
Figure VI.28 Streamwise vorticity distributions in Plane E 62
Figure VII.1 Illustrations of elementary singular points 64
Figure VII.2 Streamsurface bifurcations on a solid wall 65
Figure VII.3 Unwrapped S-duct surface streakline patterns 66
Figure VII.4 Skeleton schematic of the surface streakline patterns 67
Figure VII.5 Perspective view of an owl face separation of the first kind 68
Figure VII.6 Skeleton schematic illustrating asymmetric surface streakline patterns . . . 69
Figure A.1 The cobra three-hole probe 78
Figure A.2 Variation of the three-hole probe pressure coefficients with total-to-static pressure ratio 80
Figure B.1 Pictorial of the five-hole probe 82
Figure B.2 Variation of pressure coefficients with pitch angle for various Mach numbers 84
Figure B.3 Five hole probe pitch angles 85
Figure B.4 Variation of pressure coefficients with pitch and yaw angle for 0.4 Mach number 90

LIST OF TABLES

Table III.1 Experimental measurement plane information 14
Table V.1 Experimental and computational flow conditions in Plane A 30
Table B.1 Results of probe symmetry for calibration coefficients 94

NOMENCLATURE

ENGLISH

a	=	Local speed of sound
a_o	=	Stagnation speed of sound
a, b, c	=	Constants or coefficients
A	=	Duct cross-sectional area
Cp	=	Static pressure coefficient
Cp_i	=	Probe pressure coefficients
$\widehat{C}p_i$	=	Taylor series approximations to probe pressure coefficients
Cp_o	=	Total pressure coefficient
d	=	Duct inlet diameter
e	=	Unit vector in direction of the velocity vector
f, g	=	Calibration functions
H	=	Boundary layer shape factor (δ_1/δ_2)
M	=	Mach number
M	=	Normalized Mach number
p	=	Static pressure
p_i	=	Probe pressures
p_m	=	One-dimensional streamwise static pressure correction
p_o	=	Total pressure
P	=	Streamwise static pressure in PNS equations
Pr	=	Prandtl number
r	=	Duct cross-sectional radius
R	=	Duct centerline curvature radius
Re	=	Reynolds number
s	=	Centerline arc length
T	=	Static temperature
u,v,w	=	Velocity components in the cartesian coordinate system
u^+,y^+	=	Law-of-the-wall coordinates
x,y,z	=	Cartesian coordinate system fixed to the S-duct
x', y', z'	=	Cartesian coordinate system fixed to the measurement plane

GREEK

α	=	Pitch angle relative to the measurement plane
β	=	Yaw angle relative to the measurement plane
γ	=	Specific heat ratio
δ	=	Boundary layer thickness
δ_1	=	Displacement thickness
δ_2	=	Momentum thickness
θ	=	Duct substended angle
μ	=	Viscosity
ρ	=	Static density
ϕ	=	Cross-stream polar angle
Φ	=	Velocity potential variable
ω_s	=	Streamwise vorticity component
Ω_s	=	Nondimensional streamwise vorticity component

SUBSCRIPTS

c	=	Measured angle determined from probe calibration
cl	=	Inlet centerline condition
max	=	Maximum
o	=	Deflection or reference angle

ACKNOWLEDGMENTS

This research owes its existence to the efforts of many. We express our appreciation to the NASA Lewis Research Center, Cleveland, Ohio, sponsor of this work under Grant No. NAG 3–1275. In addition, we acknowledge the personnel without whose support this research endeavor would not have been possible. In particular we would like to thank Bob Davis, Kelly Hall, Bill Darby, Nick Wolansky, Bob Gronski and Mike Peters for their advice, support, assistance and skilled workmanship. We additionally thank Bruce Wendt, Warren Hingst, Jon McLaughlin and Dave Davis for their enlightening conversations and valuable discussions.

CHAPTER I

INTRODUCTION

Aircraft propulsion systems often use S-ducts. A primary purpose of an S-duct is to convey air flow from the wing or fuselage intake to the engine compressor. Examples of commercial aircraft with S-ducts include the Boeing 727 and the Lockheed Tristar L-1011. Amongst military aircraft, both the General Dynamics F-16 and the McDonnell-Douglas F-18 use S-shaped ducts.

Diffusing S-ducts have centerline curvature and cross-sectional area increase. Curvature of the centerline or changes in the duct cross-sectional shape give rise to streamline curvature. Cross-stream pressure gradients, resulting from streamline curvature, can produce significant secondary flows. Additionally, the adverse streamwise pressure gradient, caused by increasing cross-sectional area, can lead to flow separation.

Well designed diffusing S-ducts should efficiently decelerate the compressible incoming flow. Moreover, to achieve appropriate performance, the S-duct must also incur minimal total pressure losses and deliver nearly uniform flow with small transverse velocity components at the engine compressor entrance. Often the aircraft designer faces a difficult dilemma. Size and weight restrictions encourage the use of shorter S-ducts. However, this results in greater streamline curvature, larger adverse pressure gradients and the risk of unacceptable duct performance.

The ability to quickly predict complicated flow phenomena without experimental testing is obviously desirable for designers. The highly three-dimensional flow in a diffusing S-duct presents a substantial challenge to computational fluid dynamic (CFD) flow solvers. Unfortunately, current numerical algorithms normally require a large amount of computer time to solve the Navier-Stokes equations, which are required for complex flows. Moreover, only a limited amount of experimental benchmark data exists for the validation of CFD codes applied to compressible S-duct flows.

This report documents the important details of a concurrent experimental and computational study of the compressible flow through a diffusing S-duct. Experimentally, internal flow measurements of the three-dimensional velocity field, total pressures and static pressures were obtained in five cross-stream measurement planes. Surface static pressures and surface

flow visualization were also used to reveal flow field characteristics. Numerically, the flow field was modeled using an efficient subsonic parabolized Navier-Stokes (PNS) algorithm.

The emphasis of this report is placed on the experimental measurements. The objective of the experimental study is to investigate the development of the flow field and to provide a comprehensive benchmark data set for the compressible flow through a representative diffusing S-duct. Numerical calculations are presented concurrently with the measured results to help explain the development of the flow. The computational results also reaffirm that PNS models quickly and efficiently produce qualitatively correct results of complex internal flow fields.

This study could be beneficial to inlet designers. The numerical results show that flow field trends can be predicted using the simplified parabolized model. The measured data are suitable for CFD code validation. Data for S-ducts containing active or passive flow management devices intended to improve duct performance could be compared to these baseline data.

CHAPTER II

A REVIEW OF PRIOR INVESTIGATIONS

Previous experimental and computational studies have been conducted to determine the character of the fluid motion within S-ducts. From the available literature, selected studies similar to the one presented in this thesis are reviewed. Attention will be drawn to both experimental investigations and computational studies.

The design and implementation of earlier aircraft propulsion S-duct components relied heavily on test-stand data, because, in the past, these flow fields were too complex for numerical modeling. The development of the Boeing 727 center engine inlet duct was documented by both Bauermeister *et al.* [1] and the Boeing Commercial Aircraft Company [2]. Preliminary duct designs of the 727 inlet contained regions of reversed flow and had unacceptable exit pressure distributions. Center engine surging was also experienced during initial flight testing. A detailed experimental study revealed how installation of co-rotating vortex generators within the duct improved exit pressure uniformity, prevented flow separation and provided surgefree operation. In a separate study, the performance of several S-duct scoop diffusers used in conjunction with high-speed turboprop-fan engines was examined by Little and Trimboli [3]. These S-ducts had severe centerline curvature and underwent radical changes in cross-sectional shape. The study suggested the existence of a complicated three dimensional duct flow and provided valuable performance data for a range of applications. Both of these studies are prime examples of the extensive amount of experimental research needed to design efficient S-ducts used for engine inlets.

To aid in inlet design, experimental studies have also been performed on S-ducts which represent simplified models of engine inlets [4–9]. These studies were conducted to qualitatively examine S-duct flow fields and provided better understanding of the flow physics. These studies found counter-rotating vortices within S-ducts. The vortices convected low momentum fluid toward the center of the duct. A highly nonuniform exit velocity field existed. Rowe [4] theoretically proved that the development of the vortices was an inviscid phenomenon, provided that a nonuniform inlet velocity profile (typical of a boundary layer profile) existed. Taylor *et al.* [10,11,8] showed that counter-rotating vortices developed in ducts having circular or square cross sections. In addition, these vortices were present regardless of whether the inlet boundary layer was turbulent or laminar. S-ducts having large

incident inlet flow angles (Guo *et al.* [7,12]) were absent of counter-rotating vortices and instead the entire exit flow rotated, similar to solid body rotation, about the centerline.

Unfortunately, the majority of the studies involving simplified duct models were conducted with incompressible flow and/or thick boundary layers. Furthermore, only a few involved diffusing ducts. Most of the studies did not have streamwise separated flow, because most of the ducts were non-diffusing and had only mild centerline curvature. Streamwise separated flow did occur in the ducts studied by Bansod and Bradshaw [5]. However, the region of separation was small and had no significant effect on the flow field. A large separated flow region was present in a study by Sullivan *et al.* [13], but only surface flow visualization and surface static pressure data were obtained. Further studies involving representative diffusing S-ducts, having streamwise separation, compressible inlet flow conditions and thin inlet turbulent boundary layers, were needed to help interpret the flow physics associated with S-ducts used for aeronautical applications.

Studies on simplified duct models have also been conducted to obtain experimental benchmark data, which are needed to determine the effectiveness of a numerical model's ability to represent the flow field. A considerable amount of benchmark data exists for incompressible flow through S-ducts [7,10,11,8]. The only detailed measurements of compressible flow through a diffusing S-duct were acquired by Vakili *et al.* [9]. In this study, surface flow visualization suggested the existence of three-dimensional separated flow. Aerodynamic data were obtained with a non-calibrated five-port cone probe. These measurements showed that the exit flow was nonuniform.

The importance of computational fluid dynamics (CFD) as a design tool continues to be established. CFD internal flow research includes fully elliptical Navier-Stokes (FNS) and parabolized Navier-Stokes (PNS) models. Past efforts were focused on PNS methods because of their efficiency and small storage requirements. Computations involving many different duct geometries have been accomplished by a NASA Lewis Research Team using a PNS algorithm designated PEPSIG [14–17]. Results showed, in general, acceptable agreement between numerical and experimental data, when experimental data were available. However, the computations underpredicted the extent of exit flow nonuniformity. The location and extent of separation regions were also incorrectly predicted. A review of the literature suggests that the turbulence model was a major cause of this discrepancy.

With the availability of faster and larger memory computers, solving the complete Navier-Stokes equations has become possible. Unfortunately, only a few calculations involving S-ducts have been reported. Smith *et al.* [18] and Harloff *et al.* [19,20] have prepared reports documenting the flows in non-diffusing and diffusing circular cross-section S-ducts. A finite-volume FNS scheme and Baldwin-Lomax turbulence model were used to predict the flow field. Effects of different mesh structures on the flow field were examined. The reports indicate acceptable qualitative agreement with Vakili's *et al.* [9] experimental data. Nevertheless, within the diffusing S-duct, the accurate location and length of separation and the extent of exit flow nonuniformity were not correctly predicted. The discrepancies between computational and experimental data were possibly due to the turbulence model, the mesh density or undocumented disturbances in the experimental measurements. These studies suggested that a k-ϵ turbulence model should be incorporated into the FNS algorithm, a finer mesh should be used and additional comprehensive experimental data should be obtained for compressible diffusing S-duct flows.

The material in this thesis is a partial response to the suggestions of Smith *et al.* [18] and Harloff *et al.* [19,20]. Benchmark data have been obtained for the compressible flow through a diffusing S-duct. These data can be used to validate the computational results obtained from the FNS algorithm which currently incorporates an algebraic or k-ϵ turbulence model. In addition, PNS results reported in this thesis enable interested individuals to compare PNS and FNS prediction capabilities, advantages and disadvantages. Finally, the combination of the detailed experimental and computational data presented together enhances a designers ability to interpret the complicated flow physics within a diffusing S-duct.

CHAPTER III

EXPERIMENTAL FACILITIES AND PROCEDURES

One of the goals of this study was to provide a detailed set of test flow measurements. The calibration facility, test facility, S-duct geometry, instrumentation and measurement techniques used in the experimental program are described in this chapter.

Probe Calibration Facility

A new facility was constructed for the calibration of aerodynamic probes in the Internal Fluids Mechanics Facility at the NASA Lewis Research Center. The facility was designed for convenient access and with it the accurate calibration of measurement probes was possible. The facility consisted of a flow conditioning section, calibration point and an exhaust diverter. A schematic of the facility is shown in Figure III.1.

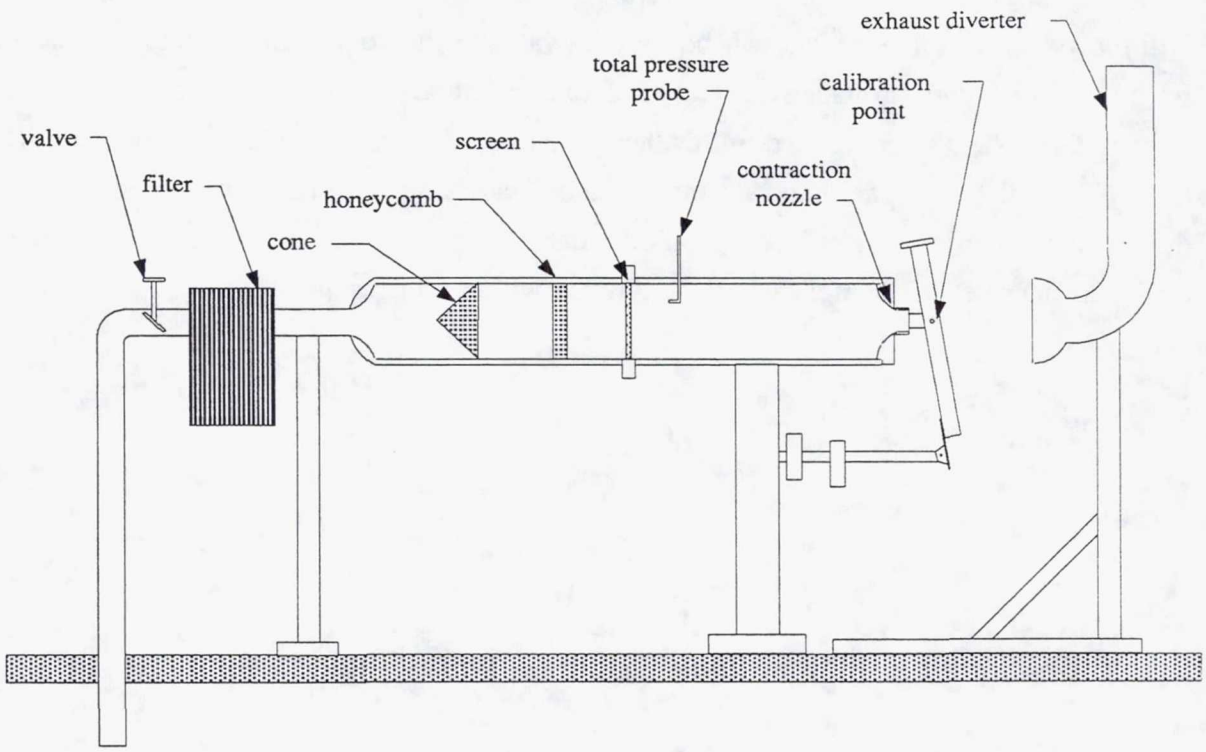

Figure III.1 Schematic of the probe calibration facility

Flow conditioning section

The flow conditioning section contained a series of filters, meshes and screens which provided a uniform freestream flow field. Pressurized shop air was used as the flow driving mechanism. Mach numbers up to 0.85 were attainable. The flow rate was controlled by a gate value. A Cuno filter retained foreign particles from continuing downstream. A perforated steel cone mixed the flow. A two inch wide honeycomb mesh reduced large eddies into small eddies. A fine mesh screen eliminated any local nonuniformities created by the honeycomb mesh. Plenum total pressure was measured by a Pitot probe positioned downstream of the screen. Therefore, only minimal losses occurred between the measured total pressure point and the calibration point. An exit contraction nozzle uniformly accelerated the flow to the calibration point. The diameter of the contraction nozzle at the exit was nominally 5 cm.

Calibration point

The calibration point was located 5 cm away from the contraction exit and in the center of the exhaust flow. The facility allowed rotations in the pitch and yaw directions to occur without repositioning the calibration point. Pitching motion was electronically controlled by an L.C. Smith actuator. Yawing motion was manually adjusted by the operator using a Klinger micro-angle-control (accurate to within 0° 01'). A photograph of pitch and yaw mechanisms assembled on the calibration rig is shown in Figure III.2.

Experimental Test Facility

All experiments were performed at the NASA Lewis Research Center in the Internal Fluid Mechanics Facility. This facility was designed to support tests of a variety of internal flow configurations. Complete details of the facility are described by Porro *et al.* [21] For this experiment, atmospheric test-cell air was drawn through a large settling chamber, passed through the test section and dumped into a large exhaust plenum. The use of test cell air inhibited independent variation of Mach numbers and Reynolds numbers. A schematic of the facility is shown in Figure III.3.

Settling chamber

The settling chamber conditioned the incoming flow in the following way. Air was drawn into the chamber through a large bell-mouth opening. A perforated spreader cone

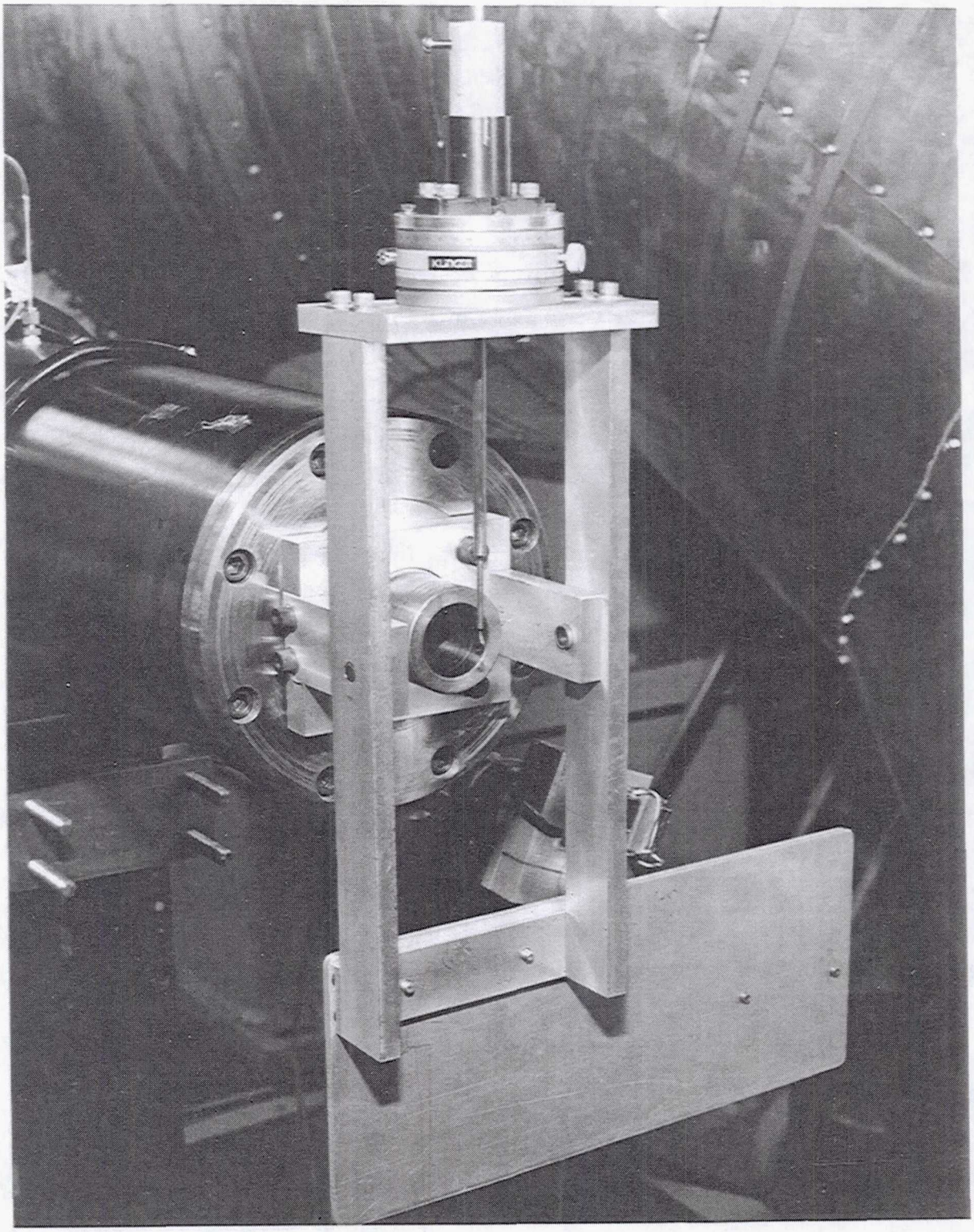

Figure III.2 Pitch and yaw mechanisms assembled on the calibration rig

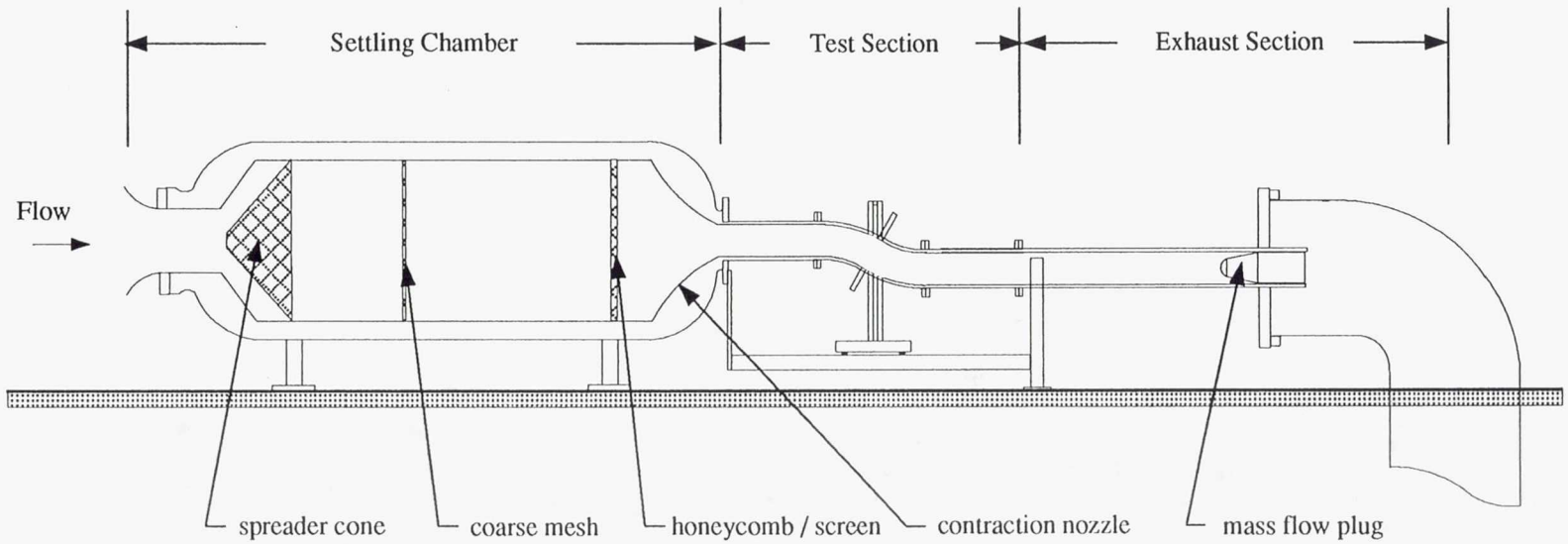

Figure III.3 Schematic of the Internal Fluid Mechanics Facility

mixed the inlet flow. A coarse mesh conditioning screen reduced mean flow nonuniformities. A honeycomb-screen combination removed large scale turbulence fluctuations. A seamless contraction section uniformly accelerated the flow from the settling chamber. An area contraction ratio of 59 to 1 ensured a low turbulence intensity flow and nearly uniform flow at the test section entrance.

Test section

The test section for this experiment consisted of the diffusing S-duct and two constant area duct extensions. The first extension (10.21 cm diameter) served as the interface between the contraction exit and the S-duct entrance. The second extension (12.57 cm diameter) conveyed the flow from the S-duct to the exhaust region. The second extension was able to rotate about its centerline, when the facility was shut down. Each extension was 76.2 cm long and had the same internal surface finish as the S-duct. S-duct details are review in sections S-Duct Geometry and Instrumentation and Measurement Techniques.

Exhaust section

The exhaust section contained a circular cross-section pipe, a mass flow plug and a sub-atmospheric plenum. The pipe was 244 cm long and had a diameter of 12.70 cm. The finish was unpolished. The pipe housed the adjustable mass flow plug and also assured no downstream influence of the exhaust plenum on the test section. The mass flow plug controlled the airflow through the entire facility. Mach numbers up to 0.95 within the test section were possible with this arrangement. Flow was simply dumped into the sub-atmospheric pressure exhaust plenum, which had a 121.92 cm diameter.

S-Duct Geometry

The diffusing S-duct was intentionally designed to incorporate as many of the complex three dimensional flows, including the possibility of unsteady streamwise separation, associated with similar configurations. The duct was designed at the NASA Lewis Research Center. A half shell representation of the diffusing S-duct is shown in Figure III.4.

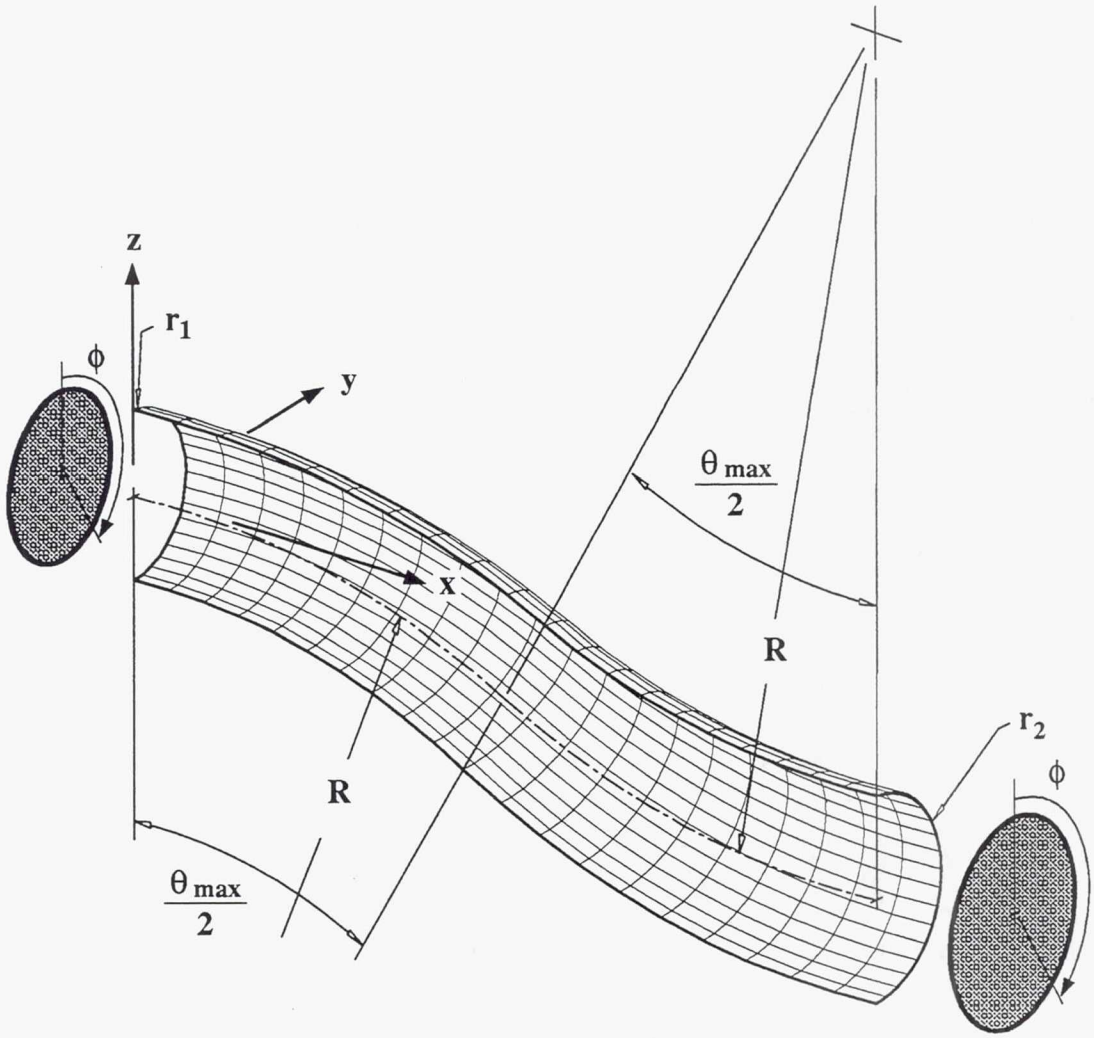

Figure III.4 Half shell representation of the diffusing S-duct

The duct centerline is defined by two circular arcs with identical radii, R, of 102.1 cm and subtended angles, $\theta_{max}/2$, of 30°. Both arcs lie in the x-z plane. The centerline coordinates, given by Equations III.1, III.2 and III.3, are indicated by the dashed line in Figure III.4. All cross sections perpendicular to the centerline are circular. The duct inlet radius, r_1, is 10.21 cm. The duct exit radius, r_2, is 12.57 cm. This produces an area ratio, A_2/A_1, of 1.52. The variation of the duct radius as a function of the angle θ is given by Equation III.4. The duct

is larger than, but geometrically similar to, the duct tested by Vakili *et al.* [9].

$$x_{cl} = \begin{cases} R \sin\theta & 0 \leq \theta \leq \theta_{max}/2 \\ 2R \sin(\theta_{max}/2) - R \sin(\theta_{max} - \theta) & \theta_{max}/2 \leq \theta \leq \theta_{max} \end{cases} \tag{III.1}$$

$$y_{cl} = 0 \tag{III.2}$$

$$z_{cl} = \begin{cases} R \cos\theta - R & 0 \leq \theta \leq \theta_{max}/2 \\ 2R \cos(\theta_{max}/2) - R(1 + \cos(\theta_{max} - \theta)) & \theta_{max}/2 \leq \theta \leq \theta_{max} \end{cases} \tag{III.3}$$

$$\frac{r}{r_1} = 1 + 3\left(\frac{r_2}{r_1} - 1\right)\left(\frac{\theta}{\theta_{max}}\right)^2 - 2\left(\frac{r_2}{r_1} - 1\right)\left(\frac{\theta}{\theta_{max}}\right)^3 \tag{III.4}$$

When discussing results, axial position refers to the distance to cross-stream planes normalized by the inlet diameter, measured along the duct centerline, beginning at the start of curvature. Positions within any cross-stream plane are specified by the polar angle ϕ, measured from the positive z-axis, and the radial distance r from the centerline. Finally, the S-duct is fixed to the coordinate system shown in Figure III.4.

The duct was milled from two separate blocks of aluminium and had a final tolerance of ±0.0127 cm. After milling, the two halves were mated together and sanded using 120 grit Emory cloth until all machining imperfections were removed. The surface was then polished. The interior split line, located on the vertical centerline plane, was flush to touch and invisible to sight.

Instrumentation and Measurement Techniques

The flow field was investigated with several different techniques. Flow visualization and wall static pressures were obtained on the S-duct surface. Three- and five-hole pressure probes were used to determine total pressures, static pressures and the velocity field. Each measurement technique is briefly explained within this section.

Surface flow visualization

Surface flow fields can be visualized by applying fluorescent oil to a duct wall and then observing streakline patterns which develop. The method is especially advantages to use when nearly steady state flow conditions exist. In general, regions of streamwise reversed

flow and boundary layer cross flows can be identified with this technique. The location of flow separation and appreciable cross-stream pressure gradients can then be deduced.

The assumption made with surface oil flow visualization is that the oil streaklines follow the flow streamlines near the surface of the duct. Squire [22] concluded that oil streaklines follow the boundary layer surface streamlines except near separation. During separation, either in compressible or incompressible flows, the oil tends to form an envelope slightly upstream of the true separation region. However, this premature indication of flow separation is less marked for turbulent than for laminar boundary layers. Squire [22] also determined that the effect of the oil on the boundary layer flow is negligible in most practical cases. Reichert *et al.* [23] have had success using a variation of this technique to visualize subsonic flow in a circular-to-rectangular transition duct. Davis *et al.* [24] have also successfully used a thin-oil-film method to investigate near wall flow behavior in hypermixing nozzles.

For this study, a mixture of fluorescent commercial powder dye (Rocket Red : Day-Glow Color Corporation) and petroleum-base lubricating oil (STP 140 wt.) was prepared. Slight thinning of this mixture with mineral oil was needed depending on the amount of powder dye used. The mixture was applied to the surface in small dots. This small-dot application method (proposed by Wendt [25]) appeared to be an improvement to the film technique utilized by Reichert *et al.* [23]. After oil application, the duct was quickly assembled for testing. Surface oil streakline patterns developed when air was drawn through the duct. The patterns corresponded to surface flow direction and shear intensity. The duration of the test, at the desired flow rate, was ten minutes. Following rapid shut down, the duct was disassembled in order to observe the streaklines under the illumination of ultraviolet light. The patterns were photographed with a 35mm camera using 400 ASA color film. An UV filter was used to reduce the glare produced by the reflection of the ultraviolet light from the surface.

Pressure measurements

The test section was instrumented to obtain mean pressure measurements. Total and static pressures were measured in cross-sectional planes with three- and five-hole pneumatic probes. Surface static pressures were acquired with wall taps. The pressure instrumentation and measurement system are described in this section.

Table III.1 Experimental measurement plane information

Plane	A	B	C	D	E
Location, s/d	-0.50	0.96	2.97	4.01	5.73
Radial Traverses	10	11	11	11	19
Measurement Points	590	462	506	539	930

Probe pressure measurements The flow field was measured with calibrated three-and five-hole probes. Data were accumulated in five measurement planes, each perpendicular to the duct centerline. The measurement plane locations along the duct centerline are presented in Table III.1. These planes are also depicted by the shaded cross sections in Figure III.5. At each measurement plane the S-duct contained probe port holes, allowing access to the flow. The number of radial traverses and measurements made in each plane are given in Table III.1. Representative schematics depicting the location of probe port holes and measurement points are shown in Figures III.6 (Plane A) , III.7 (Planes B, C and D), and III.8 (Plane E). Traversing intervals in the radial direction were approximately 0.254 cm for all measurement planes. In Planes A and E, traversing intervals near the surface were 0.0635 cm. Reported flow measurements were concentrated in only one symmetric half of the duct.

A calibrated three-hole probe was used in Plane A, since a nearly one-directional velocity field existed there. The three-hole probe allowed total pressure and static pressure and two components of velocity to be measured. A yaw-nulling measurement method was utilized. The three-hole probe calibration method and data reduction technique are presented in Appendix A.

A calibrated five-hole probe was used in Planes B, C, D and E, enabling total pressure, static pressure and three components of velocity to be measured. Both yaw-nulling and non-yaw-nulling measurement methods were employed. The five-hole probe calibration methods and data reduction procedures are presented in Appendix B.

Surface static pressure measurements A total of 220 static pressure taps were located on the surface of the duct. The taps were constructed by locally drilling a 0.143 cm diameter hole normal to the duct surface. Each hole was plugged with an appropriate size aluminium tube having an inside diameter of 0.0813 cm. Epoxy placed on the outside of the

duct sealed the interface between duct and tube . The tube was sanded flush with the inside duct surface. A drawing representing a typical static tap is shown in Figure III.9.

The static taps were distributed in the streamwise and circumferential directions. Three lines of taps ran in the streamwise direction. These streamwise lines were at constant angles of ϕ = 10°, 90°, and 170°. Measurements at ϕ = 0° and 180° were impossible because of the flanges there. The streamwise taps were spaced every s/d = 0.0873, beginning at s/d = 0.3492. A total of 53 taps were in each streamwise line. Four lines of taps ran in the circumferential direction. These circumferential taps were in Planes A, B, C and D. Plane

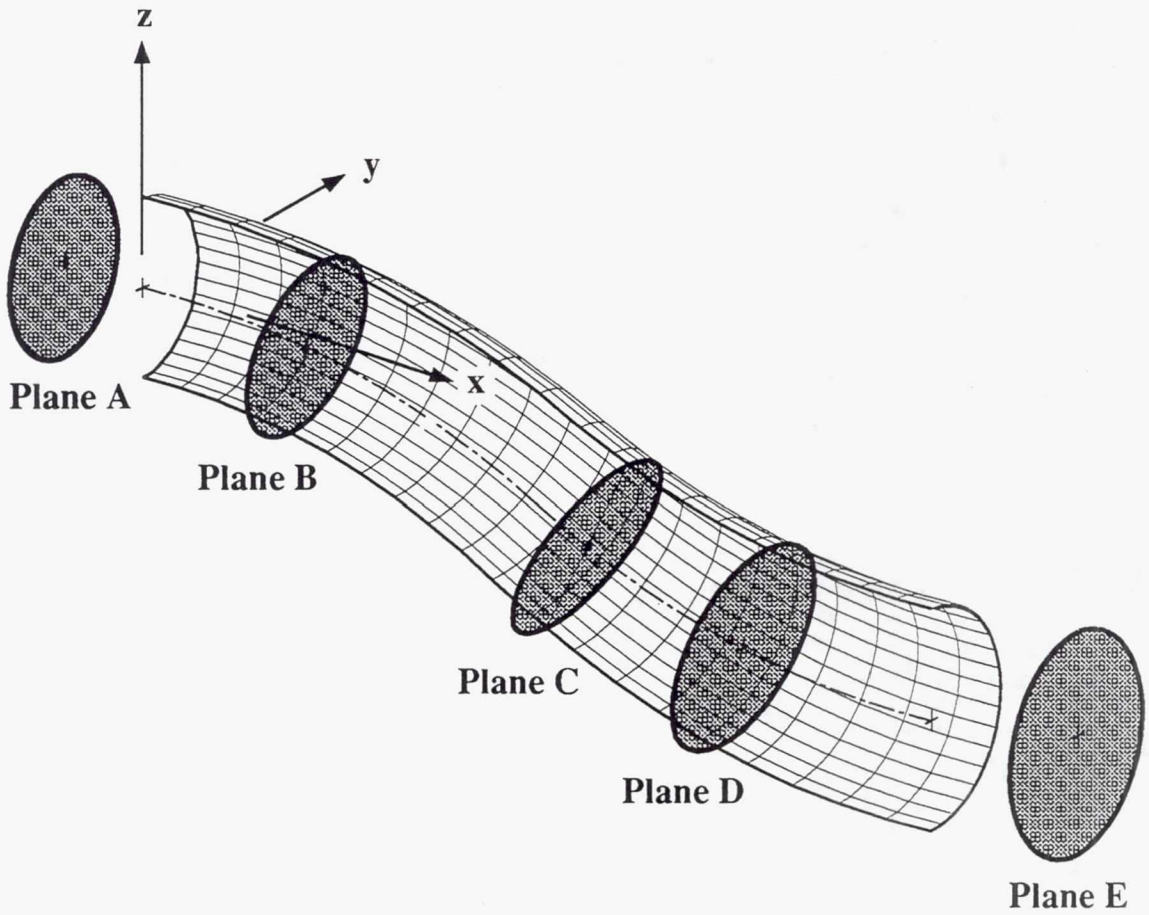

Figure III.5 Half shell representation of the diffusing S-duct indicating the measurement plane locations

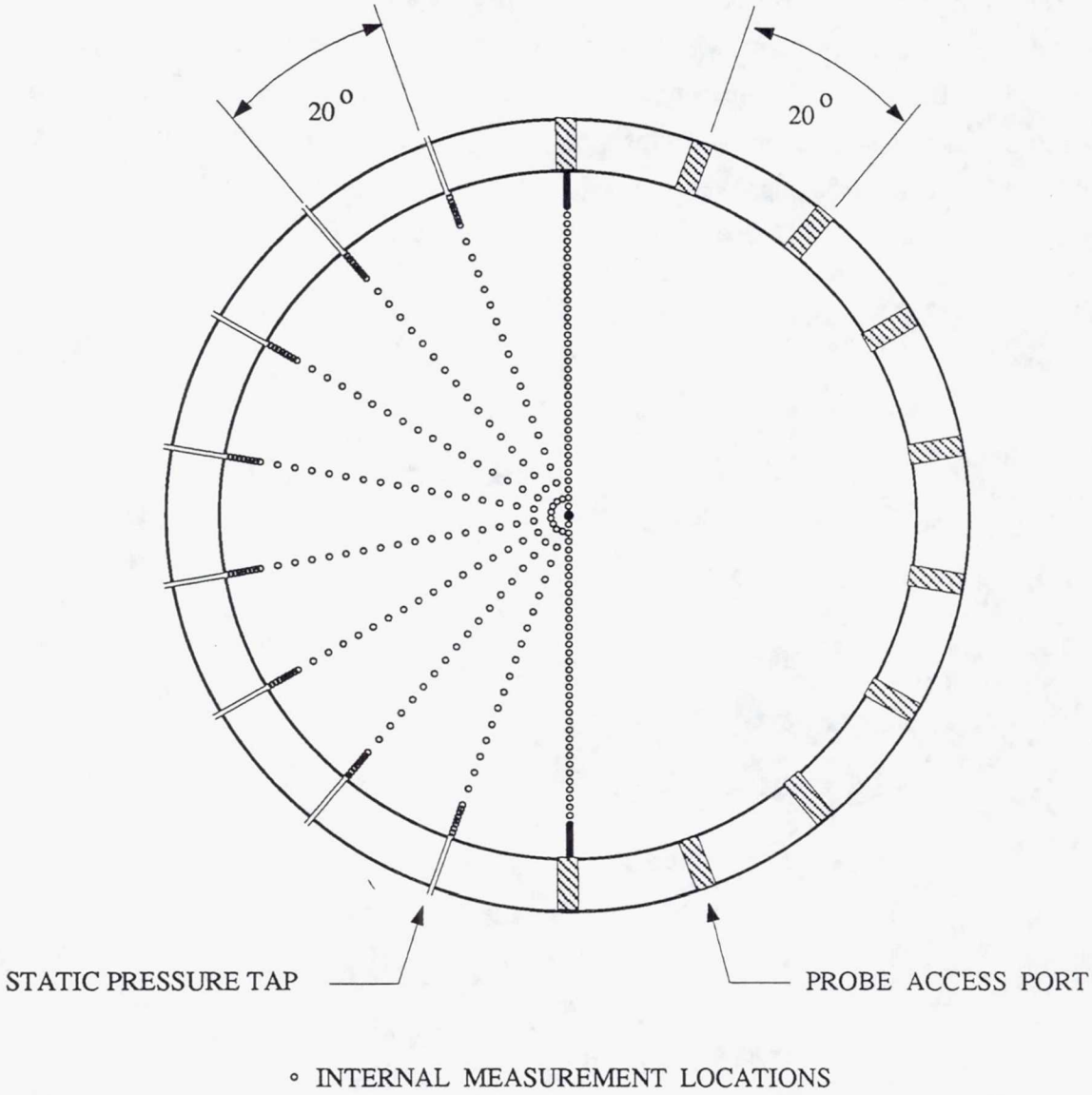

Figure III.6 Measurement plane schematic for Plane A

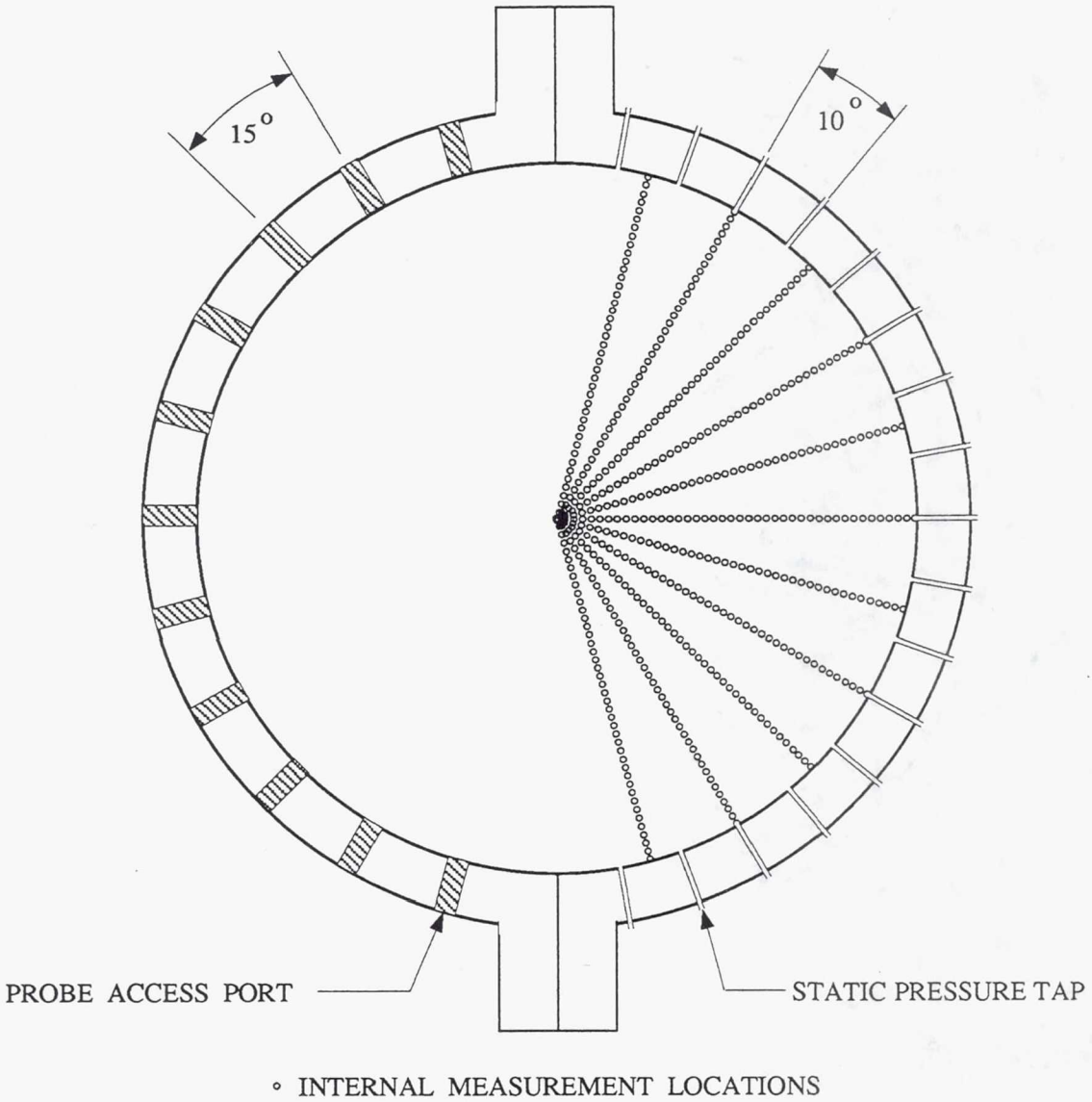

Figure III.7 Measurement plane schematic for Plane B, C and D

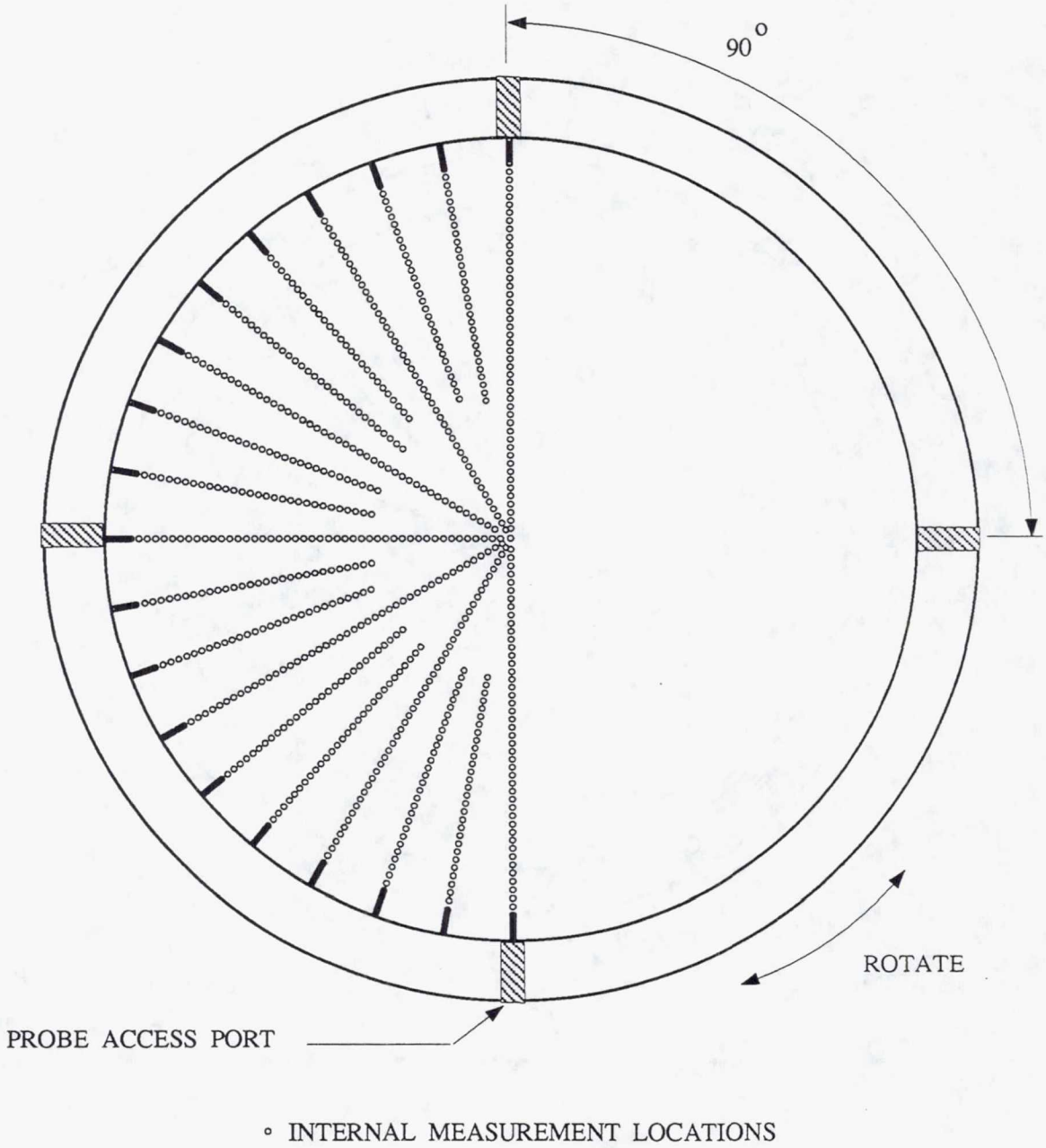

Figure III.8 Measurement plane schematic for Plane E

E was void of static taps. The circumferential static tap distribution is shown in Figure III.6 for Plane A and in Figure III.7 for Planes B, C and D.

Pressure measurement system A PSI Model 780B/T measurement system [26] was used to acquire all pressure data. The PSI system was a fully integrated measurement instrument consisting of electronically scanned pressure sensors and a microcomputer based data acquisition system. Individual pressure transducers provided high data acquisition rates for multiple pressure measurements. The accuracy of the system was maintained by frequent on-line calibrations of all transducers, performed transparently to the user at 20 minute intervals. After acquisition, information was carried by Escort, a data routing network, to a storage area for later post-processing on Sun SPARCstations.

The PSI system contained four major components: the system controller, the data acquisition and control unit (DACU), the pressure calibration unit (PCU), and the sensor

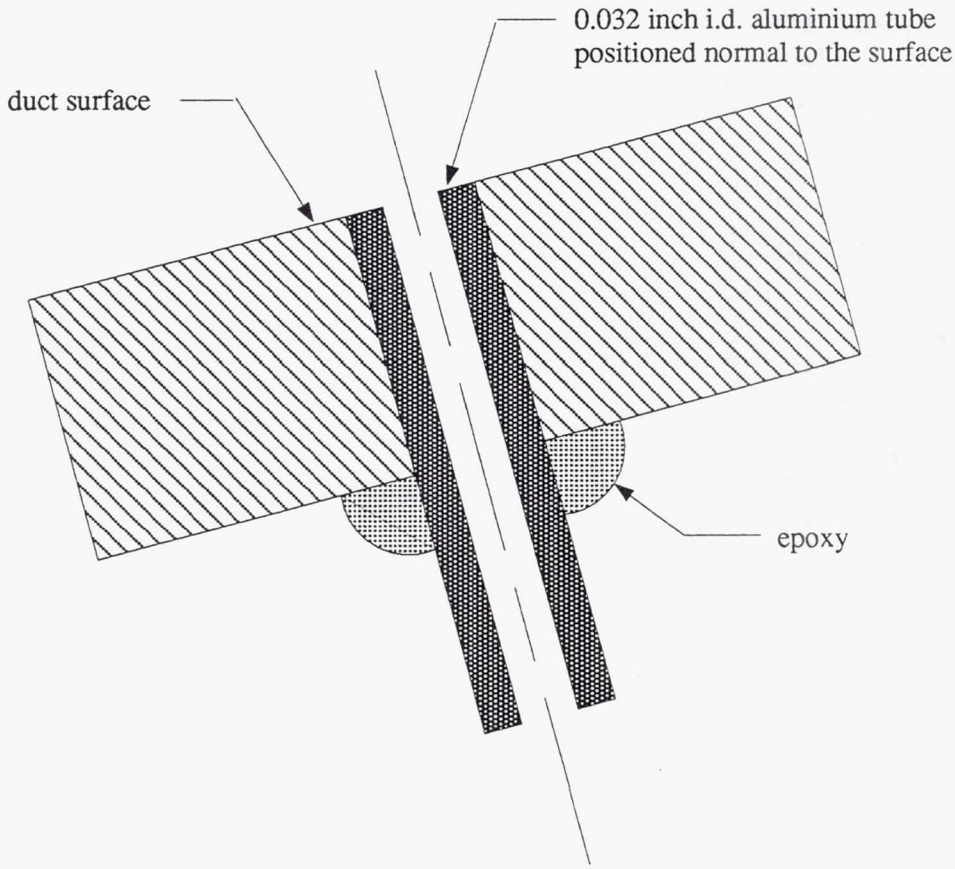

Figure III.9 Static tap mounting procedure schematic

modules. The system controller interfaced the user to the DACU and directed the data flow within the system. The DACU managed the data acquisition functions and was controlled by an eight bit microprocessor. The DACU also interfaced with the PCU and reduced the transducer calibration data. The PCU applied the three point calibration to all transducers. It consisted of pneumatic valves and a highly accurate Digiquartz 103 KPa absolute pressure transducer (accurate to within ± 0.02% full span). The Digiquartz transducer was used to calibrate the individual measurement transducers. Sensor modules were simply the link between the physical pressures and the electronic signals. Each module contained 32 individual sub-atmospheric differential pressure transducers having a full scale range of 34.5 KPa referenced to atmospheric pressure. The inaccuracy of an individual transducer was less than ± 0.10% of the full span.

CHAPTER IV

COMPUTATIONAL ANALYSIS

A second goal of this study was to numerically approximate the flow through the test S-duct. For the objectives of this thesis, a parabolized Navier-Stokes algorithm (PNS) was considered appropriate. In this chapter the formulation of governing equations, numerical procedure, grid generation and boundary conditions are described.

Formulation of Equations

Parabolized Navier-Stokes equations represent a mathematical model of three-dimensional viscous flows. PNS equations are intermediate in complexity between potential flow equations and full Navier-Stokes equations. PNS algorithms predict three-dimensional flow fields by solving a sequence of two-dimensional cross-stream governing equations while marching in the primary flow direction. This simplified solution procedure decreases computational time and storage requirements.

For subsonic flows, the PNS equations are classified as partially-parabolized Navier-Stokes (P-PNS) equations. P-PNS equations are applicable for internal flows in which a predominant flow direction exists. P-PNS equations are derived from the steady Navier-Stokes equations by neglecting the effect of momentum diffusion in the streamwise direction. This approximation represents an attempt to make use of the experimentally observed fact that small disturbances at a given point, in a high Reynolds number ducted flow, are not transmitted very far up stream by viscous diffusion from that point. P-PNS equations also require that an initial approximation to the static pressure field is known a priori. This prerequisite incorporates elliptical influences, associated with subsonic flows, and static pressure gradients, associated with streamline curvature, into the solution. The initial static pressure distribution can be obtained from a solution to the velocity potential equation (Equation IV.1) for a given duct geometry. Here, the local speed of sound, a, in Equation IV.1 is given in Equation IV.2, where a_o is constant.

$$\left[1-\frac{1}{a^2}\left(\frac{\partial\Phi}{\partial x}\right)^2\right]\frac{\partial^2\Phi}{\partial x^2}+\left[1-\frac{1}{a^2}\left(\frac{\partial\Phi}{\partial y}\right)^2\right]\frac{\partial^2\Phi}{\partial y^2}+\left[1-\frac{1}{a^2}\left(\frac{\partial\Phi}{\partial z}\right)^2\right]\frac{\partial^2\Phi}{\partial z^2}$$

$$-\frac{2}{a^2}\left(\frac{\partial\Phi}{\partial x}\right)\left(\frac{\partial\Phi}{\partial y}\right)\frac{\partial^2\Phi}{\partial x\partial y}-\frac{2}{a^2}\left(\frac{\partial\Phi}{\partial x}\right)\left(\frac{\partial\Phi}{\partial z}\right)\frac{\partial^2\Phi}{\partial x\partial z}-\frac{2}{a^2}\left(\frac{\partial\Phi}{\partial y}\right)\left(\frac{\partial\Phi}{\partial z}\right)\frac{\partial^2\Phi}{\partial y\partial z}=0 \tag{IV.1}$$

$$a^2=a_o^2-\frac{\gamma-1}{2}\left[\left(\frac{\partial\Phi}{\partial x}\right)^2+\left(\frac{\partial\Phi}{\partial y}\right)^2+\left(\frac{\partial\Phi}{\partial z}\right)^2\right] \tag{IV.2}$$

P-PNS equations are valid in both the inviscid and viscous portions of the flow field, with the interaction between these regions automatically taken into account. One important restriction of the model is that the velocity component in the primary flow direction must be greater than zero. Hence, no flow reversal in the streamwise direction is permitted. No restrictions are placed on cross-flow velocities. Mathematically, partially-parabolized Navier-Stokes models can be represented by Equations IV.3–IV.8 for a Cartesian system where the x-component is in the direction of primary flow.

$$\frac{\partial\rho u}{\partial x}+\frac{\partial\rho v}{\partial y}+\frac{\partial\rho w}{\partial z}=0 \tag{IV.3}$$

$$\int_A \rho u\, dA = constant \tag{IV.4}$$

$$u\frac{\partial u}{\partial x}+v\frac{\partial u}{\partial y}+w\frac{\partial u}{\partial z}=-\frac{1}{\rho}\frac{d(P+p_m)}{dx}+\frac{1}{\rho}\left[\frac{\partial}{\partial y}\left(\mu\frac{\partial u}{\partial y}\right)+\frac{\partial}{\partial z}\left(\mu\frac{\partial u}{\partial z}\right)\right] \tag{IV.5}$$

$$\begin{aligned}u\frac{\partial v}{\partial x}+v\frac{\partial v}{\partial y}+w\frac{\partial v}{\partial z}&=-\frac{1}{\rho}\frac{d(P+p)}{dy}\\&+\frac{1}{\rho}\left[\frac{4}{3}\frac{\partial}{\partial y}\left(\mu\frac{\partial v}{\partial y}\right)+\frac{\partial}{\partial z}\left(\mu\frac{\partial v}{\partial z}\right)-\frac{2}{3}\frac{\partial}{dy}\left(\mu\frac{\partial w}{\partial z}\right)+\frac{\partial}{dz}\left(\mu\frac{\partial w}{\partial y}\right)\right]\end{aligned} \tag{IV.6}$$

$$u\frac{\partial w}{\partial x} + v\frac{\partial w}{\partial y} + w\frac{\partial w}{\partial z} = -\frac{1}{\rho}\frac{d}{dz}(P+p)$$
$$+ \frac{1}{\rho}\left[\frac{4}{3}\frac{\partial}{\partial z}\left(\mu\frac{\partial w}{\partial z}\right) + \frac{\partial}{\partial y}\left(\mu\frac{\partial w}{\partial y}\right) - \frac{2}{3}\frac{\partial}{dz}\left(\mu\frac{\partial v}{\partial y}\right) + \frac{\partial}{dy}\left(\mu\frac{\partial v}{\partial z}\right)\right] \tag{IV.7}$$

$$u\frac{\partial H}{\partial x} + v\frac{\partial H}{\partial y} + w\frac{\partial H}{\partial z} = -\frac{1}{\rho}\left[\frac{\partial}{\partial y}\left(k\frac{\partial T}{\partial y}\right) + \frac{\partial}{\partial z}\left(k\frac{\partial T}{\partial z}\right)\right]$$
$$+ \frac{1}{\rho}\frac{\partial}{\partial y}\left\{\mu\left[\left(\frac{4}{3}\frac{\partial v}{\partial y} - \frac{\partial w}{\partial z}\right)v + \left(\frac{\partial v}{\partial z} + \frac{\partial w}{\partial y}\right)w\right]\right\} \tag{IV.8}$$
$$+ \frac{1}{\rho}\frac{\partial}{\partial z}\left\{\mu\left[\left(\frac{\partial v}{\partial z} + \frac{\partial w}{\partial y}\right)v + \left(\frac{4}{3}\frac{\partial w}{\partial z} - \frac{\partial v}{\partial y}\right)w\right]\right\}$$

$$\rho = f_1(p,T), \quad \mu = f_2(T), \quad k = f_3(T) \tag{IV.9}$$

The continuity equation, given in Equation IV.3, is applicable at all points in the flow field. The momentum equations are represented by Equations IV.5–IV.7. Here, the static pressure at a point is the sum of, P, p_m and p. The pressure, P, is the initial static pressure obtained from the potential flow solution. The components of its gradient are treated as source terms during the solution process. The mean streamwise pressure, p_m, (Equation IV.5) is assumed to vary only in the streamwise direction and is determined with the aid of a global mass flow constraint (Equation IV.4). In contrast, the cross-stream pressure, p, in Equations IV.6 and IV.7, is permitted to vary across the channel. This uncoupling procedure assumes that small pressure variations across the channel have negligible effects on the streamwise momentum equation. The energy equation, given in Equation IV.3, can be solved uncoupled from the momentum equations stated above for a constant stagnation enthalpy. Finally, state equations are needed to relate thermodynamic variables and transport properties as shown in Equation IV.9.

Numerical Procedure

The original source code, PEPSIG, used in this thesis was developed by Scientific Research Associates under NASA Lewis Research Center sponsorship. Modifications to

the code have been incorporated by Levy *et al.* [27], Briley and McDonald [28] and Anderson [29]. Further alterations to the code were performed by Wellborn [30], enabling the algorithm to run efficiently on UNIX workstations. Solutions to the PNS equations, by PEPSIG, were obtained with a two step process. A potential flow solution was first computed to approximate the static pressure field. Viscous calculations were performed next by marching once through in the primary flow direction.

The potential flow numerical procedure involved solving the three-dimensional velocity potential equation, given in Equation IV.1, including all cross derivatives on body fitted coordinates. A general purpose three-dimensional scalar finite-difference alternating-directional implicit (ADI) algorithm was used to solve Equation IV.1. The three-dimensional approximate factorization technique of Douglas-Gunn was used to generate the ADI scheme from a basic Crank-Nicolson spatial differencing. The Douglas-Gunn scheme separated the three-dimensional operator into one-dimensional components and therefore split each iteration level into three steps, each step involving the implicit operations originating from a single coordinate. A simple tri-diagonal system resulted for each of the three steps. The potential function was then solved for iteratively until convergence.

The viscous flow numerical procedure was based on the decomposition of the velocity field into primary and a secondary velocities. The primary velocity was determined from the streamwise momentum equation. The streamwise static pressure gradients were approximated from the inviscid flow solution. The one-dimensional, streamwise static pressure gradient correction was determined by ensuring global conservation of mass. These pressure gradients were treated as source terms in the streamwise momentum equation. The two-dimensional approximate factorization technique of Douglas-Gunn was used to create an ADI scheme which calculated the new primary velocity field. The secondary velocity was determined from a vector potential equation and a vorticity transport equation. A coupled ADI procedure was used to update these velocities. Corrections to these updated velocities were then computed. These correction velocities were assumed to be irrotational and ensured the difference form of the continuity equation was satisfied. Static pressures were then updated with the cross-stream momentum equations. FLARE approximations were used in regions of the flow field where the primary velocity was in the negative streamwise direction. The turbulent boundary layer was approximated by an algebraic turbulence model. The eddy mixing length was determined from an empirical relationship developed by McDonald and Camarata [31]

for equilibrium turbulent boundary layers. The equation of state for a perfect gas and a known constant stagnation energy closed the system of equations.

The basic algorithm for PEPSIG is presented below. The input parameters are documented in Reference [32] and therefore not listed here. All governing equations were solved on a body fitted computational coordinate system.

Inviscid Calculation

- Generate a three dimensional grid
- Solve velocity potential equation to obtain a static pressure field
- Store pressure field

Viscous Calculation

- Generate a two-dimensional cross-stream grid
- Solve primary momentum equation to update primary velocity
- Solve vector potential and vorticity equations to update cross-channel velocities
- Solve scalar potential equation to correct the cross-channel velocities
- Solve Poisson pressure equation to correct the cross-stream pressures
- Solve energy equation (if needed)
- Step to next plane and start viscous calculation over again

Grid Distributions

Two computational meshes existed for the numerical solution. The grid distributions used contained the maximum number of grid points allowed by the limited size of the computer memory. Both meshes modeled the experimental S-duct and were made with an algebraic grid generator.

The potential solution utilized $50 \times 19 \times 10$ grid points in the streamwise, circumferential and radial directions. An O-grid was implemented in the cross-stream plane. The O-grid was equally spaced in radial and circumferential directions. The centerline coordinates of the experimental S-duct were defined with a tenth degree polynomial which was a least-squares approximation of Equations III.1, III.2 and III.3. The variation of radius in the streamwise direction was given by Equation III.4. The cross-sectional and streamwise distributions for the potential grid are shown in Figure IV.1.

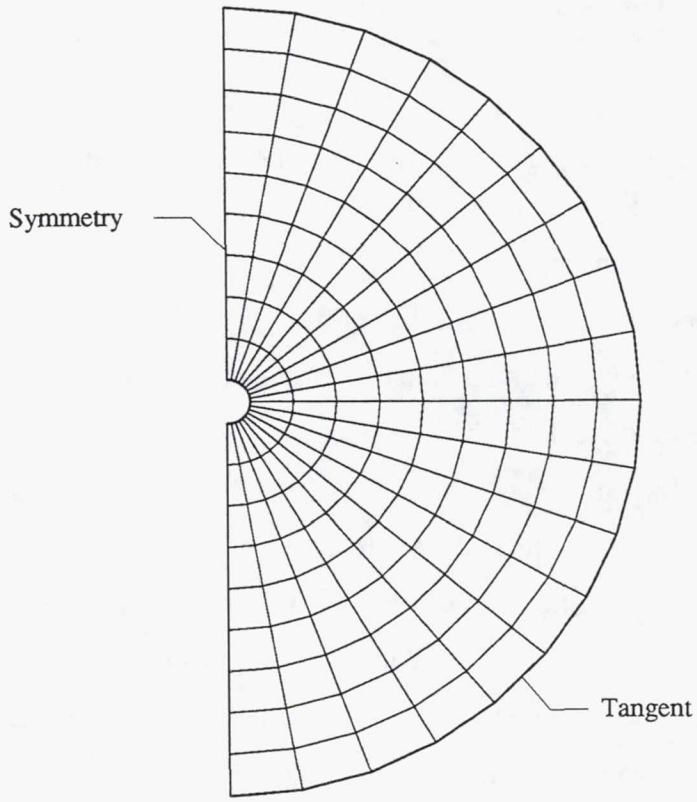

a) Cross-sectional view

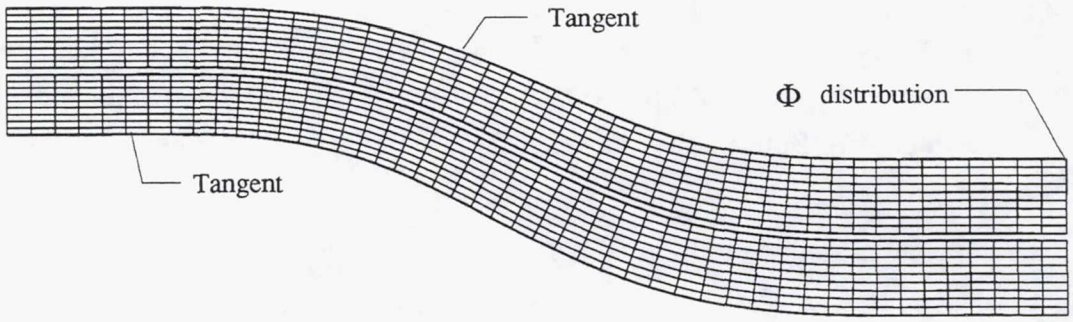

b) Streamwise view

Figure IV.1 Computational mesh distribution for the potential solution

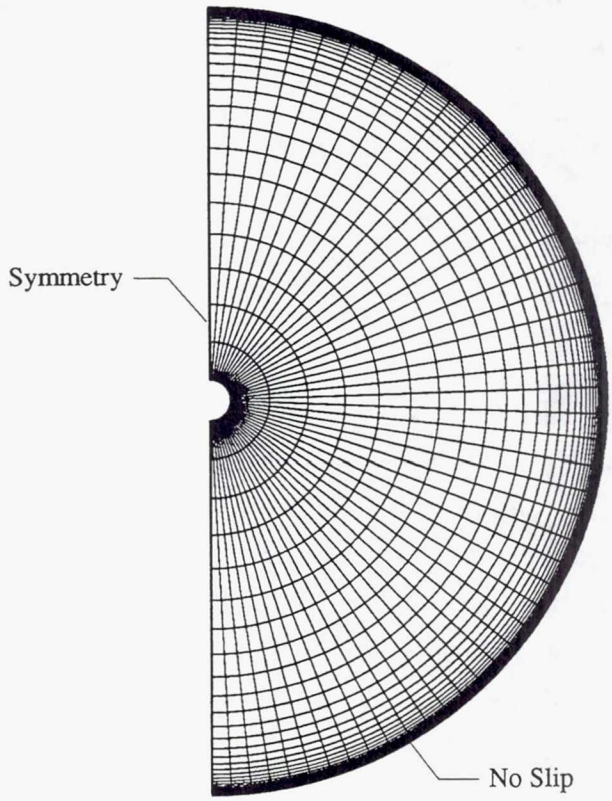

a) Cross-sectional view

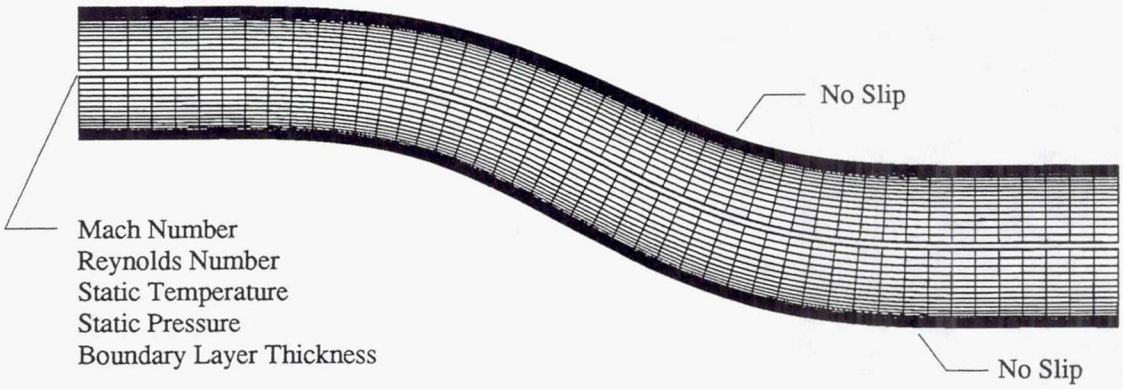

b) Streamwise view

Figure IV.2 Computational mesh distribution for the viscous solution

The viscous solution utilized $77 \times 49 \times 49$ grid points in the streamwise, circumferential and radial directions. Again, an O-grid was implemented in the cross-stream plane. However, stretching was used in both the circumferential and radial directions. In the radial direction, clustering near the duct surface was used to resolve the boundary layer. In the circumferential direction, clustering near $\phi = 180°$ was used to help enhance the calculations in the separated flow region. The variation of radius in the streamwise direction is given by Equation III.4. The streamwise positions were defined by the same polynomial used for the potential solution. The cross-sectional mesh and a representative streamwise distribution for the viscous grid are shown in Figure IV.2.

Boundary Conditions

Two sets of boundary conditions were used for the numerical solutions. The potential solution met a flow tangency condition on the duct surface. Zero gradients of the Φ function along the plane of symmetry were also satisfied. To achieve zero gradients, a reflective boundary at the plane of symmetry was assumed. The centerline was considered a pole boundary. A uniform flow distribution existed at both the inlet and exit. The downstream potential distribution, Φ, was specified. These conditions are indicated in Figure IV.1.

For the viscous solution, no slip on the duct wall and zero gradients along the plane of symmetry were used. Again, a reflective boundary at the plane of symmetry was assumed and the centerline was considered a pole boundary. The centerline Mach number, Reynolds number, static temperature, static pressure and the initial boundary layer thickness at the first marching station were specified. These conditions are indicated in Figure IV.2.

CHAPTER V

INLET FLOW CONDITIONS

Test inlet flow conditions were obtained from a survey of the flow field one radius upstream of the first bend (Plane A in Figure III.5). All reported tests were conducted with an inlet centerline Mach number of 0.6. The Reynolds number, based on the inlet diameter and centerline velocity, was 2.6×10^6. Hot wire measurements were previously gathered by Reichert [33] to ascertain the turbulence intensity at the centerline in Plane A. Measurements were made for Mach numbers ranging from 0.05 to 0.5 and for five overheat ratios. A 50Khz data acquisition sampling rate was used. The centerline turbulence intensity in Plane A for Reichert's study [33] was nominally 0.65%, which was presumed to represent the inlet centerline turbulence intensity in this thesis.

A thin turbulent inlet boundary layer existed in Plane A. The boundary layer thickness, δ, was defined as being from the wall to where 95% of the free stream velocity was achieved. The displacement thickness, δ_1, momentum thickness, δ_2, and shape factor, H, used to further quantify the inlet flow conditions, are defined by Equations V.1–V.3. These boundary layer parameters were calculated by numerically integrating the survey data. The inlet flow conditions are listed in Table V.1.

$$\delta_1 = \int_0^{r_1} \left(1 - \frac{\rho u}{\rho_{cl} u_{cl}}\right) r dr \tag{V.1}$$

$$\delta_2 = \int_0^{r_1} \frac{\rho u}{\rho_{cl} u_{cl}} \left(1 - \frac{u}{u_{cl}}\right) r dr \tag{V.2}$$

$$H = \frac{\delta_1}{\delta_2} \tag{V.3}$$

A representative inlet velocity profile, plotted in nondimensional law-of-the-wall coordinates, is shown in Figure V.1. The friction velocity, used to define law-of-the-wall coordinates, was not measured but instead was chosen to provide the best approximation of the linear profile region of the test data to the law-of-the-wall logarithmic function. Comparisons indicate little deviation from a conventional turbulent boundary layer.

Table V.1 Experimental and computational flow conditions in Plane A

Inlet Parameter	Experimental	Computational
M_{cl}	0.60	0.60
Re_{cl}	2,600,000	2,600,000
$(\delta/r_1) \times 100$	6.95	4.45
$(\delta_1/r_1) \times 100$	1.46	0.71
$(\delta_2/r_1) \times 100$	1.06	0.53
H	1.38	1.35

The numerical solution started two inlet diameters upstream of Plane A. Therefore, computational input parameters corresponded to flow variables at that position while test flow conditions pertained to flow variables in Plane A. This posed a problem when defining the computational input parameters. In practice it was very difficult to chose the input parameters which gave an exact match of all computational flow conditions in Plane A to the test flow conditions. The numerical and test flow values of Mach and Reynolds numbers in Plane A were equal. However, exact matching of computational and experimental flow boundary layer flow parameters in Plane A was unfortunately not attained. The computational flow conditions for Plane A are listed in Table V.1.

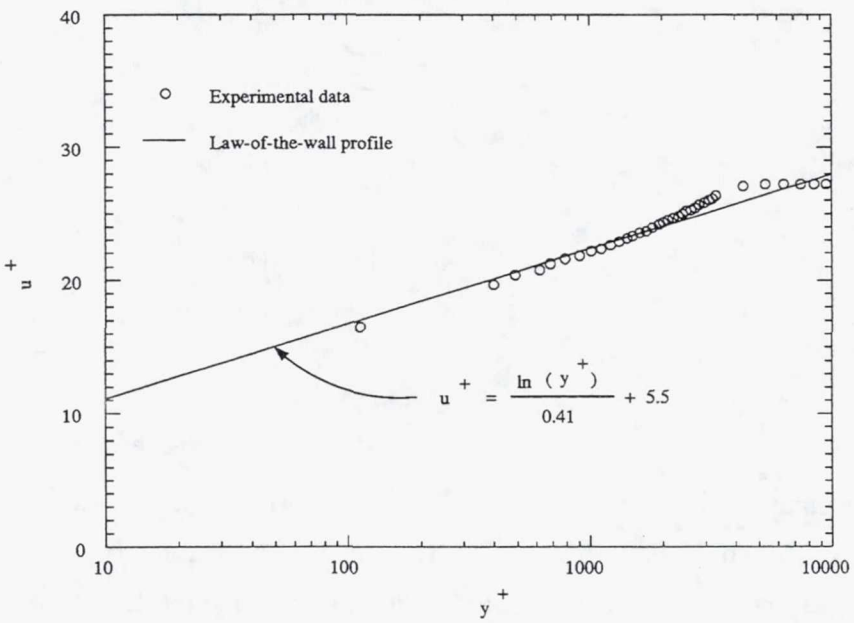

Figure V.1 Experimental law-of-the-wall velocity profile measured at Plane A

CHAPTER VI

RESULTS AND DISCUSSION

All data presented in this chapter are in nondimensional form. Aerodynamic results represent mean values of measurements. Pressures are presented as total and static pressure coefficients, which are defined by Equations VI.1 and VI.2. The pressures p_o and p represent local values of total and static pressures. Inlet centerline conditions define the reference states $p_{o,cl}$ and p_{cl}. Three dimensional velocity components were converted to local Mach vectors and normalized by the inlet centerline Mach number, as shown in Equation VI.3. Finally, streamwise vorticity, given in Equation VI.4, was normalized by the ratio of inlet centerline velocity to inlet duct diameter.

$$C_{po} = \frac{p_o - p_{cl}}{p_{o,cl} - p_{cl}} \tag{VI.1}$$

$$C_p = \frac{p - p_{cl}}{p_{o,cl} - p_{cl}} \tag{VI.2}$$

$$\mathrm{M} = \frac{\mathrm{V}/c}{M_{cl}} \tag{VI.3}$$

$$\Omega_{\mathrm{s}} = \frac{\omega_{\mathrm{s}}\, d}{V_{cl}} \tag{VI.4}$$

For this section the nondimensional pressure coefficients, normalized Mach vector and normalized streamwise vorticity component will simply be referred to as total pressure, static pressure, velocity and vorticity. The velocity vector will be presented as normal and transverse components. The normal component is perpendicular to the measurement plane while the transverse component is parallel to the measurement plane. Transverse velocity components, originally on a polar grid, were interpolated onto a Cartesian mesh [33], in order to enable easy visualization and comparison of the cross-stream flow fields. Since data were measured and computed in only one half of the symmetrical duct flow, all cross-stream aerodynamic results were mirror imaged to enhance presentation.

Surface Streakline Patterns

Major test flow field characteristics near the duct wall were visualized with streaklines of fluorescent oil on the duct surface. Three conclusions were made from the streakline patterns. First, the flow was indeed symmetric. This was ascertained by applying a different color of dye to the surface of each symmetric duct half. The dye from each half remained separate and identical streakline patterns were present on each symmetric half of the duct. Symmetry is illustrated in Figure VI.2. Here, one symmetric half of the duct is shown connected to the exit extension. The flow is from left to right. Obviously, red dye from the left half of the duct does not mix with the green dye from the right half of the duct. This is true everywhere except along the vertical split line where there exists a thin line of yellow dye (mixed red and green dyes). Second, a large region of three-dimensional separated flow existed, as strikingly indicated in Figures VI.3 and VI.4. The entire duct section is shown in Figure VI.3, while Figure VI.4 is a close up of the separated flow region. The free stream flow is from left to right and each photo shows only one symmetric half of the observed streakline pattern. The separated flow region consisted of two saddle points, occurring on the duct split line ($\phi = 180°$), and two spiral nodes, lying in each symmetric duct half. The entire separated region was located on the lower duct wall. The onset of separation (upstream saddle point) was located at s/d = 2.02, while reattachment (downstream saddle point) occurred at s/d = 4.13. Three-dimensional separated flow terminology is explained in detail in Chapter VII. Third, boundary layer cross flows were present (Figure VI.3). In the first bend, streaklines were driven toward the lower surface ($\phi = 180^o$). In the second bend, streaklines near $\phi = 90^o$ diverged. The upper streaklines converged toward the top of the duct ($\phi = 0^o$), while the lower streaklines were directed toward the bottom of the duct ($\phi = 180^o$).

A qualitative assessment of the flow in the plane of symmetry (x-z plane) was acquired by temporarily introducing a splitter plate between the two symmetric duct halves. The plate was installed for only one test to produce streakline patterns on the plate. The S-duct surface results given above were obtained without the splitter plate in place. The splitter plate results are assumed to be qualitatively correct, even though the presence of the plate introduced additional shear into the flow. The streakline patterns produced on the splitter plate are presented in Figure VI.5. Free stream flow is from left to right. The location of separation and reattachment are identifiable. The streaklines follow the duct curvature in the first bend. Blockage caused by flow separation forced the streaklines to deviate from the curvature of

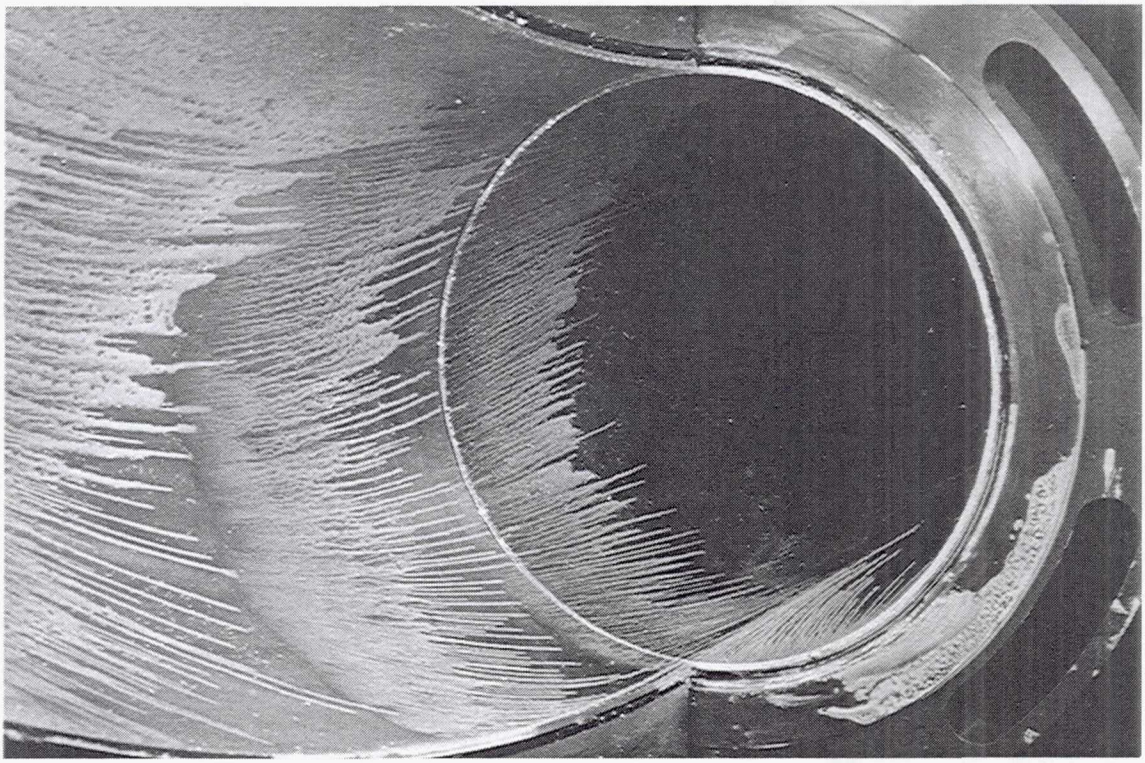

Figure VI.2 Surface oil flow patterns at the duct exit showing flow symmetry

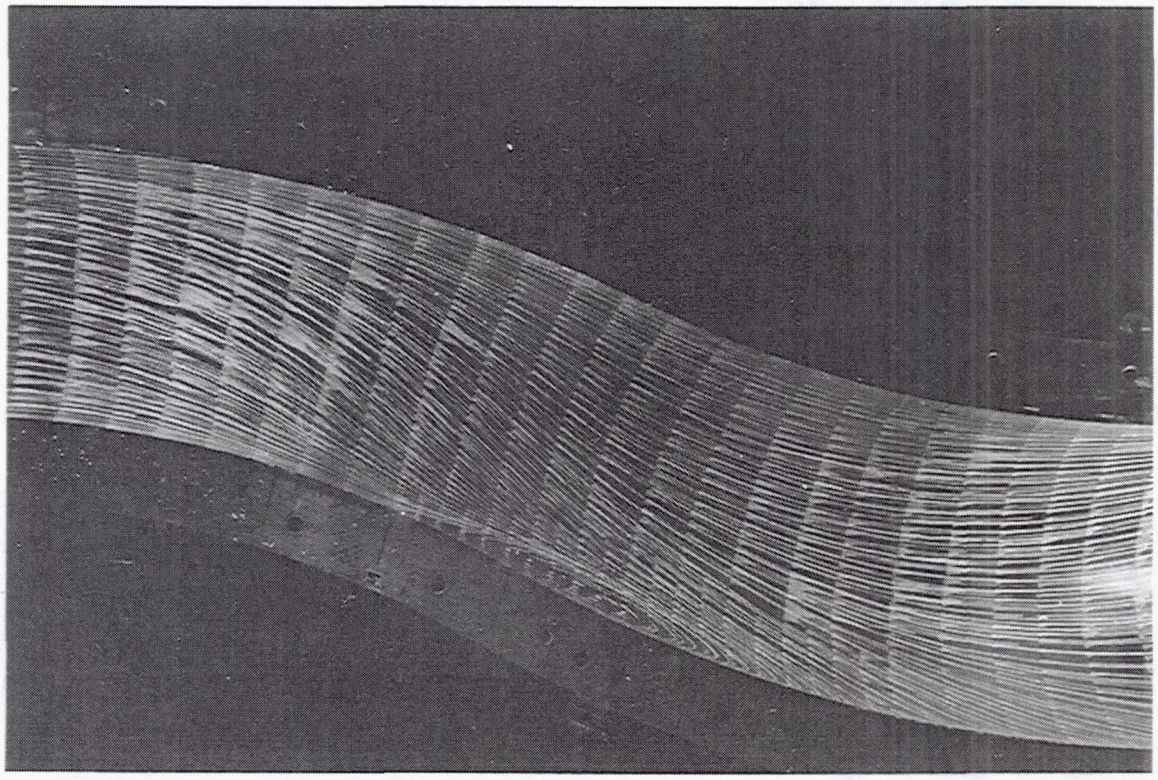

Figure VI.3 Surface oil flow patterns on one symmetric half of the duct surface

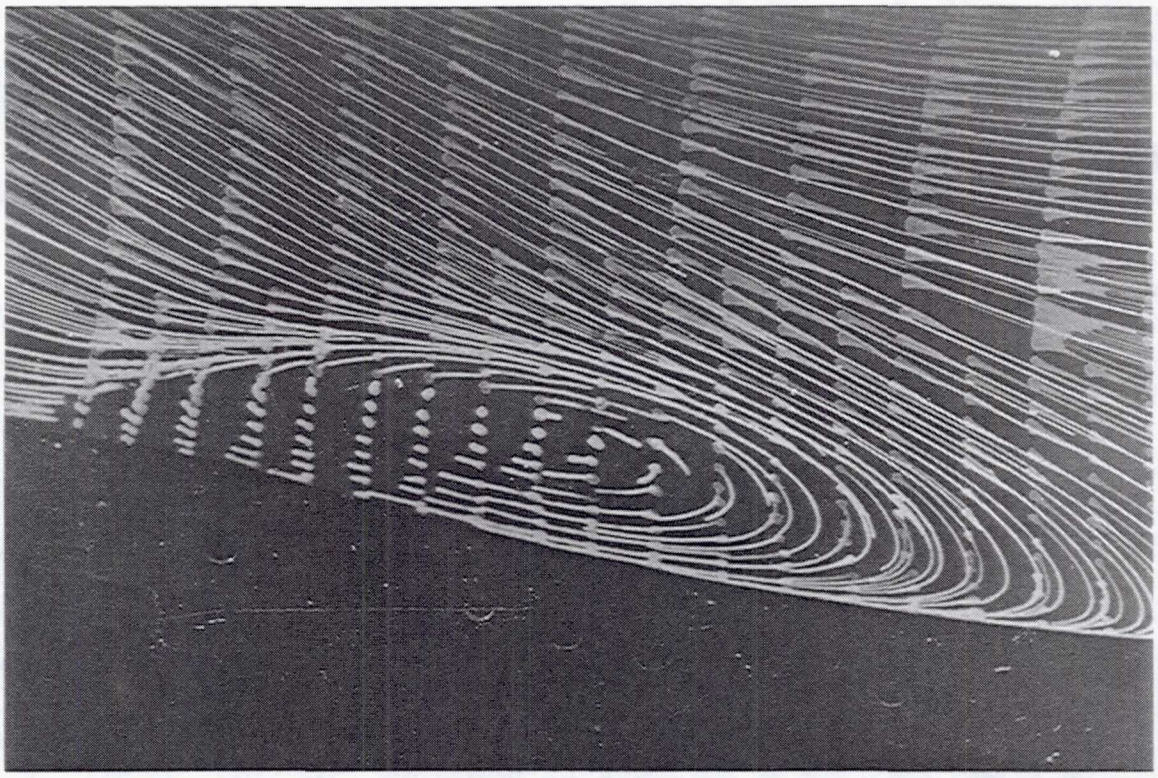

Figure VI.4 Close up of the surface oil flow patterns developed in the separation region

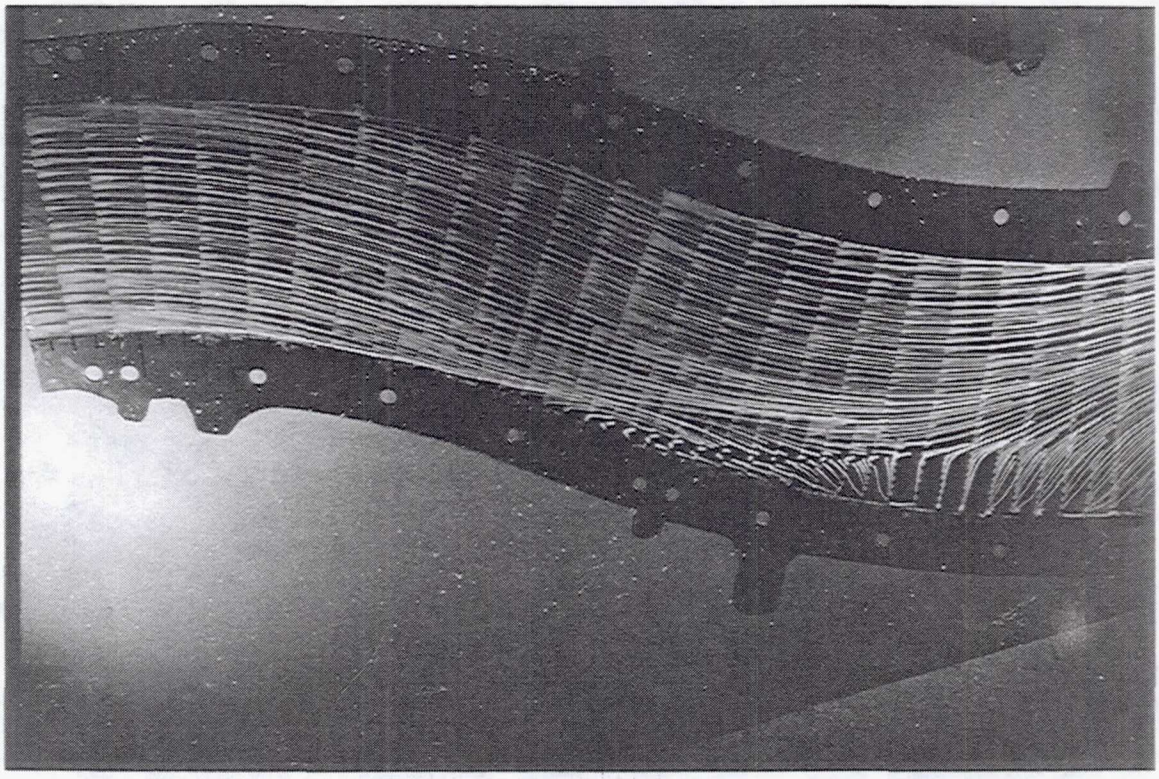

Figure VI.5 Surface oil flow patterns on the centerline splitter plate

the second bend. The reversed flow region began thin and grew until reattachment. The extensive bending of the streaklines at the exit of the duct was caused by viscous effects associated with the splitter plate. Cross-stream pressure gradients, at the duct exit, helped drive the boundary layer fluid on the splitter plate toward the top of the duct. This was most noticeable at the exit where the splitter plate boundary layer was thickest.

Surface Static Pressures

Symbols and lines in Figure VI.6 represent the experimental and computational surface static pressure variations with axial distance for three circumferential locations. The region of streamwise separated flow, deduced from flow visualization, and the corresponding computational separated flow region are also shown.

For the experimental measurements, the effects of streamline curvature and diffusion are clearly indicated within the first bend by the pressure difference between the $\phi = 10^o$ and the $\phi = 170^o$ data and the overall pressure rise. The influence of flow separation is shown

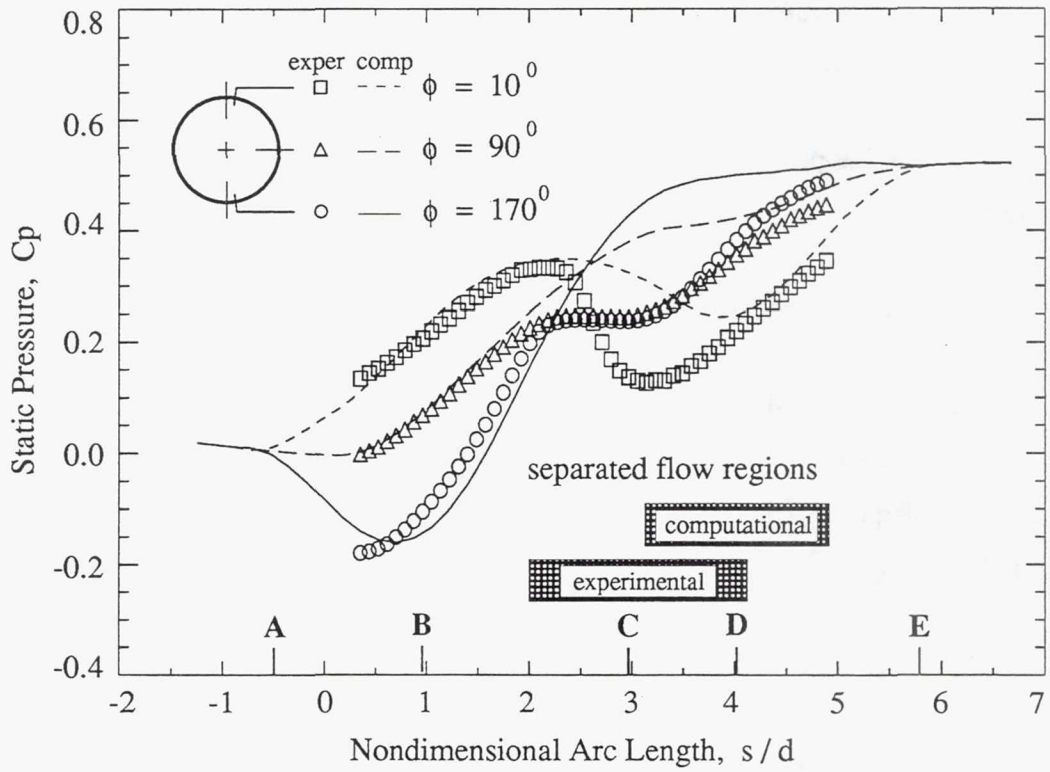

Figure VI.6 Axial distributions of surface static pressure for three circumferential positions

by the constant values of the $\phi = 90^o$ and 170° static pressures between $2.0 < s/d < 3.2$. The proximity of these two curves, between $2.0 < s/d < 3.2$, indicate only small changes in flow speed and/or direction in the lower half of the duct. Blockage caused by the separated flow also increased the favorable pressure gradient at $\phi = 10^o$. Static pressures at the three circumferential positions are nearly equal at $s/d = 2.6$. This suggests that a uniform static pressure distribution exits throughout the cross-stream plane there. Static pressure rose again for $s/d > 3.2$, even though the flow remained separated beyond this point, because the duct continued to diffuse the flow. After reattachment the pressure distributions converged to $Cp = 0.466$ far downstream ($s/d \approx 9.0$).

Computational results show the same distribution trends mentioned above for the static pressure measurements. Upstream of flow separation, streamline curvature and diffusion effects were evident. The computed static pressures at the three positions (10°, 90°, 170°) were nearly equal at $s/d = 2.6$, as with the test measurements. Downstream of the separated flow region, the pressure values converged to a single value, $Cp = 0.517$. The major discrepancies between computed and experimental results occurred within the second bend of the duct. The computed region of separated flow, $3.15 < s/d < 4.89$, was located further downstream than the experimental region. Also, the computed static pressure values at $\phi = 90^o$ and 170° did not coincide in this region as did the measured values. Numerical results of the static pressure distribution in this S-duct, reported by Harloff *et al.* [19], have been obtained using both algebraic and k-ϵ turbulence models with a FNS algorithm. The FNS results using both turbulence models within the second bend were similar to the P-PNS calculations. Therefore, errors caused by simplifications to the streamwise static pressure within the P-PNS equations are believed to be negligible when compared to the errors caused by the choice of turbulence models.

The circumferential distributions of surface static pressure in Planes A through D are presented in Figure VI.7. Symbols represent the experimental data. Lines indicate the computational results. The experimental and computational pressures for Plane A were nearly equal, both circumferentially and to each other. Essentially no influence of the duct curvature on the flow was detected at this upstream plane. The static pressure data in Figure VI.7 for Planes B, C and D all reflect the influence of streamline curvature. The pressures measured in Plane B were largest at $\phi = 10^o$ and continually decreased until $\phi = 170^o$. The values were negative for $\phi > 110^o$. Separation did not affect the flow field in Plane B. The distribution of computational and experimental static pressures at Plane B were similar. In

Planes C and D the cross-stream pressure distribution reversed from what it was in Plane B. Test measurements show that the separated flow reduced the static pressures at large values of ϕ in Planes C and D. The peak pressure location was shifted to a larger value of ϕ between Planes C and D. This trend indicates a reduction in size of the region of separated flow from Plane C to D. The computed pressure distributions, in Planes C and D, agreed in shape but were overall higher in level than the experimental pressures. This was attributed to two factors; first, the delayed prediction of separated flow and second, less computed blockage than actually occurred.

Cross-Stream Aerodynamic Data in Plane A

The flow field in Plane A corresponded to developing pipe flow. The results in Figure V.1 and Table V.1 verify the that boundary layer was fully turbulent. Total pressure contours for Plane A are presented in Figure VI.8. Normal velocity contours are displayed in Figure

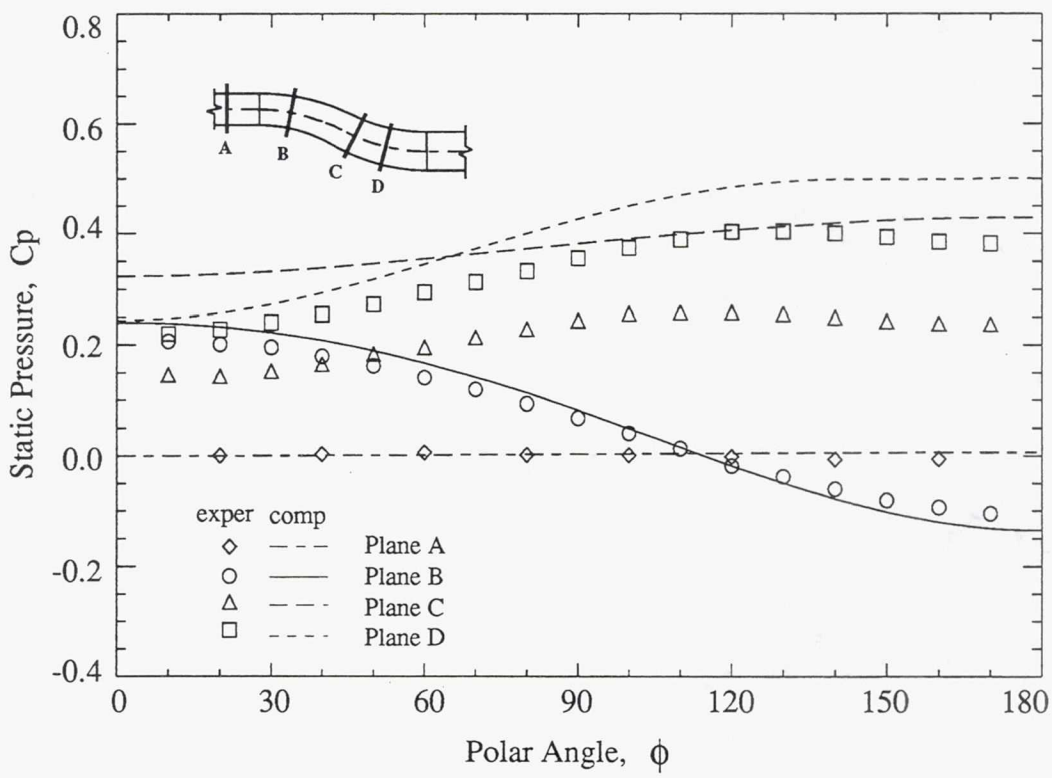

Figure VI.7 Circumferential distributions of surface static pressures in Planes A, B, C and D

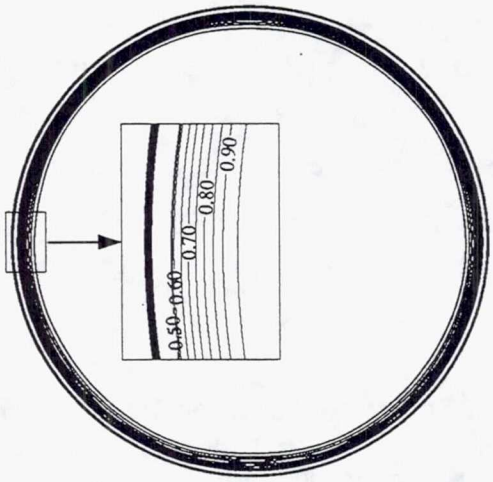

a) Experiment

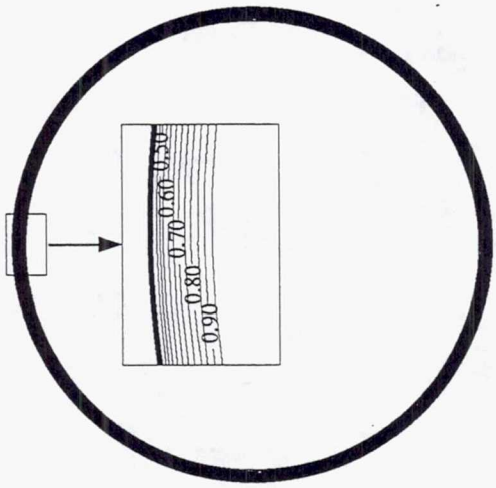

b) Computation

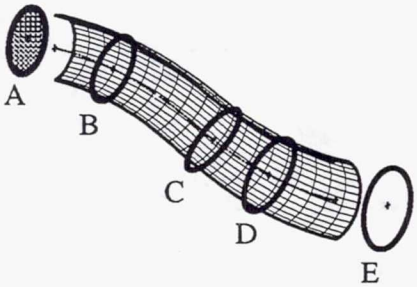

Plane A s / d = -0.50

Figure VI.8 Total pressure distributions in Plane A

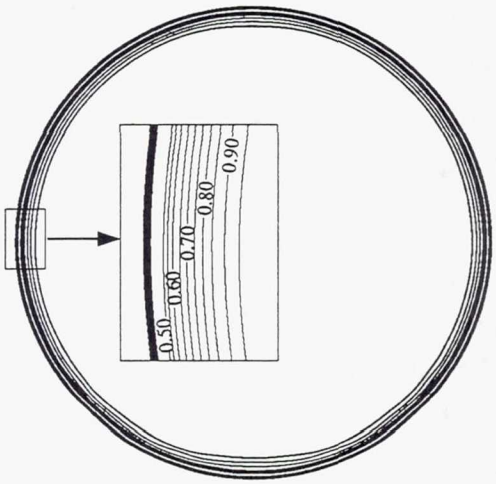

a) Experiment

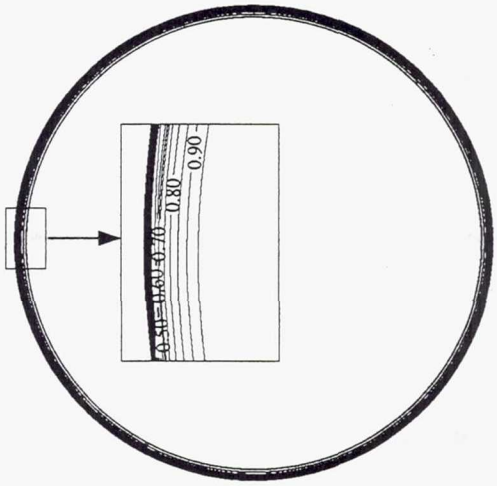

b) Computation

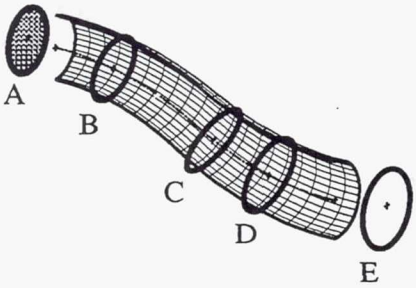

Plane A s / d = -0.50

Figure VI.9 Normal velocity distributions in Plane A

VI.9. Expanded views of these distributions near ϕ = 90° are included for comparison. Both the normal velocity and total pressure distributions (experimental and computational) show no circumferential variance. The measured and computed cross-stream static pressure distributions were nearly uniform, and are therefore not shown. This uniformity is consistent with the previously reported surface static pressures (Figures VI.6 and VI.7). The measured and computed cross flows were negligible, so transverse velocities are not presented. Vorticity was present only in planes normal to the streamwise direction.

The only discrepancy between the experimental and computational results is with the boundary layer thickness. This difference was explained in the Inlet Flow Conditions Chapter. The computational boundary layer was thinner than the experimental boundary layer. Since centerline and not bulk conditions were used to normalize aerodynamic data, this discrepancy does not affect the legitimacy of downstream comparisons.

Cross-Stream Aerodynamic Data in Plane B

Initially the S-duct deflected the incoming flow downward. This caused the flow field to deviate significantly from traditional developing pipe flow by Plane B. Cross-stream static pressure gradients developed as the flow progressed downstream. These gradients were a direct result of the core flow adjusting to duct geometry and the resulting streamline curvature. The measured and computed static pressure distributions in Plane B (Figure VI.10) indicate that the maximum static pressure existed at the top of the duct ($\phi = 0^o$) and the minimum was at the bottom of the duct ($\phi = 180^o$). These distributions are consistent with the surface static pressure data in Figures VI.6 and VI.7.

Total pressure contours are shown in Figure VI.11. Numerical and experimental results are nearly identical. There was little change in the total pressure distribution from Plane A to Plane B (Figures VI.8 and VI.11) except for a slight thickening of the boundary layer with downstream distance. The boundary layer thickness in Plane B did vary slightly with circumferential position. The boundary layer thickness was greatest at $\phi = 0^o$ and least at $\phi = 180^o$. This trend can be attributed to the streamwise pressure gradients upstream of Plane B which accelerated the flow near the bottom of the duct and decelerated the flow near the top of the duct.

The normal velocity distributions in Plane B (Figure VI.12) reflect the influence of streamline curvature. To reiterate, at the top of the duct, where the cross-stream pressure

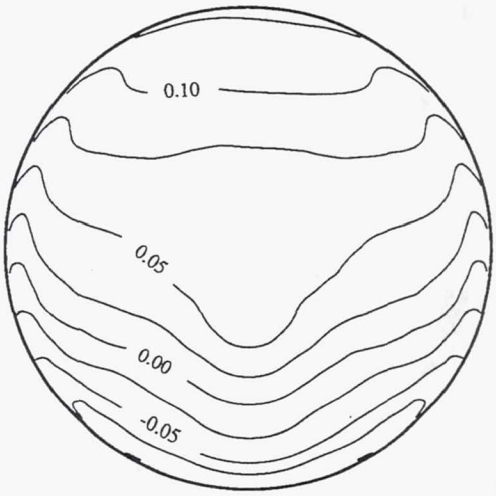

a) Experiment

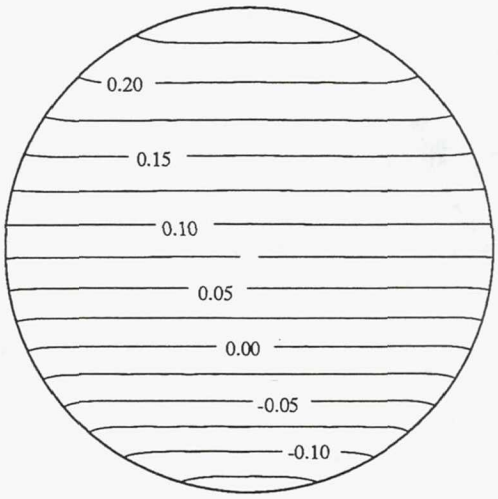

b) Computation

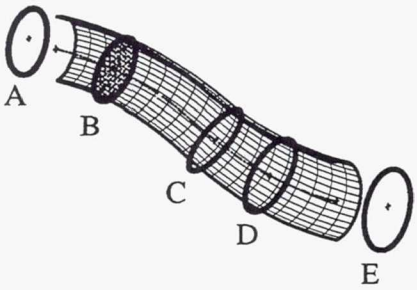

Plane B s / d = 0.96

Figure VI.10 Static pressure distributions in Plane B

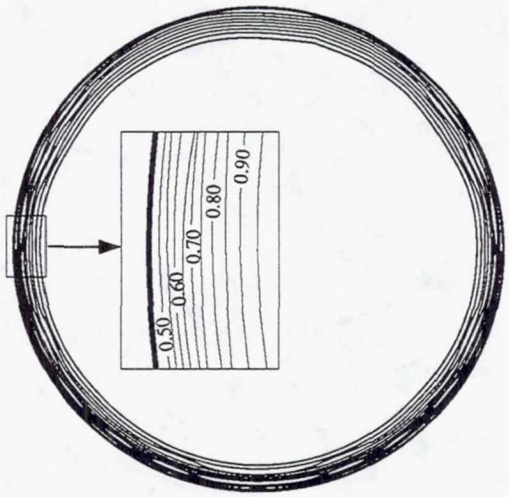

a) Experiment

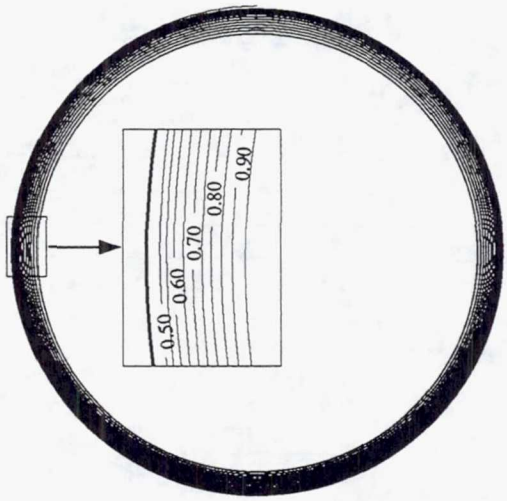

b) Computation

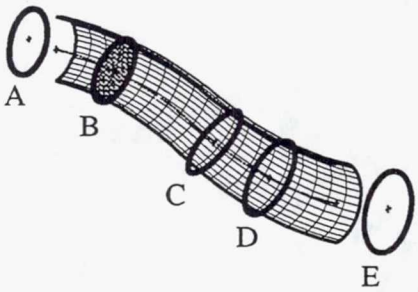

Plane B s / d = 0.96

Figure VI.11 Total pressure distributions in Plane B

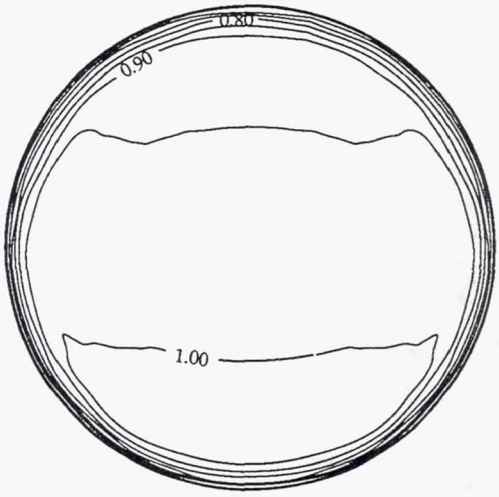

a) Experiment

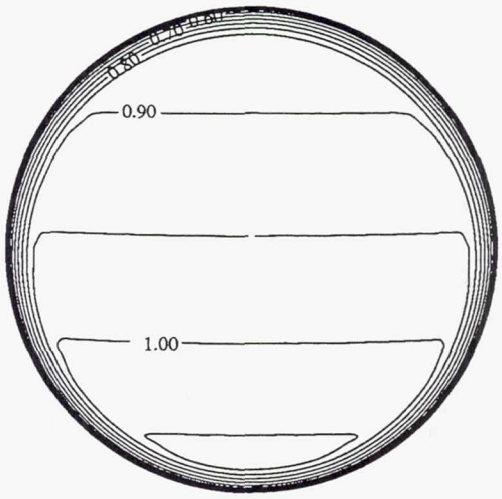

b) Computation

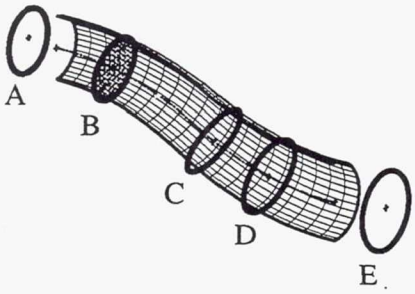

Plane B s / d = 0.96

Figure VI.12 Normal velocity distributions in Plane B

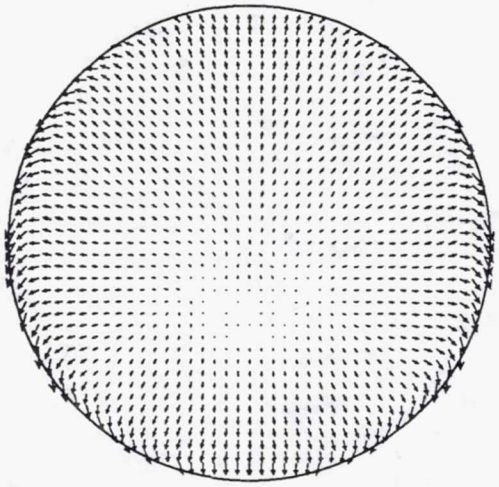

a) Experiment

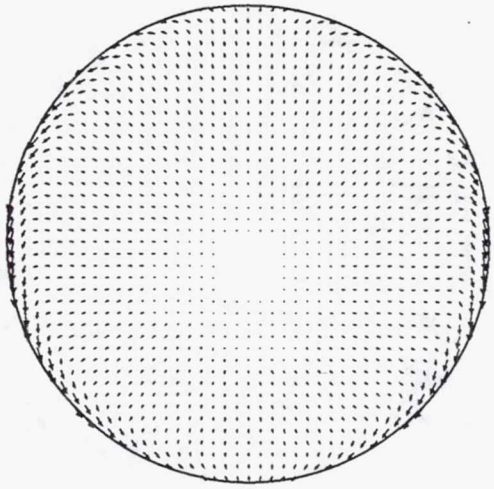

b) Computation

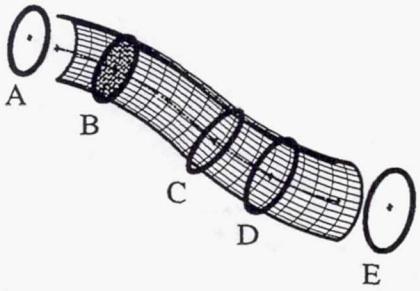

Plane B s / d = 0.96

Figure VI.13 Transverse velocity vectors in Plane B

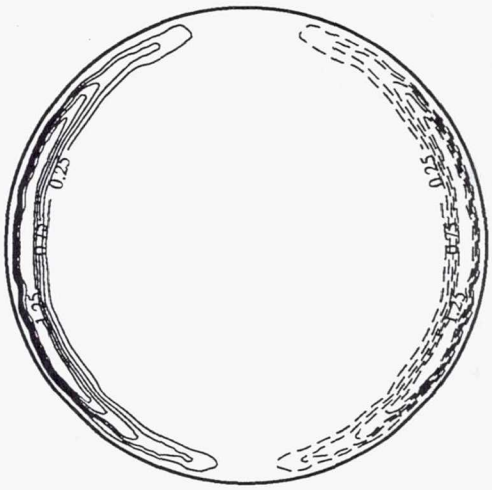

a) Experiment

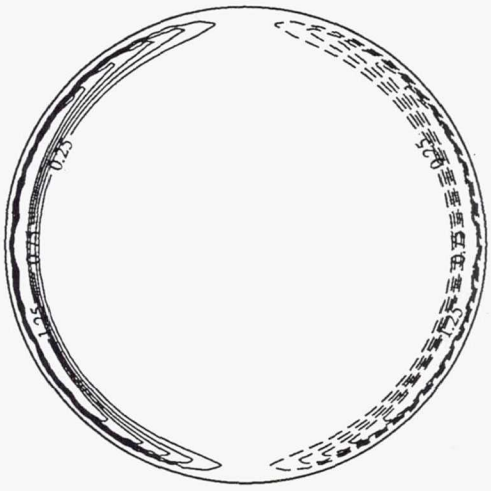

b) Computation

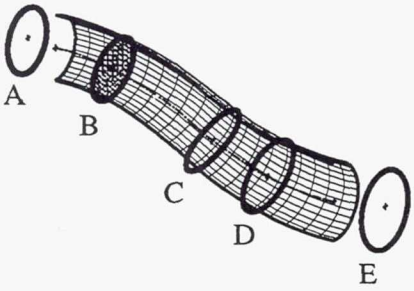

Plane B s / d = 0.96

Figure VI.14 Streamwise vorticity distributions in Plane B

was largest, an adverse streamwise pressure gradient decelerated the flow. At the bottom of the duct, where the minimum cross-stream pressure existed, a favorable streamwise pressure gradient accelerated the flow. This acceleration can be seen in Figure VI.12, where the local Mach number near the bottom of the duct exceeded the inlet Mach number.

Experimental and computational transverse velocity components in Figure VI.13 show that cross flows occurred only near the duct surface. These cross flows were caused by the pressure gradient turning the lower momentum boundary layer fluid toward the bottom of the duct. This was also detected in flow visualization, as seen in Figure VI.3. It is interesting to note that even though the pressure-driven cross flows near the duct wall were occurring in Plane B, a large region of low momentum fluid was not present near the bottom of the duct (Figure VI.11). This changed by Plane C.

The vorticity plots in Figure VI.14 confirm that transverse velocities in Plane B were confined to the wall boundary layer region only. Here the solid lines indicate positive vorticity, while dashed lines represent negative vorticity. The largest vorticity magnitude and hence the most amount of turning occurred at the sides of the duct. This was also illustrated in the transverse velocity plot (Figure VI.13). Excellent agreement in contour shapes and magnitudes of streamwise vorticity existed between test and computational data.

Cross-Stream Aerodynamic Data in Plane C

The location of Plane C (s/d = 2.97) was 0.35 diameters downstream of the middle of the S-duct. This plane was in the midst of the actual separated flow region. Differences between the computed and measured aerodynamic data arose since the computed separated flow region occurred further downstream (s/d = 3.14). The contours of static pressure, total pressure and normal velocity for Plane C are shown in Figures VI.15, VI.16 and VI.17. Transverse velocity components and streamwise vorticity are depicted in Figures VI.18 and VI.19.

Near the middle of the S-duct the static pressure distribution should become nominally flat as the centerline curve undergoes an inflection. In the second bend of the duct the orientation of the cross-stream static pressure distribution should reverse, so that the lowest static pressure is near the top of the duct and the highest static pressure is near the bottom. The static pressure data for Plane C in Figure VI.15 confirm this reversal. The measured static pressure data in Plane C also revealed a local region of nearly constant static pressure in the lower half of the duct. This trend substantiates a previous conclusion drawn from

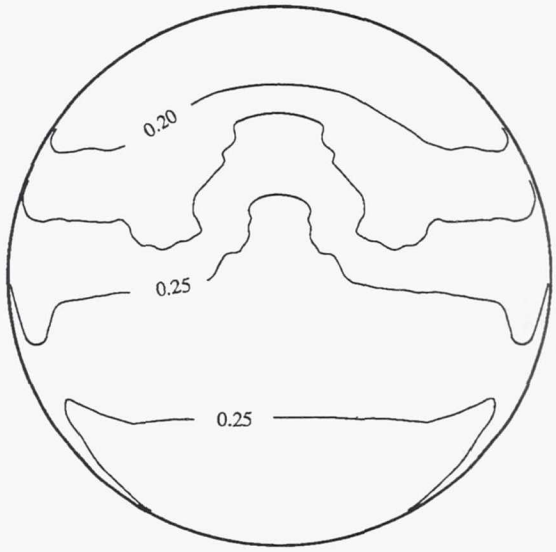

a) Experiment

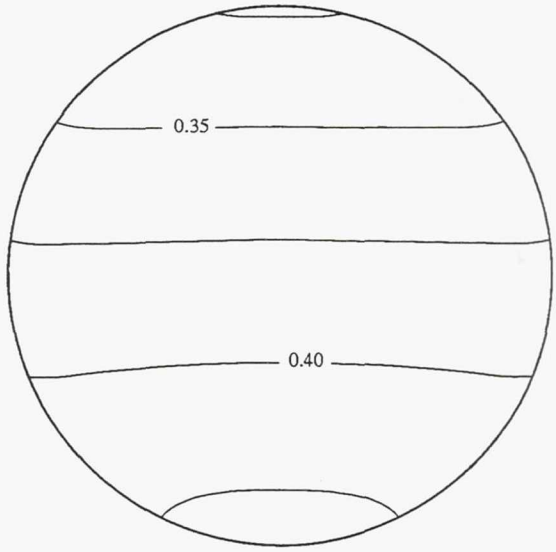

b) Computation

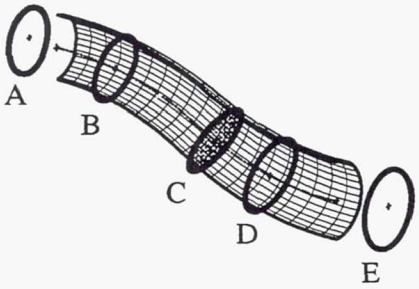

Plane C s / d = 2.97

Figure VI.15 Static pressure distributions in Plane C

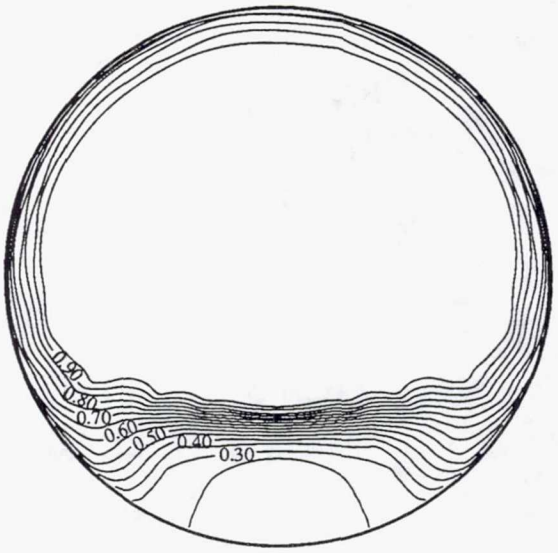

a) Experiment

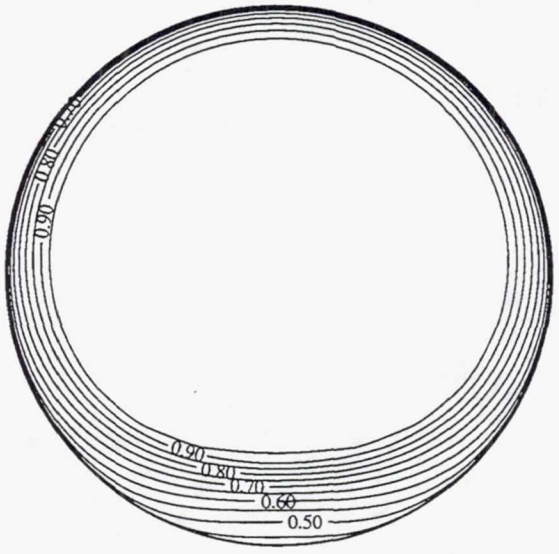

b) Computation

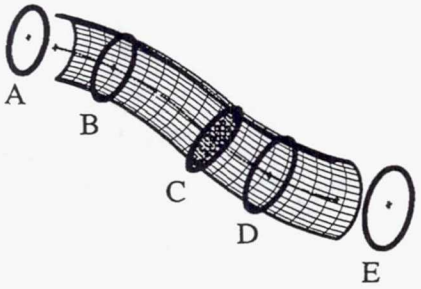

Plane C s / d = 2.97

Figure VI.16 Total pressure distributions in Plane C

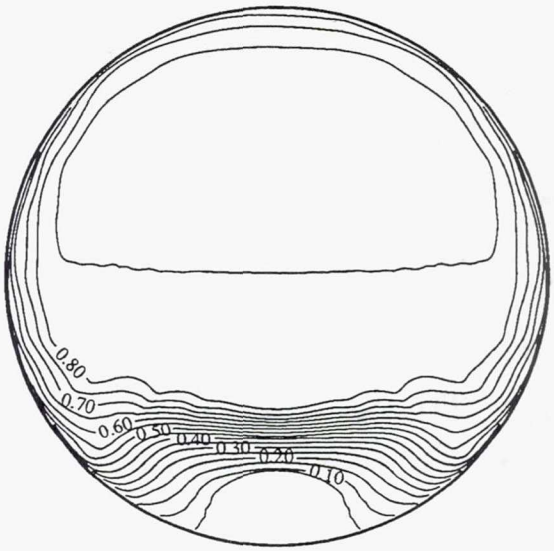

a) Experiment

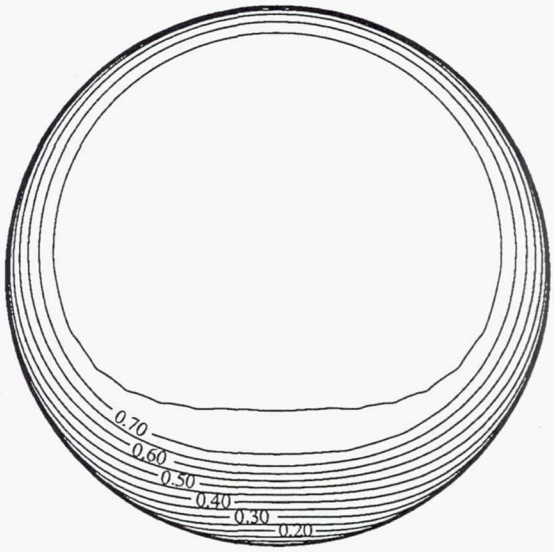

b) Computation

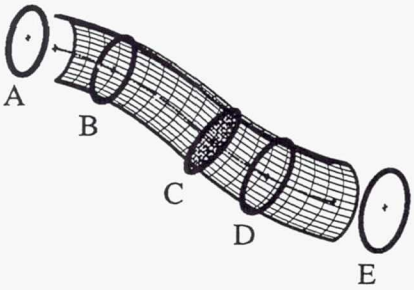

Plane C s / d = 2.97

Figure VI.17 Normal velocity distributions in Plane C

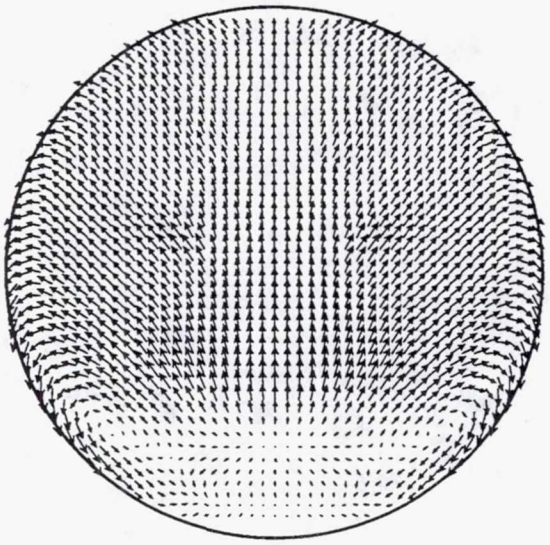

a) Experiment

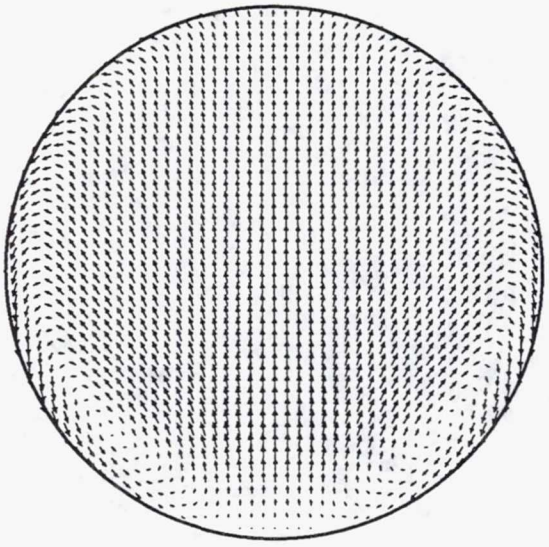

b) Computation

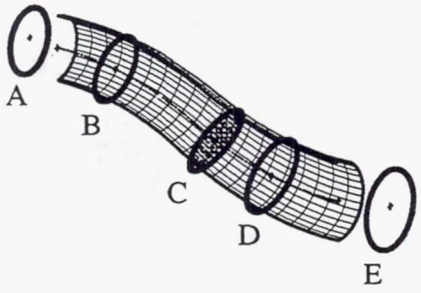

Plane C s / d = 2.97

Figure VI.18 Transverse velocity vectors in Plane C

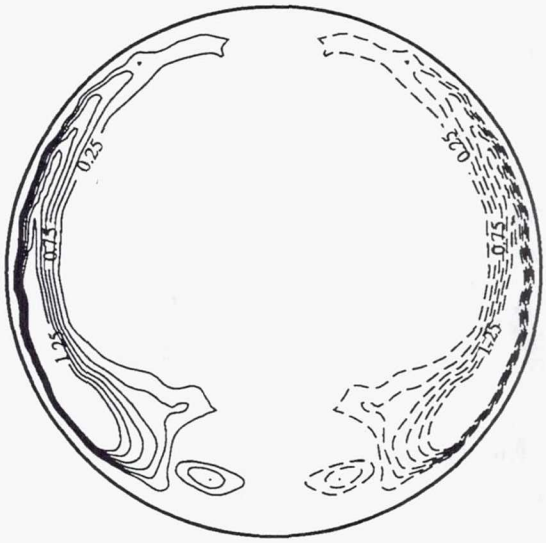

a) Experiment

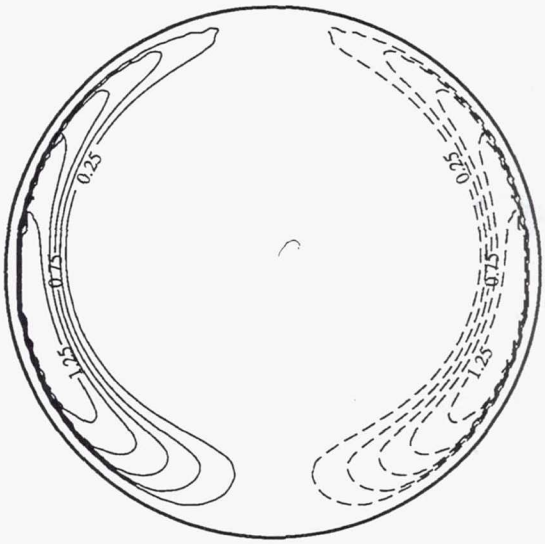

b) Computation

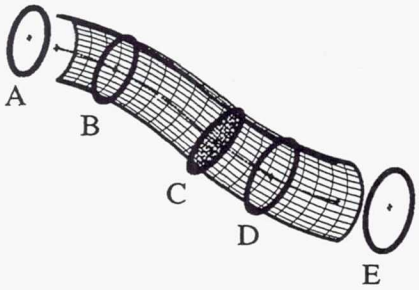

Plane C s / d = 2.97

Figure VI.19 Streamwise vorticity distributions in Plane C

the surface pressure data, namely, the existence of a region of only small changes in flow speed and/or direction. It is also consistent with the separated flow there. This same trend was not demonstrated by the computational results because of the delayed prediction of flow separation.

Strong, static-pressure-driven boundary layer cross flows existed near the lower duct surface in Plane C (Figure VI.18). These cross flows continually moved boundary layer fluid into the low velocity region. The cross flows suggest that two vortical structures were developing. These vortices were not present in Plane B. A significant amount of upward deflected flow at the centerline in Plane C is also shown in the measured data. This confirms the results obtained from the surface flow visualization on the temporary centerline splitter plane. This deflection was a direct consequence of two factors, blockage created by flow separation and cross flows driven by pressure gradients. Computationally, the smaller amount of upward centerline velocity deflection was a result of pressure-driven cross flows only.

Total pressures (Figure VI.16) and normal velocity components (Figure VI.17) show the accumulation of low momentum fluid in the bottom portion of the duct. The measured accumulation was caused by the reversed flow, the adverse streamwise pressure gradient and the convection of boundary layer fluid toward the lower surface. The same accumulation for the computational results was caused only by the adverse streamwise pressure gradient and the cross passage convection of boundary layer fluid.

The streamwise vorticity data, shown in Figure VI.14, again confirm the above mentioned trends. Here, the position of the largest vorticity magnitude moved slightly lower but was still at the sides of the duct. Overall agreement between test and computational data of the magnitudes of vorticity was surprisingly good, except near the bottom of the duct. This was where actual separation was present.

Cross-stream Aerodynamic Data in Plane D

The location of Plane D was at s/d = 4.01. This position was close to the actual reattachment point and in the middle of the computed separated flow region. Again, differences between the computed and measured aerodynamic data were expected and are present. For Plane D, the contours of static pressure, total pressure and normal velocity are shown in Figures VI.20, VI.21 and VI.22. Transverse velocity components are depicted in Figure VI.23. Streamwise vorticity distributions are plotted in Figure VI.24.

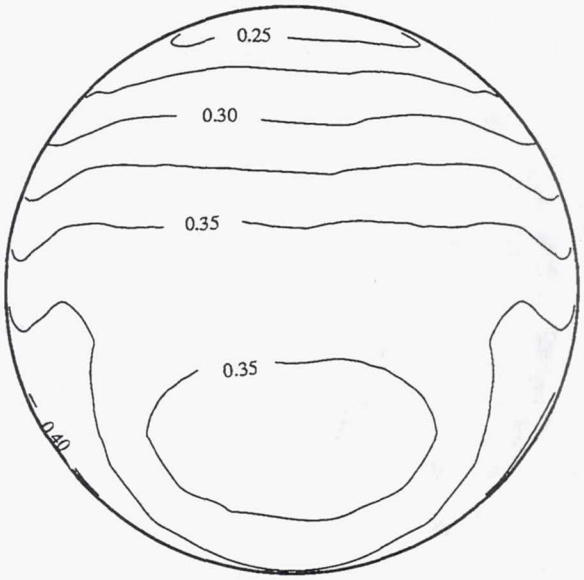

a) Experiment

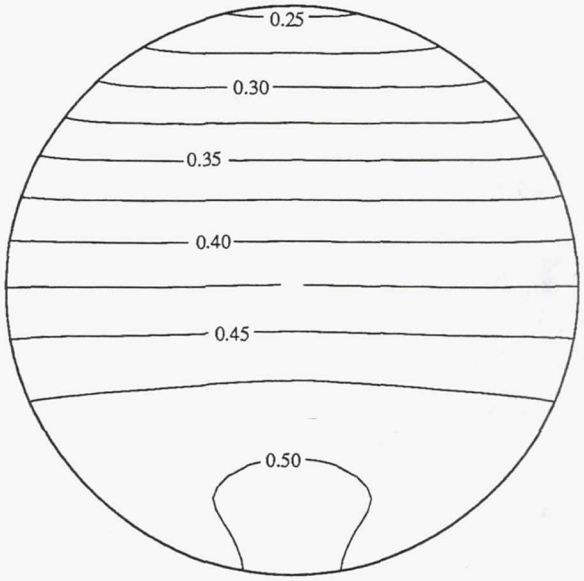

b) Computation

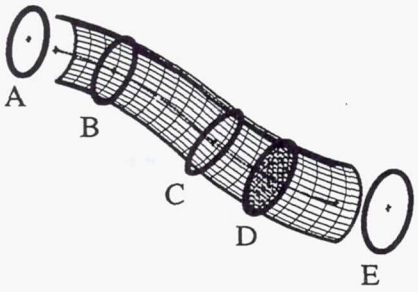

Plane D s / d = 4.01

Figure VI.20 Static pressure distributions in Plane D

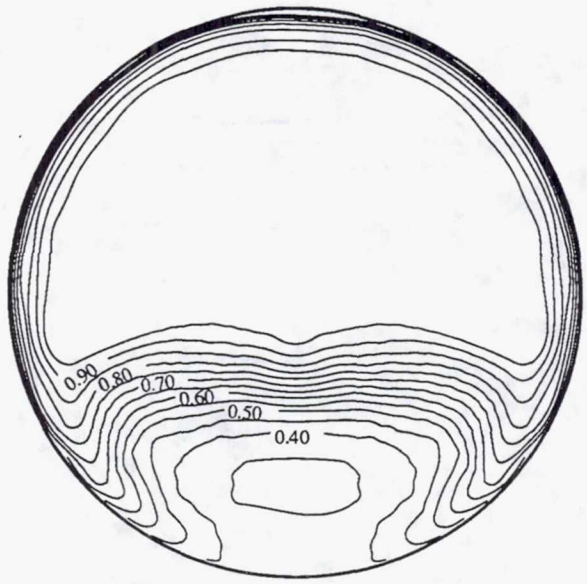

a) Experiment

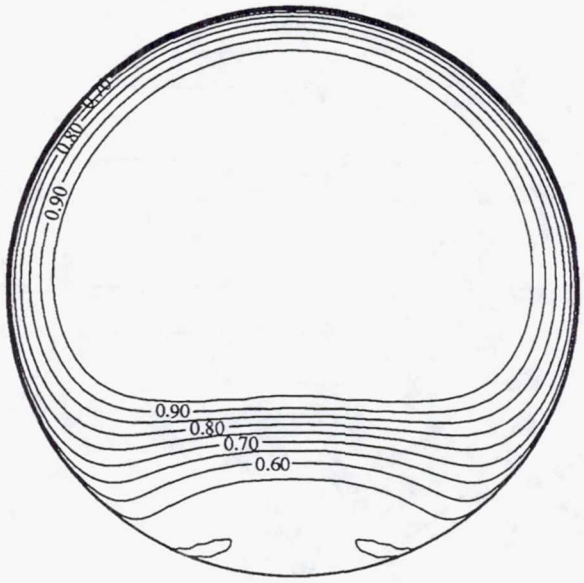

b) Computation

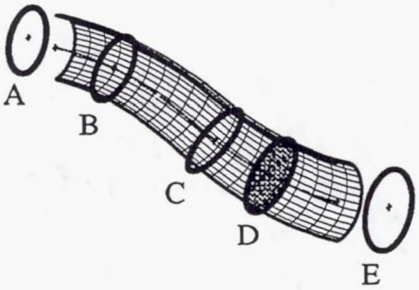

Plane D s / d = 4.01

Figure VI.21 Total pressure distributions in Plane D

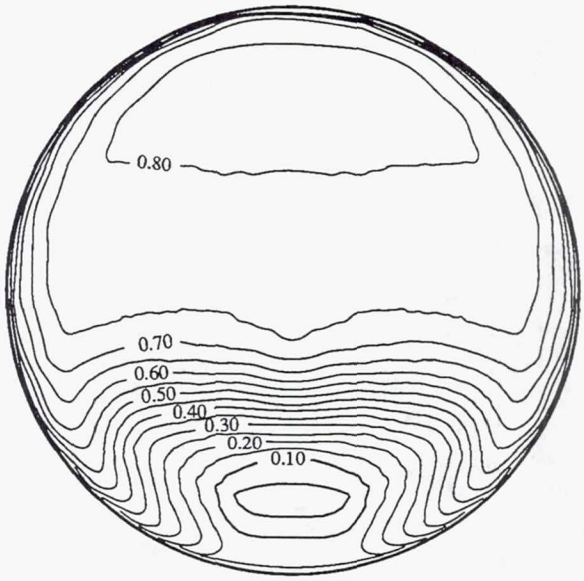

a) Experiment

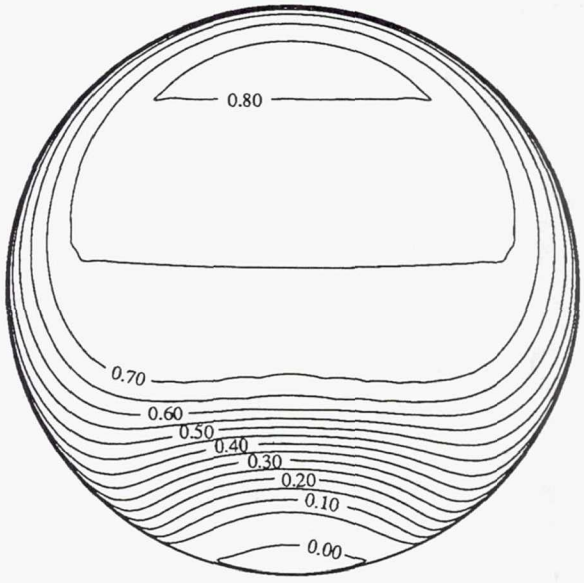

b) Computation

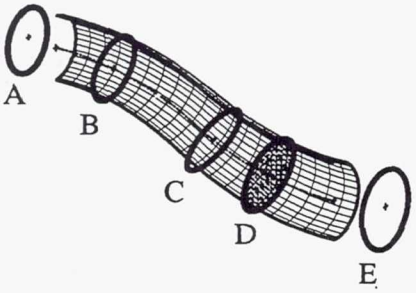

Plane D s / d = 4.01

Figure VI.22 Normal velocity distributions in Plane D

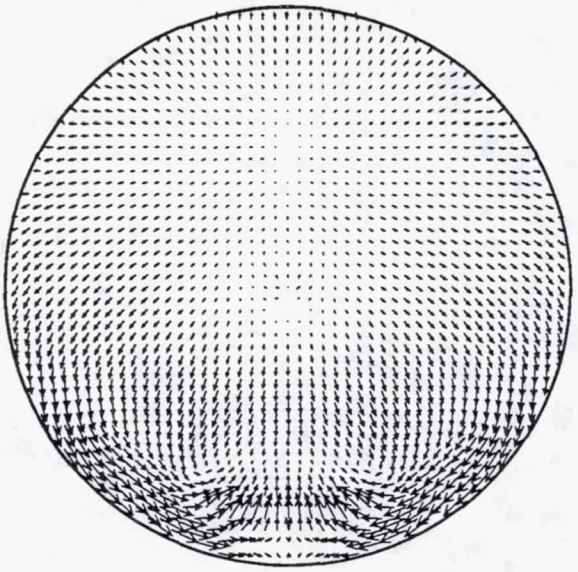

a) Experiment

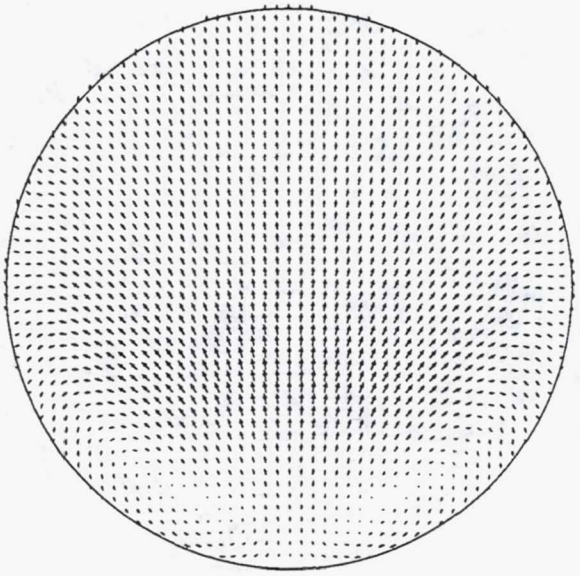

b) Computation

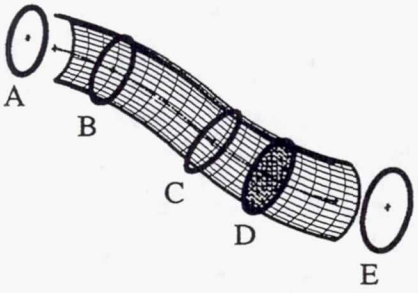

Plane D s / d = 4.01

Figure VI.23 Transverse velocity vectors in Plane D

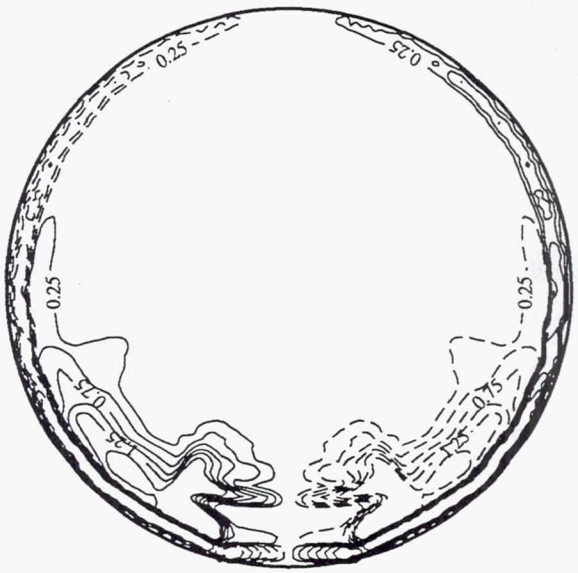

a) Experiment

b) Computation

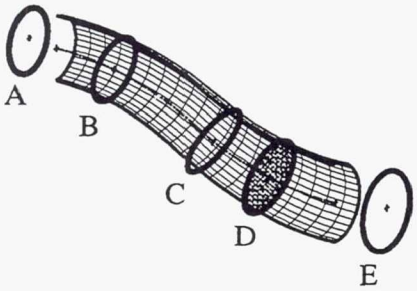

Plane D s / d = 4.01

Figure VI.24 Streamwise vorticity distributions in Plane D

The static pressure data in Plane D (Figure VI.20) are similar to static pressure data in Plane C. The measured distribution still indicated a substantial region of nearly constant static pressure in the lower half of the duct ($Cp \approx 0.35$). This region was also present in Plane C. The computational results suggest a similar region, although at a much higher pressure value ($Cp \approx 0.475$).

Total pressures (Figure VI.21) and normal velocity components (Figure VI.22) suggest further growth of the low total pressure/low velocity region in the bottom half of the duct. Measurements indicate that enough low momentum fluid was carried away from the duct wall to form a region of near zero velocity far from the surface. Computationally this region was still evolving.

Strong pressure-driven cross flows still existed near the lower duct surface in Plane D (Figure VI.23). These cross flows continually drove boundary layer fluid toward the low velocity region. A strong vortical structure developed. For the experiment, the core flow returned to the nominal streamwise direction by the time it reached Plane D, which is contrary to the splitter plate streakline patterns. This inconsistency was caused by the pressure gradients which drove the boundary layer fluid on the splitter plate toward the top of the duct, as previously explained.

Streamwise vorticity data (Figure VI.24) revealed that the boundary layer fluid at the top of the duct began to turn upward. This was slightly noticeable in the transverse velocity plots (Figure VI.23). This reversal in cross-stream flow direction was caused by the change in static pressure distribution from Plane B to Plane D. It is interesting to note that even though Plane D is well into the second bend, no large vortical structure existed at the top of the duct in Plane D.

Cross-stream Aerodynamic Data in Plane E

By Plane E the free stream flow returned nominally to the x-direction. Cross-stream static pressure gradients were nearly eliminated and are therefore not illustrated. The total pressure and normal velocity distributions are represented by contours in Figures VI.25 and VI.26. Transverse velocity components and streamwise vorticity for Plane E are depicted in Figures VI.27 and VI.28.

Even though cross-stream static pressure gradients did not exist in Plane E, upstream of Plane E, pressure gradients were strong enough to fully reverse the direction of the boundary

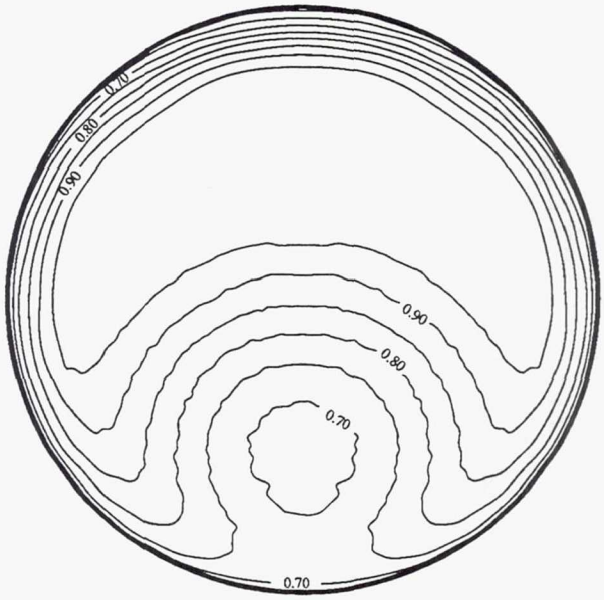

a) Experiment

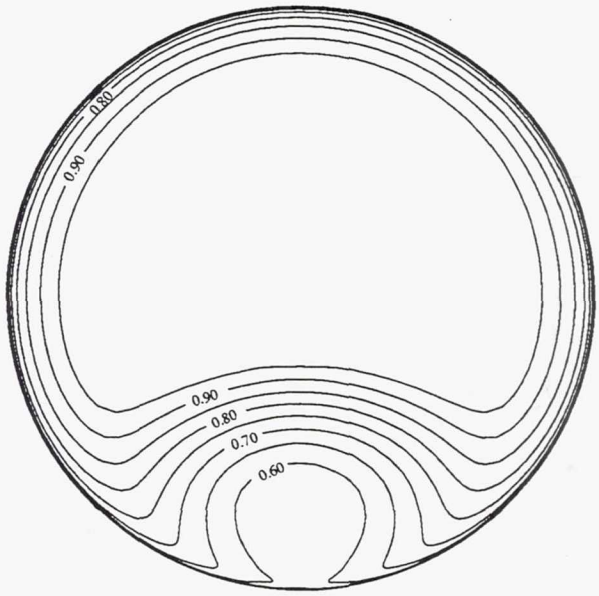

b) Computation

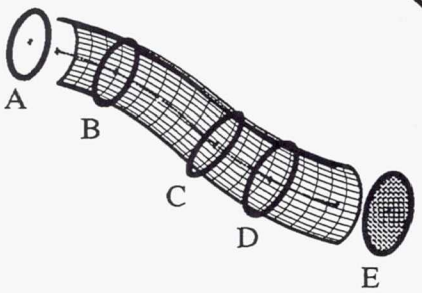

Plane E s / d = 5.73

Figure VI.25 Total pressure distributions in Plane E

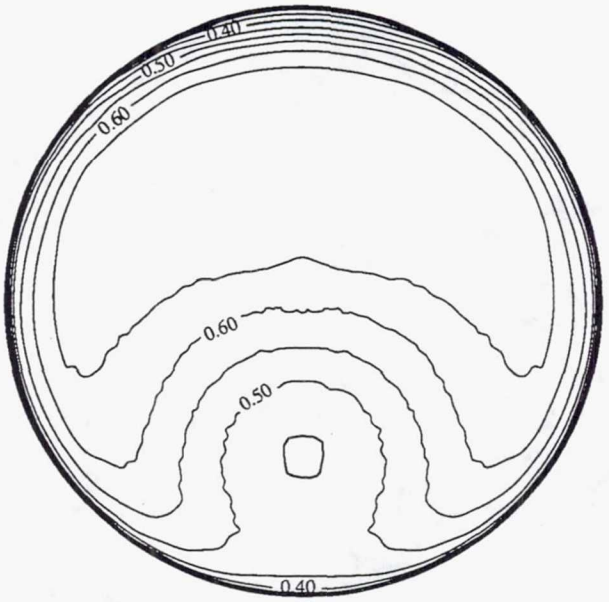

a) Experiment

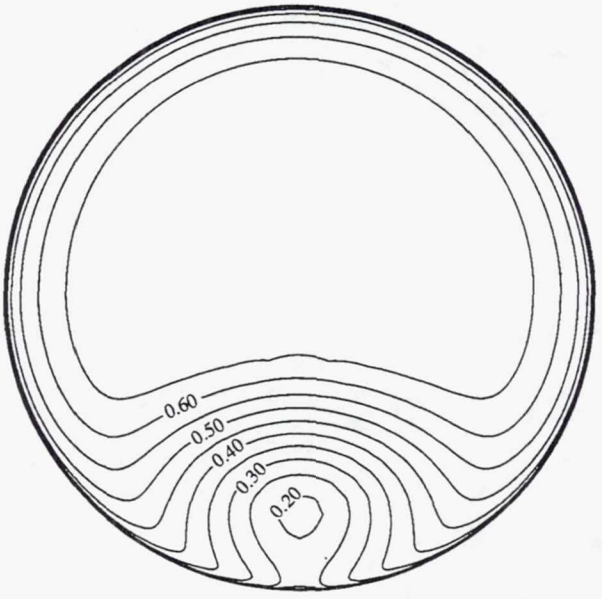

b) Computation

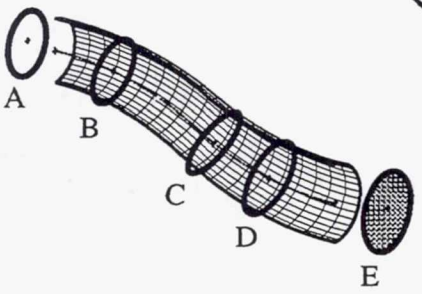

Plane E s / d = 5.73

Figure VI.26 Normal velocity distributions in Plane E

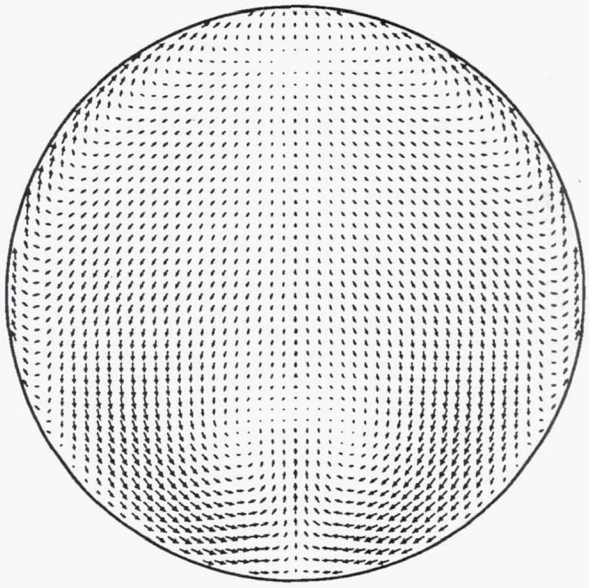

a) Experiment

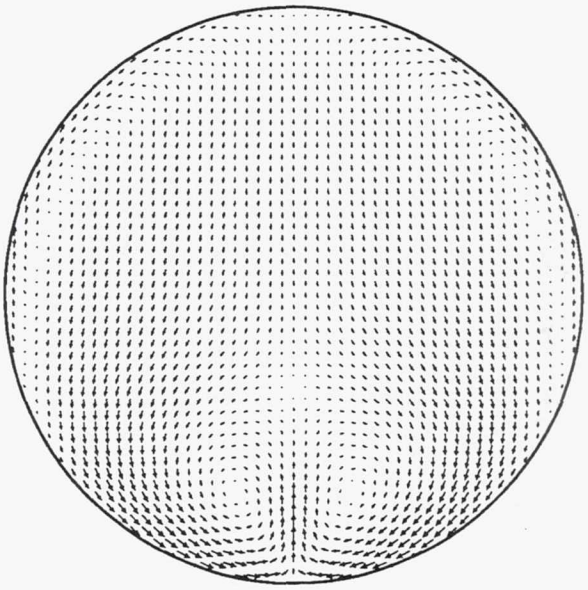

b) Computation

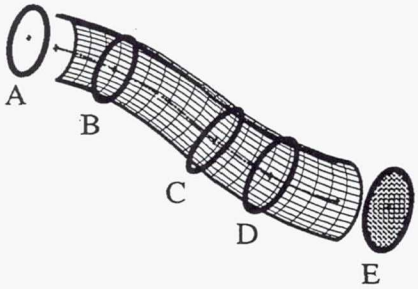

Plane E s / d = 5.73

Figure VI.27 Transverse velocity vectors in Plane E

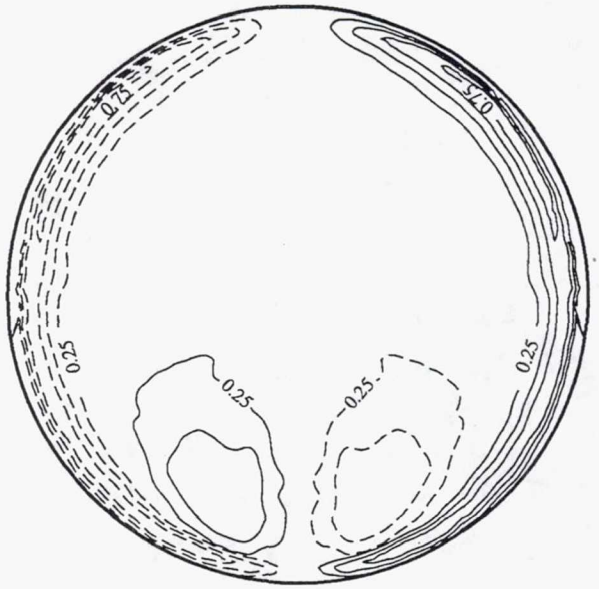

a) Experiment

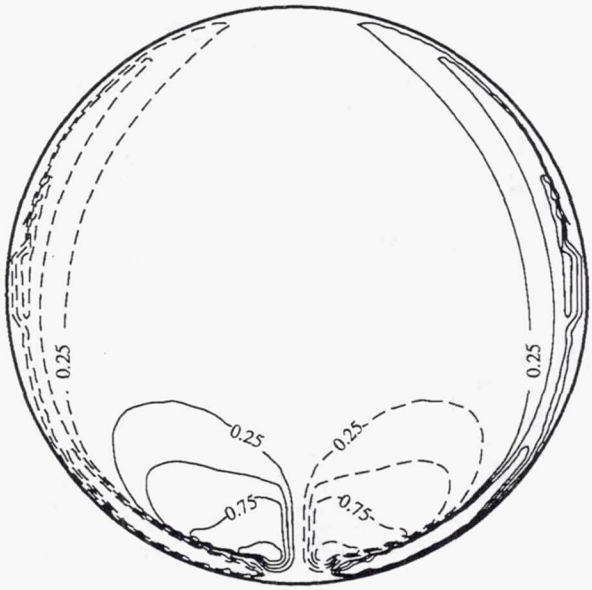

b) Computation

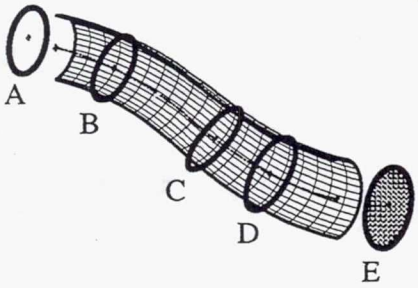

Plane E s / d = 5.73

Figure VI.28 Streamwise vorticity distributions in Plane E

layer fluid flow on the upper surface of the duct, as seen in Figures VI.27 andVI.28 for both measured and computed results. This was also detected with flow visualization. This phenomenon had just begun in Plane D. A pair of counter-rotating vortices, located in the lower half of the duct, evolved. These vortices continually convected the low momentum fluid of the boundary layer toward the center of the duct. The positions of the computed counter-rotating vortices were not in the same location as the measured vortices. This discrepancy between computed and experimental results was noted also by Harloff *et al.* [19]. Vorticity values (Figure VI.28) also indicated that the measured vortical structure was much weaker than the computed vortical structure.

Low momentum fluid convection by the vortices degraded both the uniformity and magnitude of the exit total pressure distribution. The measured region of low momentum fluid in Plane E (Figure VI.25 and VI.26) extended above the duct center line. This trend had been observed before by previous investigators [5,9]. The inability of numerical algorithms to capture this flow phenomenon (as in the P-PNS results) has also been documented by several researchers [14,18,19].

CHAPTER VII

FURTHER INSIGHTS INTO SEPARATED FLOW

Flow separation is usually related to the occurrence of reversed flow near a solid surface. Often, reversed flow simply refers to any flow whose direction is opposite to the projection of the free stream direction onto the surface. Therefore, in a two-dimensional steady flow, the phenomenon of flow separation may be clearly defined. Unfortunately, two-dimensional flow is very rare. For three-dimensional flows, the specification of separation in terms of reversed flow may be inadequate and/or inappropriate. This chapter attempts to describe and classify the region of separated flow within the S-duct by using well defined terminology. This terminology has its origin in notions based on topological structures and streamsurface bifurcation.

Legendre proposed that a pattern of streamlines near a surface may be considered as trajectories having properties consistent with those of a vector field [34]. A principle property of a vector field states that through any nonsingular point there must pass one and only one trajectory. Therefore if streamline trajectories near a surface constitute a vector field, elementary singular points of this field can be categorized mathematically. Departing from the notion of nearwall streamlines, whose velocities vanish to zero at the wall, Lighthill [35] connected skin-friction lines on a body surface to this continuous vector field. In either

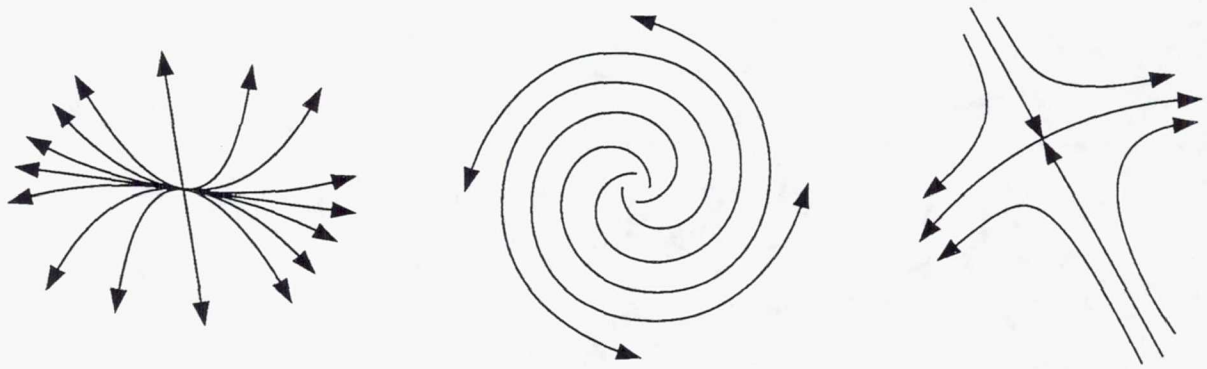

Nodal point Spiral node Saddle point

Figure VII.1 Illustrations of elementary singular points

case, it is common to assume that oil-streakline patterns which develop on a solid surface during an experiment closely represent both skin-friction lines and nearwall streamlines.

Singular points in a pattern of skin-friction lines or oil-surface streaklines occur at points on the surface where skin-friction becomes identically zero. Two types of singularities can occur: nodes and saddle points. Nodes are further classified as nodal points or foci. For this thesis, foci are simply termed spiral nodes.

A point common to an infinite number of skin friction lines is termed a nodal point. All but one of these skin-friction lines are tangent to a specific single line emanating from the singular point. An exception to this case is when every skin-friction line leaving or entering a singular point has a distinct tangent. This type of nodal point can be produced by flow over a thin axisymmetric cylindrical body. A spiral node has no common tangent line and therefore differs from a nodal point. In a spiral node, an infinite number of skin-friction lines spiral around the singular point. If the skin-friction lines spiral away from the point it is called a spiral node of attachment. If the skin-friction lines spiral into the point it is called a spiral node of separation. A saddle point differs from any node in that only two distinct skin-friction lines pass directly through the singular point. All other skin-friction lines around a saddle point miss the singular point. In this respect, a saddle point commonly acts as barrier between two adjacent sets of skin-friction lines. Representative illustrations of these singular points are presented in Figure VII.1.

With the notions of streamsurface bifurcation theory, Hornung and Perry [36] have added to the vocabulary of well defined terms for the description of three-dimensional steady separated flows. Many steady three-dimensional flows can be described by streamsurfaces. Often in flows fields there exist special streamsurfaces which appear to bifurcate (split apart or

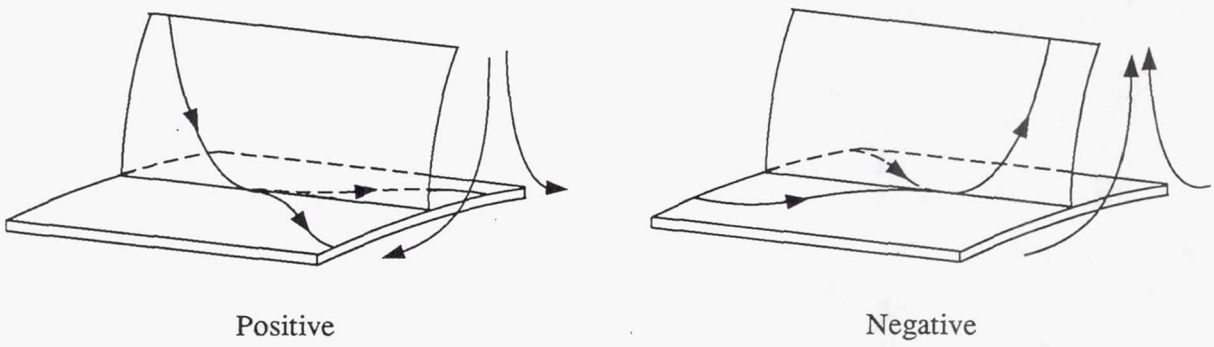

Figure VII.2 Streamsurface bifurcations on a solid wall

combine together). There are two ways a streamsurface can bifurcate. A positive bifurcation refers to a stagnation streamsurface which divides along a stagnation line. For a positive bifurcation, a single streamline within the stagnation streamsurface appears to bifurcate into two different streamlines at the positive bifurcation line. Positive bifurcations usually are associated with downwashing counter-rotating vortices. A negative bifurcation refers to a streamsurface which emerges from a negative bifurcation line. In a negative bifurcation, two different streamlines near a flow boundary combine to form a single streamline within the streamsurface. Negative bifurcations usually are connected to uplifting counter-rotating vortices. Positive and negative bifurcations are illustrated in Figure VII.2.

From the few notions of streamsurface bifurcation and topological singularities introduced above, the region of separated flow within the S-duct can now be adequately described. To begin, imagine cutting the surface of the test S-duct along the top of the vertical centerline plane ($\phi = 0°$). Now imagine unfolding the duct onto a horizontal plane. The oil-streakline patterns developed during the S-duct surface flow visualization tests (Figures VI.2–VI.5) then would closely resemble Figure VII.3. Here the flow is from left to right and both symmetric halves of the duct surface are shown. These original streakline patterns can be mapped onto a "skeleton" drawing, which illustrates the important topological singular points

Figure VII.3 Unwrapped S-duct surface streakline patterns

and bifurcation lines. The skeleton drawing related to the S-duct surface streakline patterns is shown in Figure VII.4. Two saddle points, two spiral nodes, two positive bifurcation lines and four negative bifurcation lines are identified in the simplified skeleton drawing.

The streakline patterns indicate that two negative bifurcation lines emanated from the upstream saddle point. These negative bifurcation lines ran in opposite cross-stream directions and were symmetric about the centerline. Each of these bifurcation lines were drawn into two symmetrically arranged spiral nodes of separation. A third negative bifurcation line developed from the downstream saddle point. A fourth negative bifurcation line was located at the top of the duct (along the line which was cut to unfold the S-duct). A pair of positive bifurcation lines flanked the two spiral nodes on the downstream side of the pattern.

This pattern of streaklines has been previously named an "owl face" separation [37]. Streakline patterns similar to this one have been observed in regions where the flow is under the strong influence of two uplifting vortices. These strong uplifting vortices were shown to exist in the S-duct. Owl face separations are further classified as first or second kinds. Owl face separations of the second kind have another spiral node within the flow field located on the symmetric plane . An owl face of the first kind is void of this spiral node

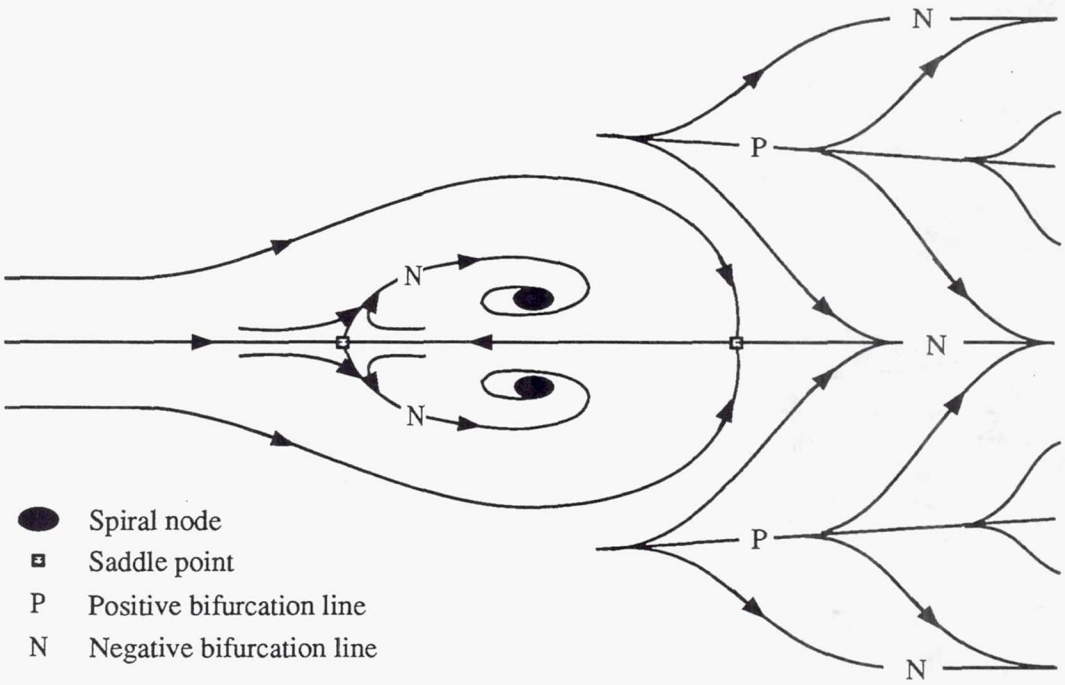

Figure VII.4 Skeleton schematic of the surface streakline patterns

on the symmetric plane. After observing to the flow visualization patterns developed on the surface of the temporary splitter plate, the separation region can now be further classified as an "owl face of the first kind", since no visible spiral node was present on the centerline splitter plate. A perspective drawing representing an owl face separation of the first kind is shown in Figure VII.5. The two tubes in Figure VII.5 correspond to the stream surfaces coiled around the two vortices. This drawing corresponds well to the S-duct experimental transverse velocity measurements and surface flow visualization observations.

In Figure VII.4 a single streakline has been drawn between the two saddle points without passing through a node on the way. Some researchers [34] consider this to be an impossible situation because it is unstable. These researchers proclaim that slight variations in any flow field conditions would alter this topological structure. However, Perry and Hornung [37] ingeniously used these slight variations in flow field conditions to justify why this topological structure can exist. They explain that the pattern drawn in Figure VII.4 is extremely special, and the slightest asymmetry in the flow would alter the streakline pattern to the one shown in Figure VII.6. Here, no trajectories pass directly between two saddles. The slightest unsteadiness might even cause the pattern to oscillate between that of Figure VII.6 and its mirror image. Perry and Hornung further point out, that from a practical viewpoint the

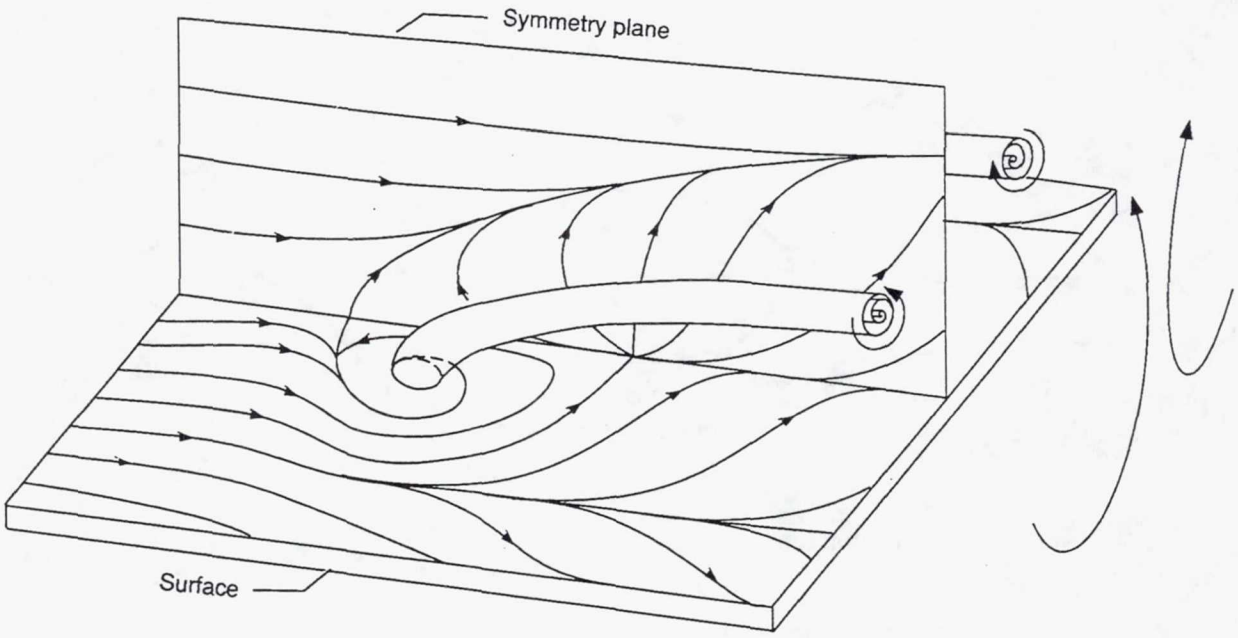

Figure VII.5 Perspective view of an owl face separation of the first kind

patterns in Figures VII.4 and VII.6 are not experimentally distinguishable since the streakline emanating from a saddle point is almost impossible to accurately identify.

Upon describing the separated flow region within the S-duct, the question arises, "What portion of the flow field is truly part of the separated flow?" and/or, "Is separated flow even a proper term to use when dealing with three-dimensional flow ?". These questions are not readily answered. It is easy to see though that referring to separated flow strictly as reverse flow is incorrect, for within the S-duct only a small region between the two spiral nodes involved reversed flow. However, most aerodynamicists would agree that the flow in the area surrounding the spiral nodes and even perhaps the flow near the negative bifurcation lines constitutes separated flow. Many researchers deem that a necessary condition for the occurrence of flow separation on a continuous surface is the convergence of oil-streakline patterns onto a particular streakline. This is perhaps the best current indicator of three-dimensional separated flow, and it is supported by the present S-duct aerodynamic and surface flow visualization data.

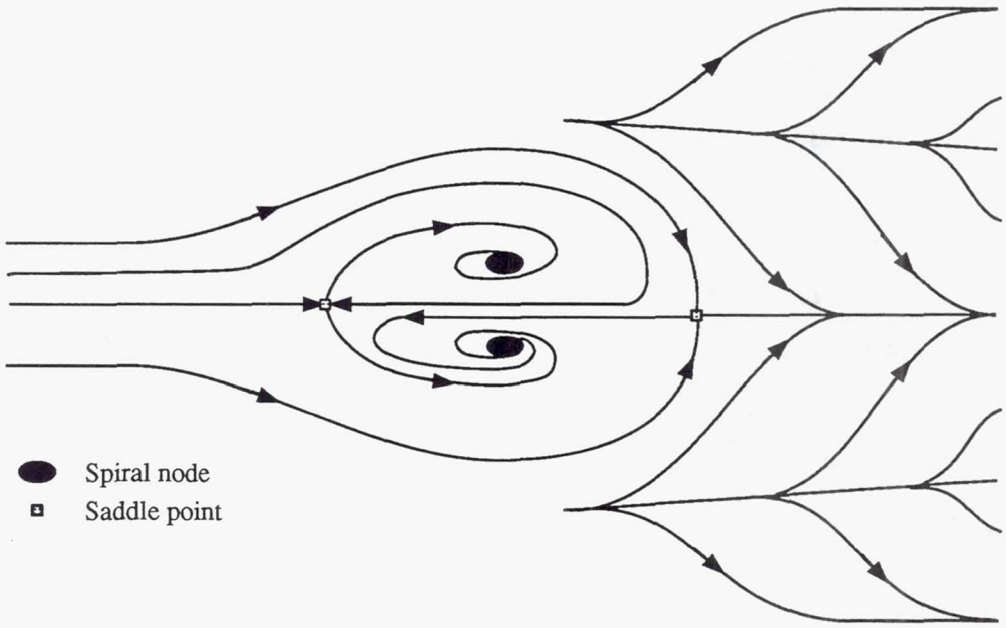

Figure VII.6 Skeleton schematic illustrating asymmetric surface streakline patterns

CHAPTER VIII

CONCLUSIONS

Compressible, subsonic flow through a diffusing S-duct was experimentally and computationally investigated. Benchmark aerodynamic measurements of the three dimensional velocity field and total pressures and static pressures were obtained in five cross-sectional planes. Surface static pressure and flow visualization data were also acquired. The S-duct flow field was computed using a subsonic parabolized Navier-Stokes code. Experimental and numerical results were compared.

The experimental measurements show that a large three-dimensional region of separated flow occurred within the duct. A large portion of the duct cross-section was blocked by this separated flow region. This blockage forced the core velocity to increase while passing over the separated flow region. The increase in core velocity led to larger shear stress levels and therefore larger total pressure losses within the S-duct. The duct curvature induced strong pressure driven secondary flows, which evolved into two counter-rotating vortices. These vortices convected low-momentum boundary layer fluid into the lower portion of the duct and from there out toward the center of the duct, degrading both the uniformity and magnitude of the total pressure distribution. At the duct exit, a large region of low momentum fluid filled the lower half of the duct and extended above the centerline.

The computational results are generally in agreement with the experimental measurements. Strong cross flows, total pressure nonuniformity and a separated flow region were all predicted. However, the separation region was calculated to occur further downstream than actually observed. The calculated cross flows did not convect as much low momentum fluid to the center of the duct as the actual cross flows did. These discrepancies, common to the use of both full and parabolized Navier-Stokes algorithms to simulate duct flows, are linked mainly to turbulence modeling and were not necessarily the fault of the simplified governing equations used in parabolized codes. In fact, parabolized codes are better suited for preliminary design purposes because of inherent reduced computational effort.

These experimental and computational analyses of the flow field could ultimately be beneficial to S-duct designers. The numerical results demonstrate how approximate flow field trends can be predicted using a simplified parabolized model of the flow. The three- and five-hole probe calibration and data reduction procedures could enable an experimentalist

to obtain quick and accurate measurement data in other ducts. The collected experimental data are suitable for the validation of computational codes. Data for S-ducts having improved performance could be compared to these baseline data.

CHAPTER IX

RECOMMENDATIONS FOR FURTHER RESEARCH

Although the material reported in the thesis is complete, additional experimental and computational analyses of the flow through a diffusing S-duct would be beneficial to inlet designers. Further baseline experimental studies using hot wires to obtain Reynolds stresses and an estimate of velocity fluctuations are still needed. Hot film gages, located on the surface of the duct, may be able to better trace the separation footprint, including some unsteady aspects of this complex flow phenomenon. In addition, an ethylene trace gas study would help confirm fluid particle pathline conclusions.

Investigations involving active or passive flow management devices, which control the extent and effects of flow separation, would be very insightful. A parametric study determining the performance benefits acquired when embedded counter-rotating vortex generators are installed in the duct is currently under progress. A study of the effects of embedded co-rotating vortex generators or boundary layer suction on the flow field to manage separation would also be useful.

The advancement of military aircraft continually make the designer expand current inlet flow technology. Advances in canard control-surfaces bring to light the need for experimental data for S-duct flows with asymmetric inlet profiles. Simple vortex ingestion experiments could produce valuable insights to this design problem. A second type of S-duct, having square-to-circular transitioning cross sections, is often used in military aircraft. Studies, similar to the one described herein need to be done on this type of S-duct.

The conclusions of this thesis indicate that much effort must be channeled toward the development of an accurate anisotropic turbulence model in order to accurately predict complicated flow fields, as in an S-duct. Unfortunately, this is not an easy task. Therefore, designers and researchers must use the tools available, keeping in mind the limitations and strengths involved.

CHAPTER X

POSTSCRIPT

The aerodynamic benchmark data collected in this study may be used for the validation of computational fluid dynamic codes. Further information concerning this study may be obtained from the authors. The data is available on diskette, tape or through the internet. Please send internet mail to fsbud@lerc.nasa.gov or fsbud@iastate.edu .

BIBLIOGRAPHY

[1] Bauermeister, W. K., Roseburg, C. M., and Ip, H. W., "727 Airplane Engine Inlet Development," AIAA Paper 68-595, 1968.

[2] "The Boeing 727-200 Inlet : Phase II Preliminary Report," Boeing Commercial Airplane Company, Jan. 1974.

[3] Little, B. H. and Trimboli, W. S., "An Experimental Investigation of S-Duct Diffusers for High-Speed Prop-Fans," AIAA Paper 82-1123, 1982.

[4] Rowe, M., "Measurements and Computations of Flow in a Pipe Bend," *Journal of Fluid Mechanics*, Vol. 43, 1970, pp. 771–783.

[5] Bansod, P. and Bradshaw, P., "The Flow in S-shaped Ducts," *Aeronautical Quarterly*, Vol. 23, May 1972, pp. 131–140.

[6] Sullivan, J. P., Murthy, S. N. B., Lan, T. H., Davis, R., and Hong, S., "S-Shaped Duct Flows," Purdue University School of Aeronautics and Astronautics Report S-ONR-TSR-80-2, Oct. 1980.

[7] Guo, R. W. and Seddon, J., "The Investigations of Swirl in an S-duct," *Aeronautical Quarterly*, Vol. 33, May 1982, pp. 25–58.

[8] Taylor, A. M. K. P., Whitelaw, J. H., and Yianneskis, M., "Developing Flow in S-Shaped Ducts II - Circular Cross-Section Duct," Imperial College of Science and Technology NASA Contractor Report 3759, Feb. 1984.

[9] Vakili, A. D., Wu, J. M., Liver, P., and Bhat, M. K., "Experimental Investigation of Secondary Flows in a Diffusing S-Duct," The University of Tennessee Space Institute Preliminary Copy Final Report for NASA Contract NAG3 233, Sept. 1984.

[10] Taylor, A. M. K. P., Whitelaw, J. H., and Yianneskis, M., "Developing Flow in S-Shaped Ducts I - Square Cross-Section Duct," Imperial College of Science and Technology NASA Contractor Report 3550, 1982.

[11] Taylor, A. M. K. P., Whitelaw, J. H., and Yianneskis, M., "Curved Ducts with Strong Secondary Motion: Velocity Measurements of Developing Laminar and Turbulent Flow," *Journal of Fluids Engineering*, Vol. 104, Sept. 1982, pp. 350–359.

[12] Guo, R. W. and Seddon, J., "Swirl Characteristics of an S-shaped Air Intake With Both Horizontal and Vertical Offsets," *Aeronautical Quarterly*, Vol. 34, May 1983, pp. 130–146.

[13] Sullivan, J. P., Murthy, S. N. B., Davis, R., and Hong, S., "S-Shaped Duct Flows," Office of Naval Research Contract No. N-78-C-0710, Dec. 1982.

[14] Towne, C. E. and Anderson, B. H., "Numerical Simulation of Flows in Curved Diffusers with Cross-Sectional Transitioning Using a Three-Dimensional Viscous Analysis," AIAA paper, 1981. (also NASA TM 81672).

[15] Towne, C. E., "Computation of Viscous Flow in Curved Ducts and Comparison with Experimental Data," AIAA Paper 84-0531, 1984.

[16] Vakili, A., Wu, J. M., Hingst, W. R., and Towne, C. E., "Comparison of Experimental and Computational Compressible Flow in a S-Duct," AIAA Paper 84-0033, 1984.

[17] Povinelli, L. A. and Towne, C. E., "Viscous Analysis of Flow Through Subsonic and Supersonic Intakes," NASA TM 88831, 1986.

[18] Smith, C. F., Bruns, J. E., Harloff, G. J., and Debonis, J. R., "Three-Dimensional Compressible Turbulent Computations for a Diffusing S-Duct," Sverdrup Technology, Inc. NASA CR 4392, 1991.

[19] Harloff, G. J., Reichert, B. A., and Wellborn, S. R., "Navier-Stokes Analysis and Experimental Data Comparison of Compressible Flow in a Diffusing S-Duct," AIAA Paper 92-2699, 1992.

[20] Harloff, G. J., Smith, C. F., Bruns, J. E., and DeBonis, J. R., "Navier-Stokes Analysis of Three-Dimensional S-Ducts," Submitted to AIAA Journal of Aircraft.

[21] Porro, A. R., Keith, T. G., and Hingst, W. R., "A Laser-Induced Heat Flux Technique for Convective Heat Transfer Measurements in High Speed Flows," NASA TM 105177, Oct. 1991.

[22] Squire, L. C., Maltby, R. L., Keating, R. F. A., and Stanbrook, A., "The Surface Oil Flow Technique," *Flow Visualization in Wind Tunnels Using Indicators*, edited by R. L. Maltby, AGARD, Apr. 1962, pp. 1–28. AGARDograph 70.

[23] Reichert, B. A., Hingst, W. R., and Okiishi, T. H., "An Experimental Comparison of Nonswirling and Swirling Flow in a Circular-to-Rectangular Transition Duct," AIAA Paper 91-0342, 1991. (also NASA TM 104359).

[24] Davis, D. O., Hingst, W. R., and Porro, A. R., "Experimental Investigation of a Single Flush-Mounted Hypermixing Nozzle," AIAA Paper 90-5240, 1990. (also NASA TM 103726).

[25] Wendt, B. Private communications, June 1992.

[26] "Model 780B/T Pressure Measurement System Users Manual," Pressure Systems Incorperated, Hampton, Virginia, Sept. 1983. 1st ed.

[27] Levy, R., Briley, W. R., and McDonald, H., "Viscous Primary/Secondary Flow Analysis for Use with Nonorthogonal Coordinate Systems," AIAA Paper 83-0556, Jan. 1983.

[28] Briley, W. R. and McDonald, H., "Three-Dimensional Viscous Flows with Large Secondary Velocities," *Journal of Fluid Mechanics*, Vol. 144, Mar. 1984, pp. 47–77.

[29] Anderson, B. H., "The Aerodynamic Characteristics of Vortex Ingestion for the F/A-18 Inlet Duct," AIAA Paper 91-0130, 1991.

[30] Wellborn, S. R., "Computation of the Flow in a Circular-to-Rectangular Transition Duct Using a Modified PNS Solver," AIAA tech. rep., 1991. Prepared for the 1991 AIAA Region V Student Conference.

[31] McDonald, H. and Camarata, F. J., "An Extended Mixing Length Approach for Computing the Turbulent Boundary Layer Development," *Proceedings, Stanford Conference of Turbulent Boundary Layers*, Vol. 1, Stanford University, 1969, pp. 83–98.

[32] "PEPSIG 3-D Parabolized Navier-Stokes Computer Code : User's Manual," NASA Lewis Research Center, Cleveland, Ohio, 1988.

[33] Reichert, B. A., *A Study of High Speed Flows in an Aircraft Transition Duct*, Ph.D. Dissertation, Iowa State University, Ames, Iowa, 1991. (also NASA TM 104449).

[34] Tobak, M. and Peake, D. J., "Topology of Three-Dimensional Separated Flows," *Annual Review of Fluid Mechanics*, Vol. 14, 1982, pp. 61–85.

[35] Lighthill, M. J., "Attachment and Separation in Three-Dimensional Flow," *Laminar Boundary Layers*, edited by L. Rosenhead, Oxford University Press, Mar. 1963, pp. 72–82.

[36] Hornung, H. and Perry, A. E., "Some Aspects of Three-Dimensional Separation, Part I: Streamsurface Bifurcations," *Zeitschrift fur Flugwissenschaften und Weltraumforschung*, Vol. 8, Mar. 1984, pp. 77–87.

[37] Perry, A. E. and Hornung, H., "Some Aspects of Three-Dimensional Separation, Part II: Vortex Skeletons," *Zeitschrift fur Flugwissenschaften und Weltraumforschung*, Vol. 8, Mar. 1984, pp. 155–160.

APPENDIX A

THREE-HOLE PROBE CALIBRATION AND DATA REDUCTION TECHNIQUES

This appendix contains supplementary information on the calibration and data reduction of a three-hole probe. The information covering five-hole probes can be found in Appendix B. Both the three- and five-hole probe calibration techniques used in this thesis closely follow the methods developed by Reichert [33]. The reader is referred to this reference for further details.

The Three-Hole Probe

A drawing of the cobra three-hole probe used in this experiment is shown in Figure A.1. The probe axes and nomenclature assigned to the individual openings are also presented. The probe was constructed of three silver brazed stainless steel tubes, each having an inside diameter of 0.056 cm. The opening of the center tube was normal to its centerline. The

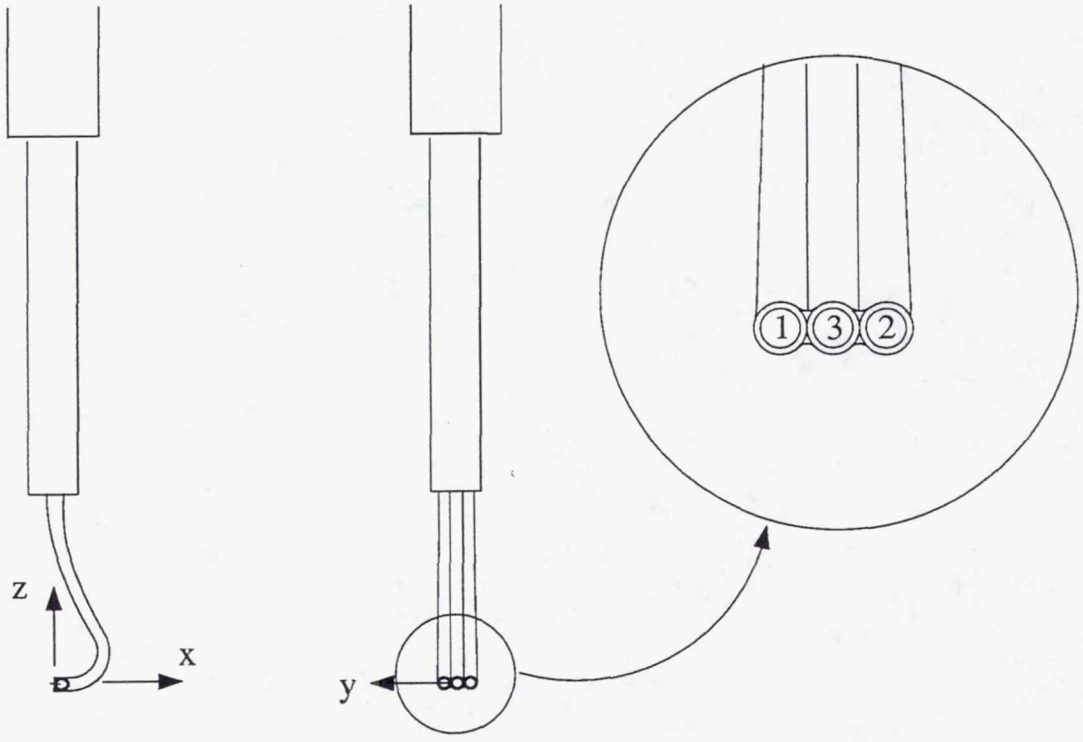

Figure A.1 The cobra three-hole probe

openings of the two outer tubes were inclined 30° to their centerline. This arrangement resulted in yawing symmetry.

Yaw-Nulling Calibration

The main objective of performing a yaw-nulling three-hole probe calibration was to empirically determine the relationships between the flow conditions (p_o, p) and the three measured pressures of the probe (p_1, p_2, p_3). Since the yaw angle was measured directly, the flow total and static pressures were determined as functions of two of the three measured probe pressures. To aid calibration, the three pressures measured during probe calibration were nondimensionalized as indicated in Equation A.1. Here, p_i is the measured pressure of port i (i=1,2,3) and p_o and p are the local flow total and static pressures.

$$C_{p_i} = \frac{p_i - p}{p_o - p} = f_i(Re,\ M,\ \gamma,\ \alpha,\ \beta) \tag{A.1}$$

The pressure coefficients were dependent on Mach number, M, Reynolds number, Re, specific heat ratio, γ, the flow pitch angle, α, and the flow yaw angle, β. The Mach number and Reynolds number were interdependent during the calibration and the test, therefore the Reynolds number was removed from the list of independent variables. The specific heat ratio was also removed since both the calibration and the experimental were performed in air. Finally, the experimental flow field was assumed to contain no pitch component and the yaw angle was measured directly, so both flow angles were omitted from the list of independent variables. This left Mach number as the only calibration variable.

The calibration was accomplished by varying Mach number while measuring the probe pressures. The probe openings were positioned in the center of the jet flow field produced by the calibration facility. During calibration, the total pressure was measured by the Pitot probe in the calibration facility. Static pressure was simply the test cell atmospheric pressure. The probe was nulled to produce equal measured pressures for ports 1 and 2. Typical calibration results are shown in Figure A.2. The three coefficients are plotted as functions of total-to-static pressure ratio. By varying Mach number, the total-to-static pressure ratio was also varied. The coefficient for the center opening, Cp_3, was independent of Mach number. The coefficients for the side openings , Cp_1 and Cp_2, were equal (since $p_1 = p_2$) and varied linearly with total-to-static pressure ratio for the applicable experimental range.

A Taylor series expansion was used to approximate the relation between the flow conditions and the measured pressures. The approximations for each pressure coefficient are given in Equations A.3 and A.2. Notice that only constant and linear terms of the expansion are included.

$$\widehat{C}p_{1,2} = b_0 + b_1\left(\frac{p_o}{p}\right) + \emptyset\left(\frac{p_o}{p}\right)^2 + \cdots = b_0 + b_1\left(\frac{p_o}{p}\right) \tag{A.2}$$

$$\widehat{C}p_3 = a_0 + \emptyset\left(\frac{p_o}{p}\right) + \emptyset\left(\frac{p_o}{p}\right)^2 + \cdots = a_0 \tag{A.3}$$

The calibration coefficient a_0 was simply equal to Cp_3, which was one. The calibration coefficients b_0 and b_1 were found using a least squares procedure. This procedure required finding the coefficients which minimized the error, given by Equation A.4. The minimization was accomplished by taking the derivative of the error function (Equation A.4) with respect to the coefficients b_0 and b_1 and equating the result to zero. The equations developed from

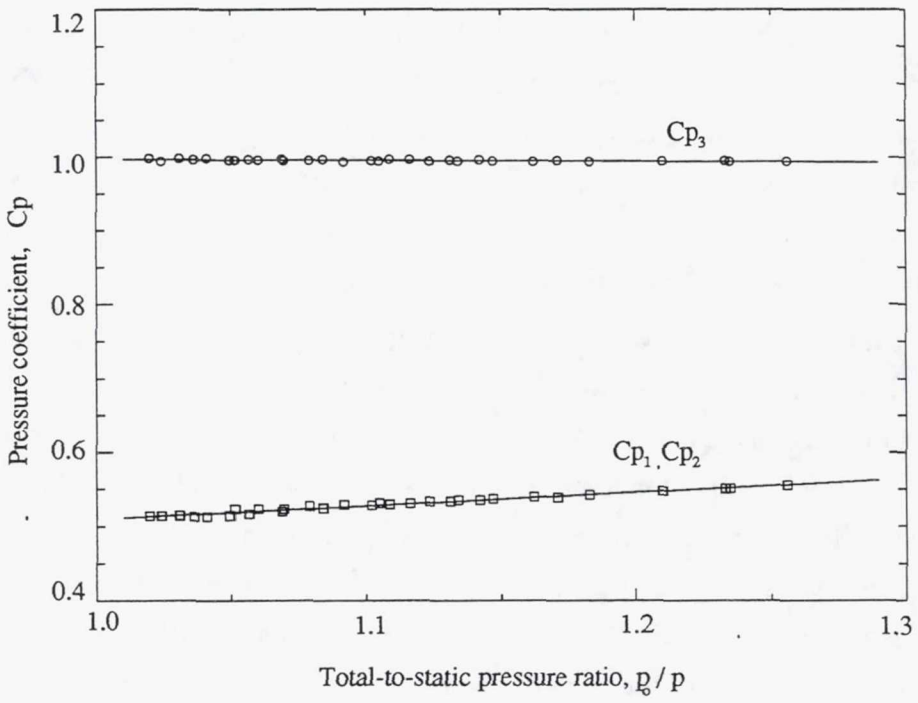

Figure A.2 Variation of the three-hole probe pressure coefficients with total-to-static pressure ratio

this minimization process are presented in Equations A.5 and A.6. Here, N refers to the total number of calibration measurements. These two equations were solved simultaneously to obtain b_0 and b_1.

$$E = \sum_{n=1}^{N} \left[Cp_{1,2} - \left(b_0 + b_1 \frac{p_0}{p} \right) \right]^2 \tag{A.4}$$

$$b_0 N + b_1 \sum_{n=1}^{N} \left(\frac{p_0}{p} \right)_n = \sum_{n=1}^{N} (Cp_{1,2})_n \tag{A.5}$$

$$b_0 \sum_{n=1}^{N} \left(\frac{p_o}{p} \right)_n + b_1 \sum_{n=1}^{N} \left(\frac{p_o}{p} \right)_n^2 = \sum_{n=1}^{N} (Cp_{1,2})_n \left(\frac{p_o}{p} \right)_n \tag{A.6}$$

Data Reduction

The local total and static pressures were found from the Taylor series approximations to the calibration pressure coefficients. The total pressure was simply the center opening pressure, p_3, as stated in Equation A.7. The static pressure was found by equating the pressure coefficient $Cp_{1,2}$ (Equation A.1) to the Taylor series expansion of $Cp_{1,2}$ (Equation A.2) and then solving explicitly for the static pressure. The resulting quadratic, given in Equation A.8 , was formulated. One root of the quadratic was within the calibration region while the other root was outside the range of calibration. No difficultly arose in determining the correct static pressure. The total and static pressures were then used to determine the local Mach number as given by Equation A.9. Since the yaw flow angle varied only slightly in the experimental flow, no further data reduction was necessary.

$$p_o = p_3 \tag{A.7}$$

$$p = \frac{-b \pm \sqrt{b^2 - 4ac}}{2a} \quad : \quad a = 1 - b_0, \quad b = (b_0 - b_1)p_3 - p_{1,2}, \quad c = b_1 p_3^2 \tag{A.8}$$

$$M = \left\{ \left[\left(\frac{p_o}{p} \right)^{\frac{\gamma-1}{\gamma}} - 1 \right] \frac{2}{\gamma - 1} \right\}^{1/2} \tag{A.9}$$

APPENDIX B

FIVE-HOLE PROBE CALIBRATION AND DATA REDUCTION TECHNIQUES

This appendix contains supplementary information on the calibration methods and data reduction techniques for a five-hole probe. Both yaw-nulling and non-yaw-nulling methods are reviewed. The information covering three-hole probes can be found in Appendix A. Both the three- and five-hole probe calibration techniques used in this thesis closely follow the methods developed by Reichert [33]. The reader in referred this reference for further details.

The Five-Hole Probe

A drawing of the five-hole probe used in this experiment is shown in Figure B.1. The probe axes and nomenclature assigned to the individual openings are also presented. The probe was constructed of five silver brazed stainless steel tubes, each having an inside diameter of 0.056 cm. The opening of the center tube was normal to its centerline. The openings of the four outer tubes were inclined 45° to their centerlines. This arrangement resulted in yawing and pitching symmetry.

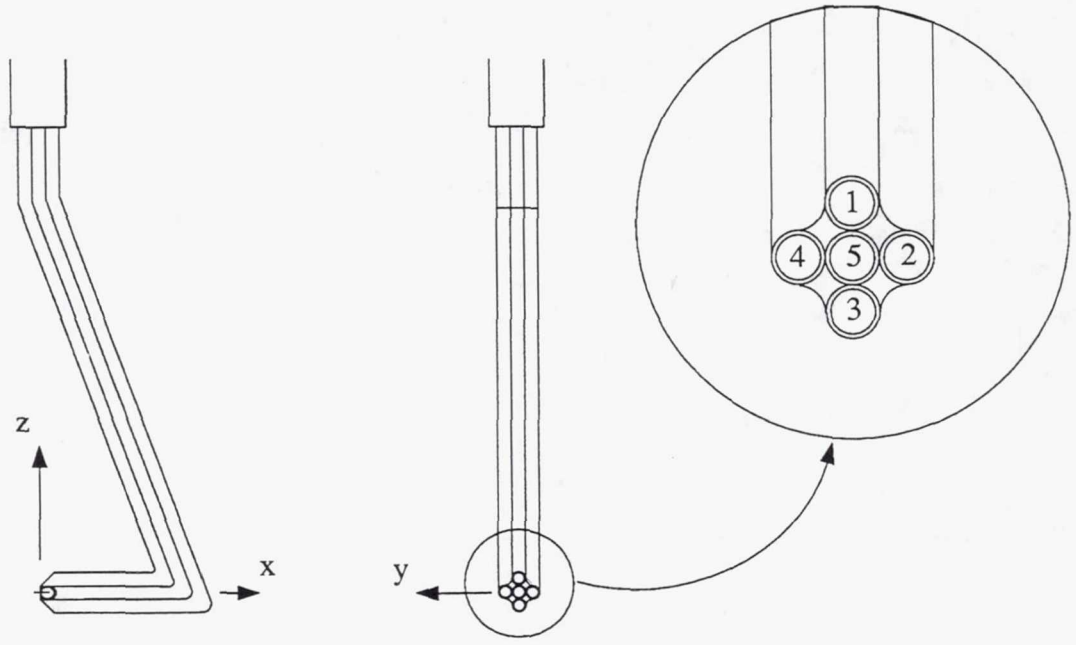

Figure B.1 Pictorial of the five-hole probe

Yaw-Nulling Calibration

Reichert previously developed an effective yaw-nulling calibration technique for five-hole probes [33]. Reichert's calibration method permits the unknown flow conditions within the test flow field to be explicitly calculated during data reduction. The flow conditions are determined from measured probe pressures and the calibration coefficients established empirically from actual calibration data. This empirical calibration technique is quit different than the theoretical calibration approaches used by Vakili *et al.* [9] in their studies. The following section summarizes Reichert's calibration technique and is included for completeness.

The yaw-nulled five-hole probe calibration empirically determined the relationships between the flow conditions (p_0, p, and α_c) and the five measured pressures of the probe ($p_1, \cdots, p_5$). The yaw angle, β, was measured directly buy nulling the probe in the experimental flow field. In practice, the flow conditions (p_0, p, and α_c) were found from three of the five measured pressures.

The pressures measured during probe calibration were nondimensionalized as indicated in Equation B.1. Here, p_i is the measured pressure of port i (i= 1,..,5) and p_o and p are the local flow total and static pressures.

$$Cp_i = \frac{p_i - p}{p_o - p} = f_i(M, Re, \gamma, \alpha_c, \beta) \tag{B.1}$$

As in the three-hole probe calibration, the pressure coefficients were dependent on Mach number, M, Reynolds number, Re, specific heat ratio, γ, measured flow pitch angle, α_c, and the flow yaw angle, β. Mach number and Reynolds number were linked during testing and calibration, therefore Reynolds number was removed from the list of independent variables. Both the calibration and the experiment were performed in air, so the specific heat ratio was also removed. Finally, the yaw angle was omitted since the probe was nulled. Therefore, Mach number and pitch angle were the independent calibration variables.

The calibration was accomplished by varying Mach number and pitch angle while measuring the probe pressures. The probe openings were positioned in the center of the jet flow field produced by the calibration facility. The total pressure was measured by the Pitot tube, shown in Figure III.1. Static pressure was the test-cell atmospheric pressure. The probe was nulled to produce equal measured pressures for ports 2 and 4. Typical calibration

results are shown in Figure B.2. The five coefficients are plotted as functions of pitch angle, α_c, for three Mach numbers (M = 0.2, 0.4, 0.6). The pressure coefficients for this probe were virtually independent of Mach number in the range of Mach numbers tested. Consequently, the pressure coefficients were functions of pitch angle alone.

Reichert points out that care must be taken when defining the pitch angle. Probe pressures responded to the velocity relative to the probe axis, not to the velocity relative to the coordinates of the measurement plane, as depicted in Figure B.3. The true pitch angle (pitch angle relative to the measurement plane), α, was related to the measured probe pitch angle, α_c, and the deflection angle, α_o, as given in Equation B.2. All of these angles were measured positive in the clockwise direction. The true pitch angle (α) was defined to be the angle between the velocity vector to the measurement plane normal. The measured probe pitch angle (α_c) was the angle between the velocity vector to the probe axis and was determined from calibration relationships. The deflection angle (α_o) was the angle between the probe axis to the measurement plane normal. The deflection angle was a result of

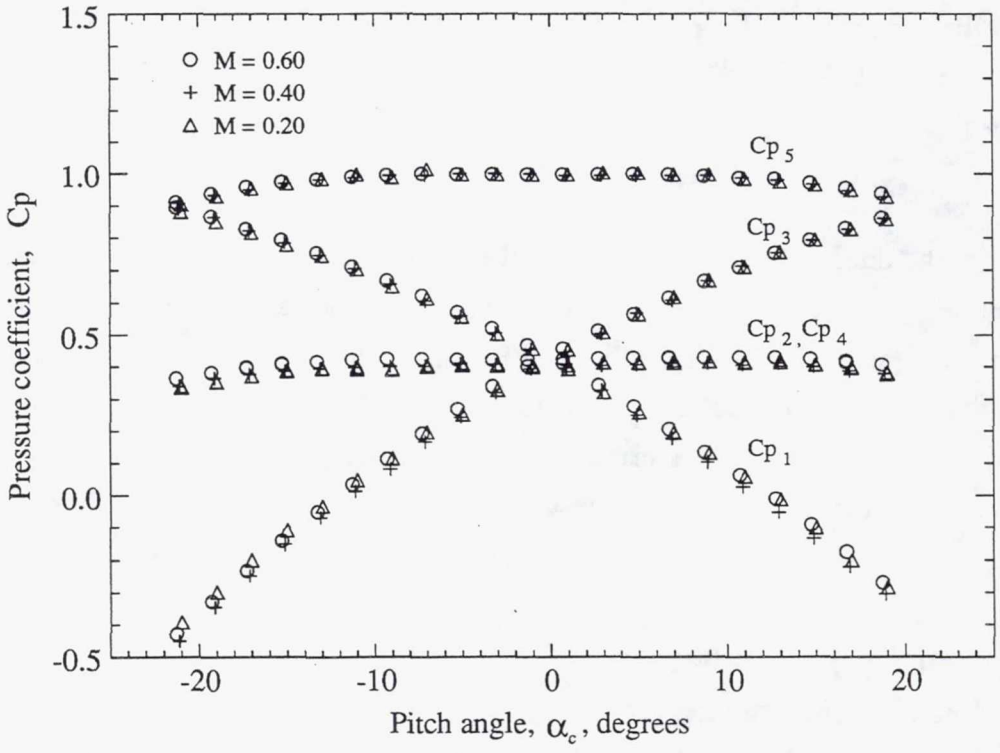

Figure B.2 Variation of pressure coefficients with pitch angle for various Mach numbers

imperfect instrumentation manufacturing, occasional bumping of the probe tip during testing and/or aerodynamic loading of the probe while cantilevered out into the experimental flow field. One simple way of calculating the deflection angle, α_o, is presented in the Yaw-Nulling Data Reduction Section. It is important to remember that the calibration was based on the probe pitch angle, α_c, and not the true pitch angle, α.

$$\alpha = \alpha_c + \alpha_o \tag{B.2}$$

Taylor series expansions were used to approximate the relations between the flow conditions and the measured pressures. The approximations for each pressure coefficient are given in Equations B.3–B.7. Simplifications to the individual calibration coefficients within each approximation are included. These simplifications were due to probe symmetry and are extensively reviewed in Reference [33].

$$\widehat{C}p_1 = a_1 + a_2\alpha_c + a_3\alpha_c^2 \tag{B.3}$$

$$\widehat{C}p_2 = a_1 + a_4\alpha_c^2 \tag{B.4}$$

$$\widehat{C}p_3 = a_1 - a_2\alpha_c + a_3\alpha_c^2 \tag{B.5}$$

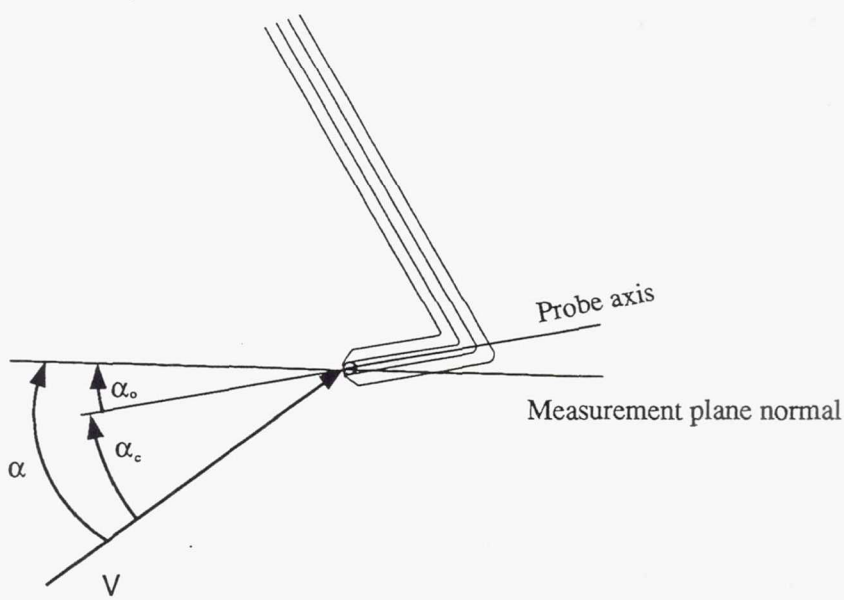

Figure B.3 Five hole probe pitch angles

$$\widehat{C}p_4 = a_1 + a_4\alpha_c^2 \tag{B.6}$$

$$\widehat{C}p_5 = 1 + a_5\alpha_c^2 \tag{B.7}$$

Reichert proved that relationships between these approximations and the flow conditions (p_0, p, and α_c) existed. The first, third and fifth expansions were need to develop the relationships. Hence, only four of the five calibration coefficients (a_1, a_2, a_3 and a_5) were determined. These four calibration coefficients were found using a least squares procedure. This procedure required finding the values of the coefficients which minimized the error, represented by Equation B.8. Here, J is the total number of calibration Mach numbers and K_j is the total number of calibration pitch angles for each Mach number.

$$E = \sum_{i=1,3,5} \sum_{j=1}^{J} \sum_{k=1}^{K_j} \left[Cp_i(M_j, \alpha_{c_k}) - \widehat{C}p_i(M_j, \alpha_{c_k}) \right]^2 \tag{B.8}$$

The minimization was accomplished by taking the derivative of the error function (Equation B.8) with respect to the coefficients (a_1, a_2, a_3 and a_5) and equating the results to zero. The equations developed from this minimization process are presented in Equations B.9–B.12. Equations B.10 and B.12 were solved independently to obtain the coefficients a_2 and a_5. Equations B.9 and B.11 were solved simultaneously to obtain the coefficients a_1 and a_3.

$$a_1 \sum_{j=1}^{J} K_j + a_3 \sum_{j=1}^{J} \sum_{k=1}^{K_j} \alpha_{c_k}^2 = \frac{1}{2} \sum_{j=1}^{J} \sum_{k=1}^{K_j} [Cp_1(M_j, \alpha_{c_k}) + Cp_3(M_j, \alpha_{c_k})] \tag{B.9}$$

$$a_2 \sum_{j=1}^{J} \sum_{k=1}^{K_j} \alpha_{c_k}^2 = \frac{1}{2} \sum_{j=1}^{J} \sum_{k=1}^{K_j} [Cp_1(M_j, \alpha_{c_k}) - Cp_3(M_j, \alpha_{c_k})]\alpha_{c_k} \tag{B.10}$$

$$a_1 \sum_{j=1}^{J} \sum_{k=1}^{K_j} \alpha_{c_k}^2 + a_3 \sum_{j=1}^{J} \sum_{k=1}^{K_j} \alpha_{c_k}^4 = \frac{1}{2} \sum_{j=1}^{J} \sum_{k=1}^{K_j} [Cp_1(M_j, \alpha_{c_k}) + Cp_3(M_j, \alpha_{c_k})]\alpha_{c_k}^2 \tag{B.11}$$

$$\sum_{j=1}^{J}\sum_{k=1}^{K_j}\alpha_{c_k}^2 + a_5\sum_{j=1}^{J}\sum_{k=1}^{K_j}\alpha_{c_k}^4 = \sum_{j=1}^{J}\sum_{k=1}^{K_j} Cp_5(M_j,\alpha_{c_k})\,\alpha_{c_k}^2 \tag{B.12}$$

Yaw-Nulling Data Reduction

The data reduction procedure determined the local total pressure, static pressure and Mach vector components from the Taylor series approximations to the calibration pressure coefficients and the measured yaw angle. The reduction process began by determining the pitch angle from a ratio of differences of measured pressures, represented by Equation B.13. This equation is a quadratic in α_c. Although two roots existed for Equation B.13, one root was always within while the second root was well outside the range of calibrated pitch angles. No difficulty arose in deciding which root was correct.

$$\frac{(p_1 - p_3)}{2p_5 - (p_1 + p_3)} = \frac{a_2\,\alpha_c}{(a_5 - a_3)\,\alpha_c^2 + 1 - a_1} \tag{B.13}$$

The flow local total and static pressures were found using Equation B.14 and the previously determined value of α_c. These total were then used to determine the magnitude of the local Mach number, as given by Equation B.15.

$$\begin{bmatrix} a_1 + a_3\,\alpha_c^2 & 1 - a_1 - a_3\,\alpha_c^2 \\ 1 + a_5\,\alpha_c^2 & -a_5\,\alpha_c^2 \end{bmatrix}\begin{bmatrix} p_o \\ p \end{bmatrix} = \begin{bmatrix} \frac{1}{2}(p_1 + p_3) \\ p_5 \end{bmatrix} \tag{B.14}$$

$$M = \left\{\left[\left(\frac{p_o}{p}\right)^{\frac{\gamma-1}{\gamma}} - 1\right]\frac{2}{\gamma - 1}\right\}^{1/2} \tag{B.15}$$

The last step in the data reduction procedure was to calculate the components of the Mach vector relative to the measurement plane. The three components of a unit vector representing the flow direction were defined as $e_{x'}$, $e_{y'}$ and $e_{z'}$. The component $e_{x'}$ was in the direction normal to the measurement plane and in the direction of streamwise flow. The components $e_{y'}$ and $e_{z'}$ were projections of the unit vector onto the measurement plane and were mutually orthogonal. These three components were found with Equation B.16.

$$\begin{bmatrix} e_{x'} \\ e_{y'} \\ e_{z'} \end{bmatrix} = \begin{bmatrix} 1 & 0 & 0 \\ 0 & \cos\phi & -\sin\phi \\ 0 & \sin\phi & \cos\phi \end{bmatrix}\begin{bmatrix} \cos(\beta + \beta_o)\cos(\alpha_c + \alpha_o) \\ \sin(\beta + \beta_o)\cos(\alpha_c + \alpha_o) \\ \sin(\alpha_c + \alpha_o) \end{bmatrix} \tag{B.16}$$

In Equation B.16, the second matrix determined the flow direction relative to the probe coordinate system (Figure B.1). The first matrix transformed the flow components from the probe coordinates to the measurement plane coordinates. Two new variables were introduced: the reference yaw angle, β_o, and the orientation angle, ϕ. The reference yaw angle, β_o, was assigned the negative value of the yaw angle when the probe was nulled at the centerline. Therefore, all subsequent yaw angles along a radial traverse were referenced to β_o. The orientation angle, ϕ, was simply the rotation angle about the centerline within a measurement plane (Figure III.4).

Before the three separate components were found, the deflection angle, α_o, was determined. The equation which established the deflection angle is given in Equation B.17. This equation was derived by equating the true pitch angle at the centerline when measured from two separate orientation angles. Equation B.17 assumes that the true pitch angle at the centerline was constant and that the deflection angle did not change while rotating from the first to the second orientation angle. Care was taken while handling the probe in order to insure the later approximation was a good assumption.

$$\alpha_o = \tan^{-1}\left[\frac{\sin(\phi_2 + \alpha_{c_2}) - \sin(\phi_1 + \alpha_{c_1})}{\cos(\phi_1 + \alpha_{c_1}) - \cos(\phi_2 + \alpha_{c_2})}\right] \tag{B.17}$$

In practice, the deflection angle was calculated only once as described above. From this deflection angle value, the true pitch angle at the centerline, $\alpha_{c_{cl}}$, could then be calculated, and hence, the left side of Equation B.16 was known at the centerline. For an arbitrary orientation angle, therefore, Equation B.18 applied at the duct centerline.

$$\alpha_o = \sin^{-1}(e_{z_{cl}'}) - \alpha_c - \phi \tag{B.18}$$

Equation B.18 was used in general to find the deflection angle along a single radial traverse. In Equations B.17 and B.18, the required measure centerline pitch angles were previously found from Equation B.13.

Non-Yaw-Nulling Calibration

In the remaining sections, the yaw-nulling calibration technique is extended to a non-yaw-nulling method. As before, the calibration permits the unknown flow conditions in the test flow field to be found from the five measured pressures and the calibration coefficients.

However, the non-yaw-nulling data reduction technique requires an iteration scheme to solve the non-linear relationships which arise. The following section summarizes details involved with a forth-order approximation calibration procedure.

The non-yaw-nulled five-hole probe calibration empirically determined the relationships between the flow conditions (p_0, p, α_c, and β_c) and the five measured pressures of the probe ($p_1, \cdots, p_5$). The pressures measured during probe calibration were nondimensionalized as indicated in Equation B.1. The pressure coefficients were dependent on Mach number, M, Reynolds number, Re, specific heat ratio, γ, the measured flow pitch angle, α_c, and the measured flow yaw angle, β_c. As in the yaw-nulled probe calibration, Reynolds number and specific heat ratio were removed from the list of independent variables. However, since the probe was insensitive to changes in Mach number (determined in the yaw-nulled calibration), Mach number was also omitted. Therefore, the measured pitch angle and yaw angle were the independent calibration variables.

The calibration was accomplished by varying pitch angle and yaw angle while measuring the probe pressures. The probe openings were positioned in the center of the jet flow field produced by the calibration facility. The total pressure was measured by the Pitot tube, shown in Figure III.1. Static pressure was the test-cell atmospheric pressure. Typical calibration results are shown in Figure B.4. The five coefficients are plotted here as functions of measured pitch angle, α_c, and measured yaw angle, β_c, for one Mach number (M = 0.4).

Similar to the yaw-nulled calibration, care was taken when defining the pitch angle. However, defining the yaw angle was less restrictive since the probe was rotated about its z-axis for the first measurement at the centerline of the duct (ie... a reference yaw angle, β_o, was defined as in the yaw-nulled calibration). The true pitch angle, α, was related to the measured probe pitch angle, α_c, and the deflection angle, α_o, as given in Equation B.2 and shown in Figure B.3. Again, all of these angles were measured positive in the clockwise direction.

Taylor series expansions were used to approximate the relationships between the flow conditions and the measured pressures. An approximation for a general pressure coefficient is given in Equation B.19. For a forth-order approximation, there exists 15 coefficients for each probe hole. Therefore, an "unsymmetric" five-hole probe has 75 coefficients which would need to be determined (... a task to which no one would look forward) However, because

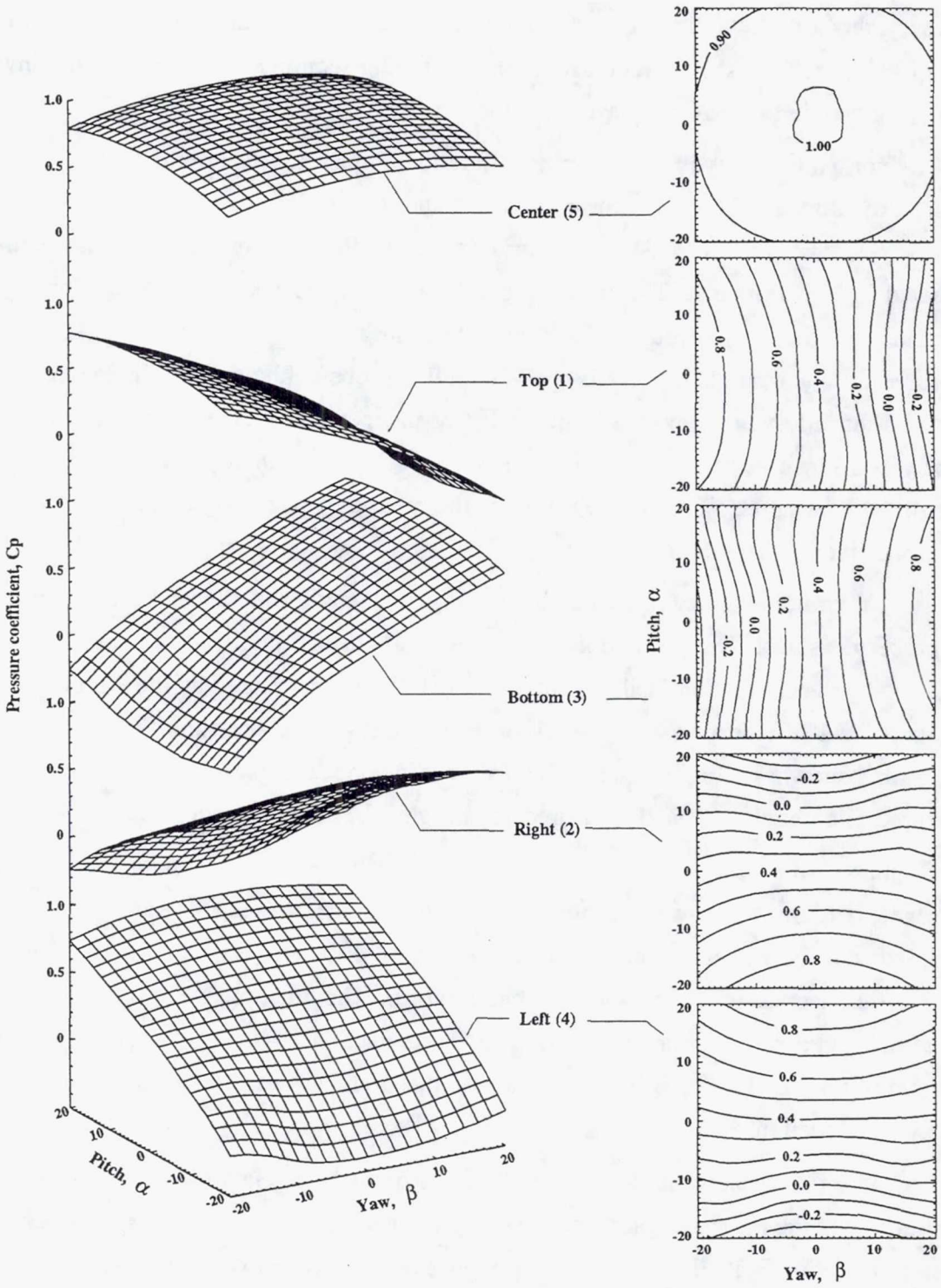

Figure B.4 Variation of pressure coefficients with pitch and yaw angle for 0.4 Mach number

the five-hole probe was symmetric, most of the calibration coefficients were eliminated. The simplifications to the calibration coefficients, due to probe symmetry, are now reviewed.

$$
\begin{aligned}
\widehat{C}p_i(\alpha_c, \beta_c) = & a_{i00} + \\
& a_{i10}\alpha_c + a_{i01}\beta_c + \\
& a_{i20}\alpha_c^2 + a_{i11}\alpha_c\beta_c + a_{i02}\beta_c^2 + \\
& a_{i30}\alpha_c^3 + a_{i21}\alpha_c^2\beta_c + a_{i12}\alpha_c\beta_c^2 + a_{i03}\beta_c^3 + \\
& a_{i40}\alpha_c^4 + a_{i31}\alpha_c^3\beta_c + a_{i22}\alpha_c^2\beta_c^2 + a_{i13}\alpha_c\beta_c^3 + a_{i04}\beta_c^4 + \cdots
\end{aligned}
\tag{B.19}
$$

There existed three symmetry conditions which held for the five-hole probe. The first was a reflection across the *xz*-plane. The second was a reflection across the *xy*-plane. The third was a 90° rotation about the *x*-axis. These symmetry conditions had important consequences for the Taylor series approximations. The simplifications to the calibration coefficients from each symmetry condition were developed by Reichert and are summarized below.

1. Symmetric with respect to reflection across the xz-plane. Therefore

   a. $Cp_1(\alpha_c, \beta_c) = Cp_1(\alpha_c, -\beta_c)$

   - $a_{101} = 0$
   - $a_{111} = 0$
   - $a_{121} = 0$
   - $a_{103} = 0$
   - $a_{131} = 0$
   - $a_{113} = 0$

   b. $Cp_3(\alpha_c, \beta_c) = Cp_3(\alpha_c, -\beta_c)$

   - $a_{301} = 0$
   - $a_{311} = 0$
   - $a_{321} = 0$
   - $a_{303} = 0$
   - $a_{331} = 0$
   - $a_{313} = 0$

   c. $Cp_5(\alpha_c, \beta_c) = Cp_5(\alpha_c, -\beta_c)$

   - $a_{501} = 0$
   - $a_{511} = 0$
   - $a_{521} = 0$
   - $a_{503} = 0$
   - $a_{531} = 0$
   - $a_{513} = 0$

d. $Cp_2(\alpha_c, \beta_c) = Cp_4(\alpha_c, -\beta_c)$

- $a_{200} = a_{400}$
- $a_{210} = a_{410}$
- $a_{201} = -a_{401}$
- $a_{220} = a_{420}$
- $a_{211} = -a_{411}$
- $a_{202} = a_{402}$
- $a_{221} = -a_{421}$
- $a_{203} = -a_{403}$
- $a_{240} = a_{440}$
- $a_{231} = -a_{431}$
- $a_{222} = a_{422}$
- $a_{213} = -a_{413}$
- $a_{204} = a_{404}$

2. Symmetric with respect to reflection across the xy-plane. Hence

a. $Cp_2(\alpha_c, \beta_c) = Cp_2(-\alpha_c, \beta_c)$

- $a_{210} = 0$
- $a_{211} = 0$
- $a_{212} = 0$
- $a_{230} = 0$
- $a_{231} = 0$
- $a_{213} = 0$

b. $Cp_4(\alpha_c, \beta_c) = Cp_4(-\alpha_c, \beta_c)$

- $a_{410} = 0$
- $a_{411} = 0$
- $a_{412} = 0$
- $a_{430} = 0$
- $a_{431} = 0$
- $a_{413} = 0$

c. $Cp_5(\alpha_c, \beta_c) = Cp_5(-\alpha_c, \beta_c)$

- $a_{510} = 0$
- $a_{511} = 0$
- $a_{512} = 0$
- $a_{530} = 0$
- $a_{531} = 0$
- $a_{513} = 0$

d. $Cp_1(\alpha_c, \beta_c) = Cp_3(-\alpha_c, \beta_c)$

- $a_{100} = a_{300}$
- $a_{110} = -a_{310}$
- $a_{101} = a_{301}$
- $a_{120} = a_{320}$
- $a_{111} = -a_{311}$
- $a_{102} = a_{302}$
- $a_{130} = -a_{330}$
- $a_{112} = -a_{312}$
- $a_{140} = a_{340}$
- $a_{131} = -a_{331}$
- $a_{122} = a_{322}$
- $a_{113} = -a_{313}$
- $a_{104} = a_{304}$

3. Symmetric with respect to 90° rotation about the x-axis. Consequently

   a. $Cp_1(0, \beta_c) = Cp_2(-\beta_c, 0)$ and $Cp_1(\alpha_c, 0) = Cp_2(0, \alpha_c)$

   - $a_{100} = a_{200}$
   - $a_{110} = a_{201}$
   - $a_{101} = -a_{210}$
   - $a_{120} = a_{202}$
   - $a_{102} = a_{220}$
   - $a_{130} = a_{203}$
   - $a_{103} = -a_{230}$
   - $a_{140} = a_{204}$
   - $a_{104} = a_{240}$

   b. $Cp_5(0, \beta_c) = Cp_5(-\beta_c, 0)$ and $Cp_5(\alpha_c, 0) = Cp_5(0, \alpha_c)$

   - $a_{510} = a_{501}$
   - $a_{501} = -a_{510}$
   - $a_{520} = a_{502}$
   - $a_{530} = a_{503}$
   - $a_{503} = -a_{530}$
   - $a_{540} = a_{504}$

Finally, the aerodynamic stagnation condition implied

$$Cp_5(0, 0) = 1 \Rightarrow a_{500} = 1 \ . \tag{B.20}$$

The resulting simplifications to the each of the individual coefficients are listed in Table B.1. Notice that only 14 independent calibration coefficients were needed for the Taylor series approximations.

Defining the vectors $\hat{\mathrm{C}}\mathrm{p}_{jk}$, u and a^T (Equations B.21 and B.22), and the matrix M_{jk} (Equation B.23) enables a system of equations to be written, as represented in Equation B.24.

$$\mathrm{Cp}_{jk} = \begin{bmatrix} Cp_1(\alpha_{c_j}, \beta_{c_k}) \\ Cp_2(\alpha_{c_j}, \beta_{c_k}) \\ Cp_3(\alpha_{c_j}, \beta_{c_k}) \\ Cp_4(\alpha_{c_j}, \beta_{c_k}) \\ Cp_5(\alpha_{c_j}, \beta_{c_k}) \end{bmatrix} \qquad \widehat{\mathrm{C}}\mathrm{p}_{jk} = \begin{bmatrix} \widehat{C}p_1(\alpha_{c_j}, \beta_{c_k}) \\ \widehat{C}p_2(\alpha_{c_j}, \beta_{c_k}) \\ \widehat{C}p_3(\alpha_{c_j}, \beta_{c_k}) \\ \widehat{C}p_4(\alpha_{c_j}, \beta_{c_k}) \\ \widehat{C}p_5(\alpha_{c_j}, \beta_{c_k}) \end{bmatrix} \qquad \mathrm{u} = \begin{bmatrix} 0 \\ 0 \\ 0 \\ 0 \\ 1 \end{bmatrix} \tag{B.21}$$

$$\begin{aligned} \mathrm{a}^T = [\, & a_{100} \quad a_{110} \quad a_{120} \quad a_{102} \quad a_{502} \quad a_{130} \quad a_{112} \,] \\ [\, & a_{221} \quad a_{140} \quad a_{122} \quad a_{222} \quad a_{104} \quad a_{540} \quad a_{522} \,] \end{aligned} \tag{B.22}$$

Table B.1 Results of probe symmetry for calibration coefficients

	$i=1$	$i=2$	$i=3$	$i=4$	$i=5$
a_{i00}	a_{100}	a_{100}	a_{100}	a_{100}	1
a_{i10}	a_{110}	0	$-a_{110}$	0	0
a_{i01}	0	a_{110}	0	$-a_{110}$	0
a_{i20}	a_{120}	a_{102}	a_{120}	a_{102}	a_{520}
a_{i11}	0	0	0	0	0
a_{i02}	a_{102}	a_{120}	a_{102}	a_{120}	a_{520}
a_{i30}	a_{130}	0	$-a_{130}$	0	0
a_{i21}	0	a_{221}	0	$-a_{221}$	0
a_{i12}	a_{112}	0	$-a_{112}$	0	0
a_{i03}	0	a_{130}	0	$-a_{130}$	0
a_{i40}	a_{140}	a_{104}	a_{140}	a_{104}	a_{540}
a_{i31}	0	0	0	0	0
a_{i22}	a_{122}	a_{222}	a_{122}	a_{222}	a_{522}
a_{i13}	0	0	0	0	0
a_{i04}	a_{104}	a_{140}	a_{104}	a_{140}	a_{540}

$$\mathbf{M}_{jk} = \mathbf{M}(\alpha_{c_j}, \beta_{c_k}) = \begin{bmatrix} 1 & \alpha_c & \alpha_c^2 & \beta_c^2 & 0 & \alpha_c^3 & \alpha_c\beta_c^2 \\ 1 & \beta_c & \beta_c^2 & \alpha_c^2 & 0 & \beta_c^3 & 0 \\ 1 & -\alpha_c & \alpha_c^2 & \beta_c^2 & 0 & -\alpha_c^3 & -\alpha_c\beta_c^2 \\ 1 & -\beta_c & \beta_c^2 & \alpha_c^2 & 0 & -\beta_c^3 & 0 \\ 0 & 0 & 0 & 0 & \alpha_c^2+\beta_c^2 & 0 & 0 \end{bmatrix}$$
$$\begin{bmatrix} 0 & \alpha_c^4 & \alpha_c^2\beta_c^2 & 0 & \beta_c^4 & 0 & 0 \\ \alpha_c^2\beta_c & \beta_c^4 & 0 & \alpha_c^2\beta_c^2 & \alpha_c^4 & 0 & 0 \\ 0 & \alpha_c^4 & \alpha_c^2\beta_c^2 & 0 & \beta_c^4 & 0 & 0 \\ -\alpha_c^2\beta_c & \beta_c^4 & 0 & \alpha_c^2\beta_c^2 & \alpha_c^4 & 0 & 0 \\ 0 & 0 & 0 & 0 & 0 & \alpha_c^4+\beta_c^4 & \alpha_c^2\beta_c^2 \end{bmatrix} \tag{B.23}$$

$$\mathrm{Cp}_{jk} \approx \widehat{\mathrm{C}}\mathrm{p}_{\mathrm{jk}} = \mathbf{u} + \mathbf{M}_{\mathbf{jk}}\mathbf{a} \tag{B.24}$$

Relationships between the Taylor series approximations to the pressure coefficients and the flow conditions (p_0, p, α_c, and β_c) existed. All five expansions were needed to develop these relationships and therefore all 14 calibration coefficients were required to be found. These calibration coefficients were again determined using a least squares procedure. The procedure required finding the values of the coefficients which minimized the error, represented by Equation B.25.

$$E = \sum_{i=1}^{5} \sum_{j} \sum_{k} \left[Cp_i(\alpha_{c_j}, \beta_{c_k}) - \widehat{C}p_i(\alpha_{c_j}, \beta_{c_k}) \right]^2 \tag{B.25}$$

The minimization was accomplished by taking the derivative of the error function (Equation B.25) with respect to each of the calibration coefficients and equating the results to zero (Equation B.26). The system of equations developed from this minimization process is presented in Equation B.27. Here the vector $\mathbf{Cp}_{jk}$ is given in Equation B.21. Equation B.27 was solved to obtain the calibration coefficients in vector $\mathbf{a}$.

$$\frac{\partial E}{\partial a_l} = -2 \sum_{i=1}^{5} \sum_{j} \sum_{k} \left[Cp_i(\alpha_{c_j}, \beta_{c_k}) - \widehat{C}p_i(\alpha_{c_j}, \beta_{c_k}) \right] \frac{\partial \widehat{C}p_i}{\partial a_l} = 0, \quad l = 1, \ldots, 14 \tag{B.26}$$

$$\sum_{j} \sum_{k} \mathbf{M}_{jk}^T (\mathbf{Cp}_{jk} - \mathbf{u}) = \left(\sum_{j} \sum_{k} \mathbf{M}_{jk}^T \mathbf{M}_{jk} \right) \mathbf{a} \tag{B.27}$$

Non-Yaw-Nulling Data Reduction

The data reduction procedure determined the local total pressure, static pressure and Mach vector components from the Taylor series approximations to the calibration pressure coefficients. The reduction process began by determining the pitch and yaw angles from a ratio of differences of measured pressures, represented by Equations B.28 and B.29. Here D is given in Equation B.30

$$f = \frac{2(p_1 - p_3)}{4p_5 - (p_1 + p_2 + p_3 + p_4)} = \frac{a_{110}\,\alpha_c + a_{130}\,\alpha_c^3 + a_{112}\,\alpha_c \beta_c^2}{D} \tag{B.28}$$

$$g = \frac{2(p_2 - p_4)}{4p_5 - (p_1 + p_2 + p_3 + p_4)} = \frac{a_{110}\beta_c + a_{130}\beta_c^3 + a_{221}\,\alpha_c^2 \beta_c}{D} \tag{B.29}$$

$$
\begin{aligned}
D = 1 - a_{100} &+ \left(a_{520} - \frac{1}{2}(a_{120} + a_{102})\right)(\alpha_c^2 + \beta_c^2) \\
&+ \left(a_{540} - \frac{1}{2}(a_{140} + a_{104})\right)(\alpha_c^4 + \beta_c^4) \\
&+ \left(a_{522} - \frac{1}{2}(a_{122} + a_{222})\right)(\alpha_c^2 \beta_c^2)
\end{aligned}
\tag{B.30}
$$

The right-hand-sides of Equations B.28 and B.29 are fourth-order approximations to the respective f and g functions. These equations are non-linear and coupled. An initial guess to the measure pitch and yaw angles was obtained by developing and solving second-order approximations to the f and g functions. The second-order approximations are given in Equations B.31 and B.32.

$$
f = \frac{2(p_1 - p_3)}{4p_5 - (p_1 + p_2 + p_3 + p_4)} = \frac{a_{110}\,\alpha_c}{1 - a_{100} + \left(a_{520} - \frac{1}{2}(a_{120} + a_{102})\right)(\alpha_c^2 + \beta_c^2)} \tag{B.31}
$$

$$
g = \frac{2(p_2 - p_4)}{4p_5 - (p_1 + p_2 + p_3 + p_4)} = \frac{a_{110}\beta_c}{1 - a_{100} + \left(a_{520} - \frac{1}{2}(a_{120} + a_{102})\right)(\alpha_c^2 + \beta_c^2)} \tag{B.32}
$$

The right-hand-sides of the second-order approximations to the respective f and g functions are also non-linear and coupled; however, the non-linear and coupling term $(\alpha_c^2 + \beta_c^2)$ in the denominators of Equations B.31 and B.32 can be found by solving the quadratic given in Equation B.33. Consequently, a first guess to measure pitch and yaw angles can be solved for explicitly from Equations B.31 and B.32.

$$
a(\alpha_c^2 + \beta_c^2)^2 + b(\alpha_c^2 + \beta_c^2) + c = 0 \tag{B.33}
$$

$$
\begin{aligned}
a &= (f^2 + g^2)\left(a_{520} - \frac{1}{2}[a_{120} + a_{102}]\right)^2 \\
b &= 2(f^2 + g^2)\left(a_{520} - \frac{1}{2}[a_{120} + a_{102}]\right)(1 + a_{100}) - a_{110}^2 \\
c &= (f^2 + g^2)(1 + a_{100})^2
\end{aligned}
$$

Non-linear terms in Equations B.28 and B.29 were linearized. The initial approximations to the measure pitch and yaw angles were used as a starting point for solving the fourth-order approximations represented by B.28 and B.29. The measure pitch and yaw angles were obtained iteratively and were determined upon convergence.

The local total and static pressures were found using Equation B.35 and the previously determined value of α_c and β_c. Here, the pressure coefficients, $\widehat{C}p$, are defined by Equation B.24. The total and static pressures were then used to determine the magnitude of the local Mach number, as given by Equation B.15.

$$\begin{bmatrix} \widehat{C}p_{1234} & 1-\widehat{C}p_{1234} \\ \widehat{C}p_5 & 1-\widehat{C}p_5 \end{bmatrix} \begin{bmatrix} p_o \\ p \end{bmatrix} = \begin{bmatrix} \frac{1}{4}(p_1+p_2+p_3+p_4) \\ p_5 \end{bmatrix} \tag{B.35}$$

$$\widehat{C}p_{1234} = \frac{1}{4}\left(\widehat{C}p_1 + \widehat{C}p_2 + \widehat{C}p_3 + \widehat{C}p_4\right)$$

The last step in the non-yaw-nulling data reduction procedure was to calculate the components of the Mach vector relative to the measurement plane. This step was completed in the same fashion as previously described in Yaw-Nulling Data Reduction and is therefore not presented here.

REPORT DOCUMENTATION PAGE

Form Approved
OMB No. 0704-0188

Public reporting burden for this collection of information is estimated to average 1 hour per response, including the time for reviewing instructions, searching existing data sources, gathering and maintaining the data needed, and completing and reviewing the collection of information. Send comments regarding this burden estimate or any other aspect of this collection of information, including suggestions for reducing this burden, to Washington Headquarters Services, Directorate for Information Operations and Reports, 1215 Jefferson Davis Highway, Suite 1204, Arlington, VA 22202-4302, and to the Office of Management and Budget, Paperwork Reduction Project (0704-0188), Washington, DC 20503.

1. AGENCY USE ONLY (*Leave blank*)	2. REPORT DATE	3. REPORT TYPE AND DATES COVERED
	December 1993	Technical Memorandum

4. TITLE AND SUBTITLE

A Study of the Compressible Flow Through a Diffusing S-Duct

5. FUNDING NUMBERS

WU–505–62–52

6. AUTHOR(S)

Steven R. Wellborn, Theodore H. Okiishi, and Bruce A. Reichert

7. PERFORMING ORGANIZATION NAME(S) AND ADDRESS(ES)

National Aeronautics and Space Administration
Lewis Research Center
Cleveland, Ohio 44135–3191

8. PERFORMING ORGANIZATION REPORT NUMBER

E–8247

9. SPONSORING/MONITORING AGENCY NAME(S) AND ADDRESS(ES)

National Aeronautics and Space Administration
Washington, D.C. 20546–0001

10. SPONSORING/MONITORING AGENCY REPORT NUMBER

NASA TM–106411

11. SUPPLEMENTARY NOTES

Steven R. Wellborn and Theodore H. Okiishi, Iowa State University, Ames, Iowa 50011; and Bruce A. Reichert, NASA Lewis Research Center. Responsible person, Bruce A. Reichert, (216) 433–2743.

12a. DISTRIBUTION/AVAILABILITY STATEMENT

Unclassified - Unlimited
Subject Category 02

12b. DISTRIBUTION CODE

13. ABSTRACT ***(Maximum 200 words)***

Benchmark aerodynamic data are presented for compressible flow through a representative S-duct configuration. A numerical prediction of the S-duct flow field, obtained from a subsonic parabolized Navier-Stokes algorithm, is also shown. The experimental and numerical results are compared. Measurements of the three-dimensional velocity field, total pressures and static pressures were obtained at five cross-sectional planes. Aerodynamic data were gathered with calibrated pneumatic probes. Surface static pressure and surface flow visualization data were also acquired. All reported tests were conducted with an inlet centerline Mach number of 0.6. The Reynolds number, based on the inlet centerline velocity and duct inlet diameter, was 2.6×10^6. Thin inlet turbulent boundary layers existed. The collected data should be beneficial to aircraft inlet designers and the measurements are suitable for the validation of computational codes. The results show that a region of streamwise flow separation occurred within the duct. Details about the separated flow region, including mechanisms which drive this complicated flow phenomenon, are discussed. Results also indicate that the duct curvature induces strong pressure driven secondary flows. The cross flows evolve into counter-rotating vortices. These vortices convect low momentum fluid of the boundary layer toward the center of the duct, degrading both the uniformity and magnitude of the total pressure profile.

14. SUBJECT TERMS

Computational; Fluid dynamics; Engine inlets; Inlet flow; Intake systems; Separated flow

15. NUMBER OF PAGES

99

16. PRICE CODE

A05

17. SECURITY CLASSIFICATION OF REPORT	18. SECURITY CLASSIFICATION OF THIS PAGE	19. SECURITY CLASSIFICATION OF ABSTRACT	20. LIMITATION OF ABSTRACT
Unclassified	Unclassified	Unclassified	

National Aeronautics and
Space Administration

Lewis Research Center
Cleveland, OH 44135-3191

Official Business
Penalty for Private Use $300